UNIVERSITY OF SOUTHAMPTON

FACULTY OF PHYSICAL AND APPLIED SCIENCES

Optoelectronics Research Centre

Reconfigurable Photonic Metamaterials

Jun-Yu Ou

Thesis for the degree of Doctor of Philosophy

September 2014

UNIVERSITY OF SOUTHAMPTON

ABSTRACT

FACULTY OF PHYSICAL AND APPLIED SCIENCE

Optoelectronics Research Centre

Doctor of Philosophy

RECONFIGURABLE PHOTONIC METAMATERIALS

by Jun-Yu Ou

This thesis reports on the development of a new class of switchable nanostructured photonic metamaterials, Reconfigurable Photonic Metamaterials (RPMs). Over the last decade, fascinating material properties including negative refraction, optical magnetism, invisibility, asymmetric transmission, perfect lenses and many more were demonstrated in metamaterials. Inspired by pioneering work on micro-electro-mechanical metamaterials for the terahertz and microwave spectral regions with feature sizes from millimeters to tens and hundreds microns, I develop reconfigurable photonic metamaterials for the optical spectral range that have sub-micron meta-molecules and nanoscale design features.

In particular, for the first time I developed:

- Novel fabrication processes for manufacturing reconfigurable photonic metamaterials based on the platform of elastic silicon nitride membranes using focused ion beam lithography, film deposition, precise alignment, etching and annealing techniques. These fabrication techniques have allowed the manufacturing of a wide range of reconfigurable metamaterials consisting of bi-layer (gold/silicon nitride) or tri-layer (gold/silicon nitride/gold) structured membranes suitable for applications as plasmonic RPMs.

- Novel RPMs tunable by ambient temperature that operate in the optical and near infrared parts of the spectrum. With such metamaterials exploiting the change in plasmonic response due to differential thermal expansion in bimorph nanostructures I have demonstrated 50% changes in optical transmission at the wavelength of 1735 nm when the temperature is ramped from 76 K to 270 K.

- Novel RPMs operating in the near-infrared part of the spectrum that can be controlled by electric signals. These types of metamaterials harness electrostatic forces on the nanoscale and offer up to 20 MHz modulation bandwidth. At a threshold level of stimulation these metamaterials exhibit non-volatile switching with up to 250% transmission change. As a part of this research I developed a characterization technique that allows imaging and recording of the electrostatic switching under a scanning electron microscope.

- Novel optically controlled RPMs exploiting near-field optical forces induced by light and optical heating for reconfiguration. Such metamaterials show a new type of optomechanical nonlinearity leading to intensity-dependent transmission that exceeds the cubic nonlinearity of GaAs by seven orders of magnitude. Using CW diode lasers operating at telecommunication wavelengths of 1.3 μm and 1.55 μm I have demonstrated cross-wavelength optical modulation with amplitude of about 1 % that can be achieved at only about 1 mW of average power of the control beam. I also developed the numerical analysis of thermo-opto-mechanical properties of the structures and calculated eigenmodes and cooling constants of the RPMs under modulated laser irradiation.

Overall, the development of reconfigurable photonic metamaterials provides a new and flexible platform for the control of metamaterial properties “on demand”. Such metamaterials can find applications in sensors, tunable spectral filters, switches, modulators, programmable transformation optics devices and any other application where tunable optical properties are required.

Contents

List of Figures

List of Tables

DECLARATION OF AUTHORSHIP

I, Jun-Yu Ou, declare that the thesis entitled "Reconfigurable photonic metamaterials" and the work presented in the thesis are both my own, and have been generated by me as the result of my own original research. I confirm that:

- this work was done wholly or mainly while in candidature for a research degree at this University;
- where any part of this thesis has previously been submitted for a degree or any other qualification at this University or any other institution, this has been clearly stated;
- where I have consulted the published work of others, this is always clearly attributed;
- where I have quoted from the work of others, the source is always given. With the exception of such quotations, this thesis is entirely my own work;
- I have acknowledged all main sources of help;
- where the thesis is based on work done by myself jointly with others, I have made clear exactly what was done by others and what I have contributed myself;
- parts of this work have been published as the journal papers and conference contributions listed in Appendix A Publications.

Signed: _____

Date: _____

Acknowledgements

The work presented in this report would be impossible without the help of my sponsor, supervisors, collaborators and my wife. Here I would like to thank those people who have helped me to get to this stage, in particular:

- Nikolay Zheludev and Eric Plum, my supervisors, for their guidance of my research.
- My collaborators, without whom some of my work would not have been possible. Especially Nikitas Papasimakis for helping me build and optimize my first COMSOL models. I have also enjoyed and benefited a lot from my collaboration with Jianfa Zhang on simulation of reconfigurable photonic metamaterials.
- My group members and ORC/ECS cleanroom technicians. Especially, Takashi Uchino for his kind help and useful advice on sample fabrication, Giorgio Adamo for helping me get first observation of temperature controlled RPMs and Neil Sessions for training me to use the ORC cleanroom facilities.
- I appreciate my wife Sharon's encouragement and full support of my PhD studies. Without her, I would not have reached this stage.

1 Introduction

1.1 Motivation

Metamaterials are composed of sub-wavelength unit cells, so-called meta-molecules, which control their electromagnetic properties [1,2]. Engineering of the meta-molecule's geometry allows the realization of metamaterials with unique properties including negative refractive index [3, 4], artificial magnetism [5] and novel devices like invisibility cloaks [2], the lasing spaser [6] and superlenses [1] making them promising building blocks for future optical components. Nevertheless, few of these demonstrations have lead to practical applications, largely because the unique properties of metamaterials are usually fixed and limited to a single wavelength [7].

Switchable and tunable metamaterials are expanding areas of research driven by the development of nanophotonic all-optical data processing circuits, optical memory, smart surfaces, adaptable detection and imaging systems and transformation optics devices [8]. Several avenues are being explored. Metamaterials where metal nanostructures are hybridized with nonlinear and switchable layers provide a way to achieve high-contrast optical switching and enhanced nonlinear responses. Indeed, a change in the refractive index or absorption in the hybridized material will modify the plasmon spectrum of the nanostructure. This can lead to a large change in the resonant transmission and reflection characteristics of the hybrid structure. Also, the ability to change a metamaterial's response at terahertz frequencies by injection or optical generation of free carriers in a semiconductor substrate has been reported [9, 10]. A layer of single-wall semiconductor carbon nanotubes deposited on a metamaterial shows an order of magnitude higher nonlinearity than the already extremely strong response of the nanotubes themselves, due to resonant plasmon-exciton interactions [11]. Nanoscale metamaterial electro-optical

switches using phase change chalcogenide glass [12] and vanadium dioxide [13] have already been demonstrated. Graphene is another favorite that promises to add electro-optical capability to metamaterials, in particular in the infrared and terahertz domains, by exploiting the spectral shift of the electromagnetic response that is driven by applied voltage [14, 15].

When high speed switching is not the prime objective, metamaterials can be reliably and reversibly controlled by microelectromechanical (MEMS) actuators repositioning parts of the meta-molecules. MEMS-based metamaterials can provide continuous tuning, rather than step-like switching associated with phase-change materials, and in contrast to approaches exploiting optical nonlinearities they are compatible with low intensities. This has been convincingly demonstrated for terahertz metamaterials consisting of specially-designed deformable meta-molecules [16–19]. Reconfigurable photonic metamaterials (RPMs) operating in the visible and near-infrared parts of the spectrum require the development of components and actuators operating on the scale of a few tens of nanometers.

It is well-known that the overall properties of a material are not only determined by the nature of the constituent atoms and molecules but also depend dramatically on the lattice structure. The same rule applies to metamaterials. Compared with natural materials, achievable properties through adjusting the crystal lattice are limited by chemical bonding and the nature of the atoms themselves, the range of tunability for metamaterials is much broader as the lattice effects can be made much stronger by an appropriate design. Therefore, structural tunability is a new and promising route to real-time control of the electromagnetic (EM) properties of metamaterials such as polarization characteristics, transmission and reflection amplitudes and phases, asymmetric transmission and optical activity. For the infrared and visible spectral regions which correspond to micron and sub-micron wavelengths, the geometric dimensions of the required sub-wavelength resonators are on the order of hundreds of nanometers or even smaller. At this size scale, the emerging nanoelectromechanical systems (NEMS) technologies provide an opportunity to control metamaterial structures and their optical properties.

My PhD project focuses on systematically developing novel reconfigurable NEMS photonic metamaterials. By combining NEMS technology with metamaterials, active and dynamic control of metamaterials are achieved in response to external stimuli such as temperature, electrical voltage and light. These efforts provide us with a novel platform

for tunable metamaterials for the optical part of the spectrum.

1.2 Background

At the beginning of this chapter, the different methods of realizing metameterials with tunable characteristics will be briefly introduced. Thereafter, reconfigurable metamaterials and NEMS will be discussed in greater detail.

1.2.1 Metamaterials

The research field of metamaterials has grown rapidly over the last 15 years since the discovery of artificial structures with negative magnetic responses [20] and negative refractive index [1, 3, 21]. It now includes a broad range of materials that attain unusual electromagnetic properties from structuring on at a scale smaller than the wavelength of incident radiation. Examples include novel physical phenomena such as asymmetric transmission [22], transformation optics [23] and invisibility cloaking [24], as well as dramatic enhancements of e.g. optical activity [25, 26] and optical nonlinearities [27, 28]. The field of metamaterials partially overlaps with the area of photonic crystals [29–31]. The development of the latter was initially driven by the goal to create structures with photonic band gaps analogous to the electronic band gaps of semiconductors. Photonic band gaps are frequency ranges where photons cannot propagate and as a result light is confined near defects of the structure, which can be designed to have frequency and polarization characteristics [32]. While metamaterial structures are ideally much smaller than the wavelength to ensure an effective medium response, photonic crystals tend to be close to the diffraction regime.

1.2.2 Tunable Metamaterials

Current efforts in metamaterials research focus on dynamic functionalities such as tunability, switching and modulation of electromagnetic waves [33]. To this end, various approaches have appeared, including embedded varactors [34], phase-change media [12, 13], use of liquid crystals [35, 36], electrical modulation with graphene [37, 38] and superconductors [39], and carrier injection or depletion in semiconductor substrates [10, 40]. However, tuning, switching and modulating metamaterial properties in the visible and near-infrared range remain major technological challenges: the existing microelectromechanical solutions and designs for the sub-THz [41] and THz [17–19] regions are extremely

challenging to shrink by 2-3 orders of magnitude in dimension (size of unit cell from few tens of microns to hundreds of nanometers) in order to enter the optical spectral range.

In general, tunable metamaterials can be divided into two major categories. One is based on changing the effective electromagnetic properties via various nonlinear effects in the resonators [42, 43] or materials hybridized with metamaterials [11, 12, 37]. The other is based on structural reconfiguration [44], such as changing the lattice [44–46], or reorienting [16] or reshaping the structural elements [17, 18]. The geometry changes of the metamaterial micro/nano-structures are often induced by mechanical shifting or deformation of the metamaterials.

1.2.2.1 Tunable Hybrid Metamaterials

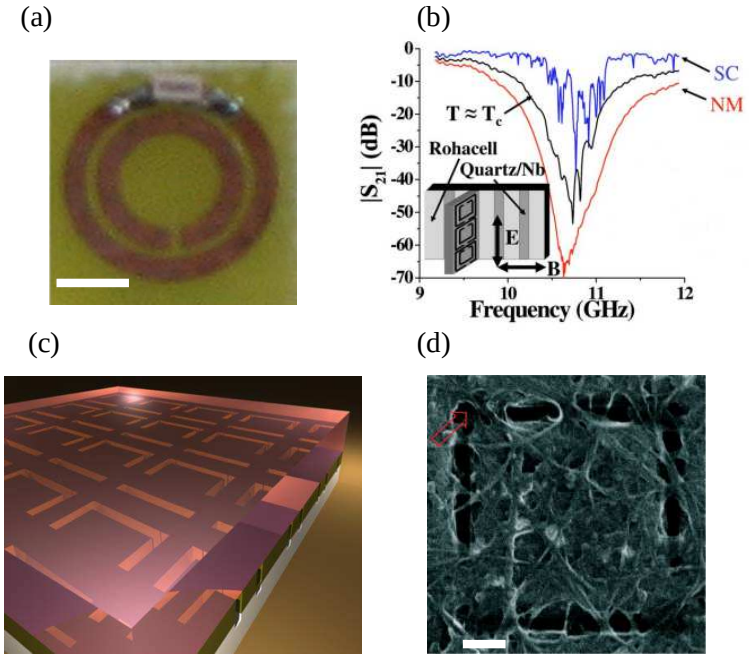

Figure 1.1: **Examples of tunable metamaterials.** (a) Split ring resonator with various capacitors loaded in the outer split region, scale bar is 1mm [42]. (b) Superconducting metamaterial [43]. (c) Phase change metamaterial [12]. (d) Nonlinear metamaterial, scale bar is 100nm [11].

Many early designs of tunable/switchable metamaterials focused on changing directly the distributed capacitance or distributed inductance of the resonators by adding a tunable capacitor or inductance [42]. This method, though simple and effective for millimeter-scale microwave resonators, cannot be applied to the micron/sub-micron scale structures required for optical metamaterials.

Tunable/switchable metamaterials have also been realized based on superconductors by exploiting the breakdown of superconductivity at the critical temperature, in strong magnetic fields, and for large electrical currents [43, 47, 48]. However, superconducting metamaterials cooled to cryogenic temperatures can control electromagnetic waves only up to terahertz frequencies. As higher frequency photons have enough energy to break the superconducting Cooper pairs, they are unsuitable for controlling metamaterials in the infrared and visible spectral ranges.

Another interesting approach is to include materials with tunable properties in the metamaterial. The dielectric function of metals is generally robust, difficult to tune by an external stimulus. Fortunately, the electromagnetic properties of metamaterials are very sensitive to the surrounding environment, which provides another dimension for tunable/switchable metamaterials. The use of materials with tunable electrical or optical properties allows control over the resonant response of metamaterials. The hybrid metamaterial approach has been proven effective in various tunable metamaterials that respond to the application of external electric current [12], light [49], heat [50] and so on.

In particular, nanoscale metamaterial electro-optical switches using phase change chalcogenide glass [12] and vanadium dioxide [13] have been demonstrated. Phase change metamaterials work in the visible and near infrared, however, they are typically limited to switching rather than continuous tuning. Nonlinear material also can be used to achieve tunable photonic metamaterials, where high intensities are acceptable. A layer of single-wall semiconductor carbon nanotubes deposited on a metamaterial shows an order of magnitude higher nonlinearity than the already extremely strong response of the nanotubes themselves, due to resonant plasmon-exciton interactions [11]. In addition, a 600 fs device response by utilizing a regime of subpicosecond carrier dynamics in α-Si and 20% modulation in a path length of only 116 nm by exploiting the enhanced nonlinearities in metamaterials has been demonstrated [49].

1.2.2.2 Reconfigurable Metamaterials

Structural reconfiguration is a straightforward approach for efficient control of optical characteristics of metamaterial. For sufficiently dense metamaterials, the meta-molecules are strongly coupled and therefore their optical properties can be changed dramatically by lattice tuning [51] [52].

The most simple lattice tuning approach is to vary a lattice constant, e.g. lattice

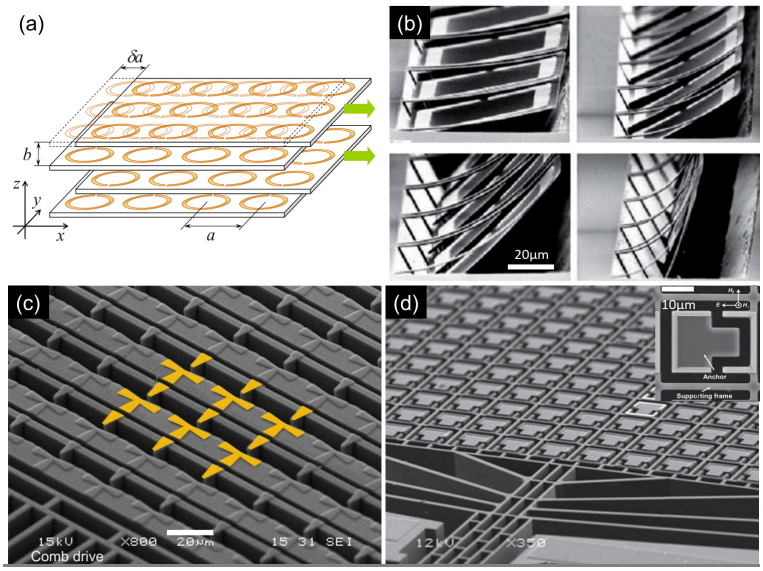

Figure 1.2: **Examples of GHz and THz reconfigurable metamaterials.** (a) Illustration of the staggered lattice shift with a lateral displacement of every second metamaterial layer [44]. (b) Scanning electron microscopy (SEM) images of arrays of metamolecules of a terahertz metamaterial are switched from one configuration to the other by thermal activation [16]. (c,d) Terahertz metamaterial can be dynamically tuned by manufacturing the metamaterial array on a MEMS-driven silicon platform. Inset: SEM showing the metamolecule consisting of static and movable components [17, 19].

parameter b in the anisotropic split ring metamaterial shown in Fig. 1.2(a). It was shown that the resonance frequency can be impressively shifted in this way [51]. Consequently, the metamaterial characteristics can be tuned. A disadvantage of this method is that varying b significantly would imply a corresponding change in the overall dimension of the metamaterial along z, which might be undesirable for certain applications. Another direction of structural tuning is by changing a periodic lateral displacement of layers in the $x-y$ plane [44]. In this way, the resonators become displaced along x (or y, or both) by a fraction of the lattice constant a with respect to the original position. As a result, a resonance of the medium can be "moved" across a signal frequency, leading to a drastic change in transmission characteristics. It is clear that for practical applications it is not even necessary to exploit the whole range of lateral shifts – in the above example it is sufficient to operate between $0.1a$ and $0.3a$ where most of the transition occurs.

Based on the idea described above, reconfigurable metamaterial structures have been pioneered in the GHz [44] and THz [16] spectral ranges. In the early work illustrated by Fig. 1.2(b) rapid thermal annealing has been used to lock split ring resonators in fixed tilted positions [16]. In order to achieve dynamic control of reconfigurable metamate-

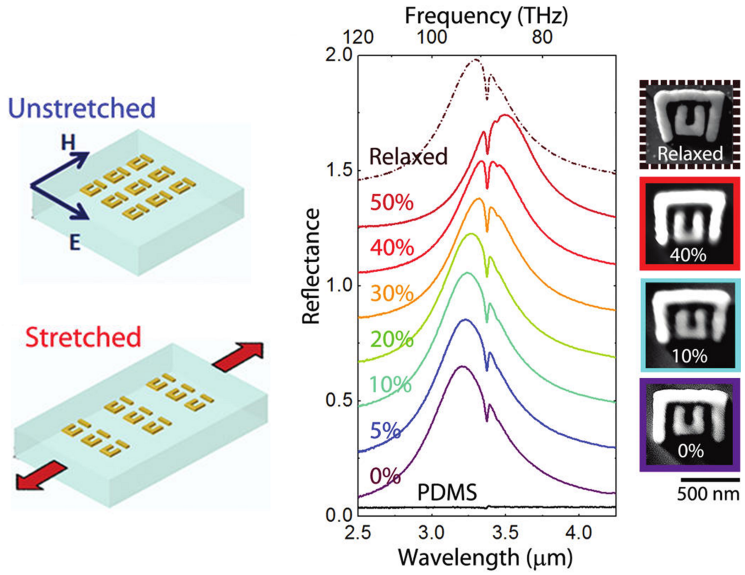

Figure 1.3: **Mid-infrared Metamaterials on a Flexible Subtract.** A compliant metamaterial with tunability of $\Delta\lambda\sim400$ nm at mid-infrared wavelength, using high-strain mechanical deformation of an elastomeric substrate to control the distance between the resonant elements [53].

rials, a quite complex electromechanically controlled reconfigurable THz metamaterials have been demonstrated driven by typical MEMS comb drive actuators [54], shown in Fig. 1.2(c) and (d) [17–19]. The mechanical tuning of the metamaterials requires a controllable actuation of the sub-wavelength structures and often results in a slow response time. For example, a typical micromachined structure has a size of 1–100 mm and the actuation time is more than 100 μs, which means that the modulation frequency of micromachined tunable metamaterials for the THz region is less than 10 kHz [55].

However, moving to optical frequencies requires about 100 times smaller structures and nanoscale movements. This requires simpler structures and new ideas. One approach is using strain induced deformation of metamaterials on a flexible substrate, shown in Fig. 1.3 [53,56]. The mechanical deformation of elastomeric substrates has been used to induce spectral shifts in the resonance of nanophotonic structures such as nanoparticle dimer extinction [57] and metamaterials [53,56]. Nevertheless, physical deformation of a mm size flexible substrate takes hundreds of microseconds which is not suitable for fast dynamic turning of photonic metamaterials.

In order to realize dynamic and active control with nanoscale displacement within a meta-molecule, nanoelectromechanical systems (NEMS) and basic actuation mechanisms for nanoscale structures will be discussed in the following section.

1.2.3 Nanoelectromechanical Systems

The last decade has been an exciting period for people working in the fields of NEMS and nanofabrication technologies. Starting from the earliest devices in electromechanical transducers, such as accelerometers [58, 59], sensors [60], actuators [61], and optical switches [62] which are among the most commercially successful NEMS devices and systems [63–65], the technology has experienced a rapid expansion into many different fields of engineering, physical sciences, and bio medicine.

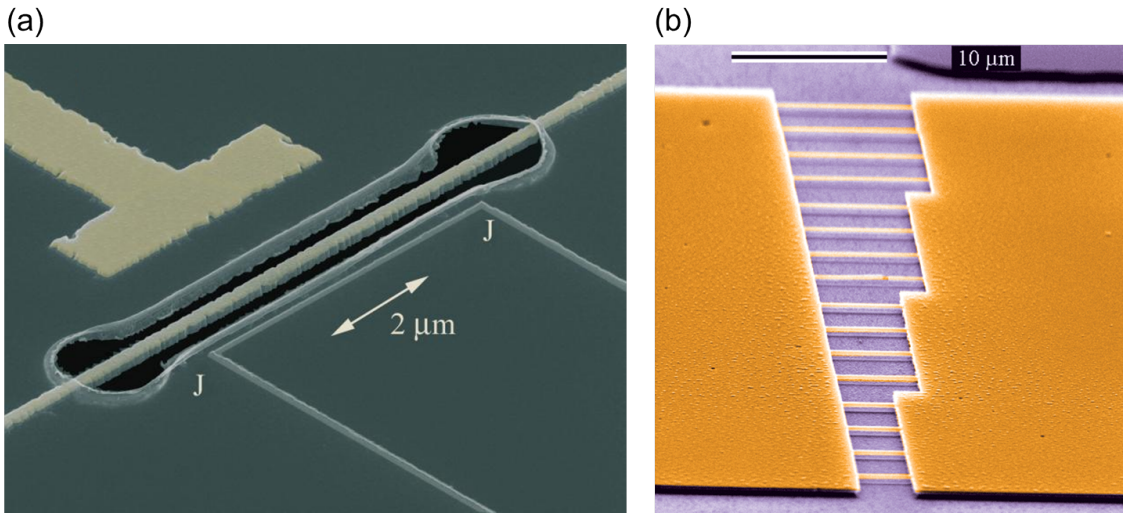

Figure 1.4: **Examples of NEMS devices.** (a) SEM micrograph of a nanoelectromechanical system composed of a microscopic mechanical resonator capacitively coupled to a superconducting single-electron transistor which was used to study the quantum limit of nanomechanical resonator. A 19.7 MHz nanomechanical resonator (200 nm wide, 8 μm long, coated with 20 nm of Au on top of 100 nm Si_3N_4), defined by the regions in black where the Si_3N_4 has been etched through. A superconducting single electron transistor island (5 μm long and 50 nm wide) is positioned 600 nm away from the resonator. Tunnel junctions, marked "J" are located at corners [66]. (b) SEM micrograph of doubly clamped NEMS beams [67]. These NEMS beams were used to demonstrate optical interferometric displacement detection techniques.

Nanoengineering studies nanoscale structures, devices and systems that exhibit novel physical (electromagnetic, electromechanical, optical, etc.), chemical, electrochemical and biological properties, phenomena, and effects. NEMS and their components (nanostructures) are structured on a scale from 10^{-10}m (molecule size) to 10^{-7}m; that is, from 0.1 to 100 nanometers. To manufacture nanostructures, nanotechnology is applied. In contrast, the dimension of MEMS and their components (devices and microstructures) is from 100 nanometers to the millimeter range. Conventional microelectronics technolo-

gies are usually used to fabricate MEMS. Studying nanoscale systems, one concentrates on the atomic and molecular levels in manufacturing, fabrication, design, analysis, optimization, integration, synthesis, etc. Reducing the dimension of systems leads to the application of novel materials (carbon nanotubes, molecular wires, etc.) and new fabrication technologies, such as electron beam lithography and focused ion beam lithography. The problems to be solved range from high-yield mass production, assembling, and self-organization to devising novel high-performance MEMS and NEMS [68], see Fig. 1.4. For example, micro and nanoscale switches, logic gates, actuators, and sensors are being devised, studied, optimized, and fabricated.

Today, nanomechanical systems are widely used in applications from thermal sensing and infrared imaging to chemical and biological sensing. This huge success is due to the fact that sensors based on micro/nano cantilevers can detect extremely small stimuli such as temperature and mass changes as well as small external forces. Available devices can be placed in two categories based on their readout scheme. NEMS use a wide array of electronic coupling schemes to transduce mechanical energy into electronic signals, while micro-optomechanical systems are usually read out using an optical interferometer.

1.3 Conclusion and Thesis Overview

In summary, the research on reconfigurable metamaterials so far focus on the millimeter to mid-infrared wavelength range and the operation speed of reconfigurable metamaterials has been limited to 10s of kHz. The main objective of my PhD research is to develop reconfigurable photonic metamaterials for the optical spectral range that have deep sub-micron meta-molecules and MHz operational speed.

Reconfigurable photonic metamaterials are a flexible and convenient platform for realizing tunable and switchable metamaterials in the optical part of the spectrum. This thesis reports on the first demonstrations of reconfigurable metamaterials operating in the optical spectral range. Reconfigurable photonic metamaterials controlled by ambient temperature, electrical voltage and light are demonstrated, creating novel opportunities for sensing, electro-optical devices and optical data processing. Also, during the period of this project, sophisticated nanofabrication techniques based on focused ion beam milling and electron beam lithography for optical metamaterials/metadevices have been developed.

Chapter 2 provides a review of nanofabrication techniques for photonic metamaterials leading to the main fabrication technique used in this thesis which is focused ion beam (FIB) lithography. The interactions between ions and matter are discussed in order to explain the working principles of FIB. A detailed description of focused ion beam milling, and fabrication examples from my PhD period are presented.

Chapter 3 focuses on the first experimental demonstration of reconfigurable photonic metamaterial working in the optical spectral range. This reconfigurable photonic metamaterial is reconfigured by changes of the ambient temperature. It is experimentally shown how coupled resonators that reconfigure in response to temperature changes exhibit large changes of their optical properties at optical wavelengths.

Chapter 4 reports the demonstration of the first reconfigurable photonic metamaterial that is driven by electrostatic forces. This novel class of reconfigurable nanostructures introduced here transfers electrically reconfigurable metamaterials from the terahertz to the optical part of the spectrum, while simultaneously increasing their modulation speed up to MHz frequencies.

Chapter 5 demonstrates for the first time experimentally that photonic metamaterials can be reconfigured and modulated by light. Evidence of two mechanisms of optomechanical deformation, (i) optical heating leading to deformation of bimaterial structures and (ii) optical forces between plasmonic resonators, is observed.

Finally, the work covered in this thesis is summarized in Chapter 6, together with an outlook of the potential routes of further investigation for each of the three experimental breakthroughs reported here.

2

Nanofabrication Technology for Photonic Metamaterials

2.1 Introduction

The main mission of metamaterials research is not only design or theoretical prediction of fascinating properties, but also realization of such structures. The recent revolutionary progress in optical metamaterial research became only possible because of improvements in nanofabrication technology developed over the last two decades. Manufacturing optical metamaterials is extremely challenging because the definition of metamaterials involves that the size of meta-molecules must be substantially smaller than their operating wavelength, which is few hundreds of nanometers for visible light, see an example in Fig. 2.1. As a consequence, the fabrication of optical metamaterials requires the creation of features at deep subwavelength scale. Due to the fact that the required feature sizes for optical metamaterials fabrication are smaller than the resolution of state-of-the-art photolithography, 2D metamaterial layers are normally fabricated using complicated technologies such as electron beam lithography (EBL), focused ion beam (FIB) lithography/milling, nanoimprint lithography, interference optical lithography, direct laser writing, and many more [69, 70].

In the semiconductor industry, optical lithography is the main patterning method that allows for cost efficient, high-volume fabrication of micro- and nanoelectronic devices. Nevertheless, alternative lithography methods coexist and stand out in all cases where the requirement for a photomask is a disadvantage. Especially for low-volume fabrication of nanodevices like optical metamaterials and for prototype device development, the need for a photomask is inefficient and restrictive. The fabrication of high-resolution masks with a price well above £10k is too cost intensive for the fabrication of single test devices. Nanofabrication of silicon-based devices commonly relies on a combination of

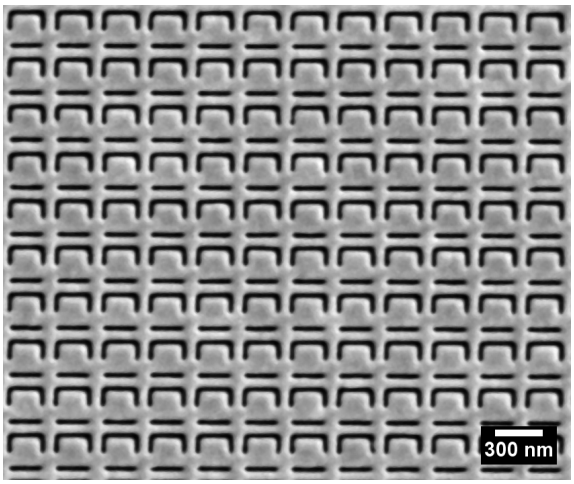

Figure 2.1: **SEM micrograph of an optical asymmetric split ring aperture metamaterial.** It consists of 50nm thick gold on fused quartz fabricated by focused ion beam (FIB) lithography.

optical lithography followed by plasma etching of the silicon or of dielectric films (SiO_2, Si_3N_4). The flexibility of silicon processing is augmented by the availability of chemical vapor deposition (CVD) of polycrystalline silicon, which provides excellent conformality and step coverage. Unfortunately, most CVD-deposited metal films, especially those useful for plasmonics, have degraded optical properties due to inherent contaminants from the precursor materials. Unlike silicon, most metals are not suitable for dry etching. In particular, gold and silver cannot be easily plasma etched because their etch by-product is nonvolatile. Physical patterning such as ion milling is thus often required but may worsen surface roughness and contaminate the metallic surface with implanted ions [71].

For these reasons, 'direct-write' approaches have emerged that are popular for several applications such as mask fabrication, 3D patterning and rapid prototyping [72]. Optical direct-write lithography and electron beam lithography are among the most spectacular techniques of direct-write lithography. Less known, but extremely versatile and powerful, is the ion beam lithography method.

Optical direct laser write lithography uses laser beam writers with a programmable spatial light modulator (SLM). With 500 mm^2/minute write speed and advanced 3D lithography capabilities, optical direct-write lithography is also suitable for commercial microchip fabrication [72]. With a resolution of 0.6-μm minimum feature size of the photoresist pattern, regular optical direct-write lithography cannot be considered a nanopatterning method for optical metamaterials. However, in two-photon direct laser writing, femtosecond laser pulses are tightly focused into the volume of a photoresist.

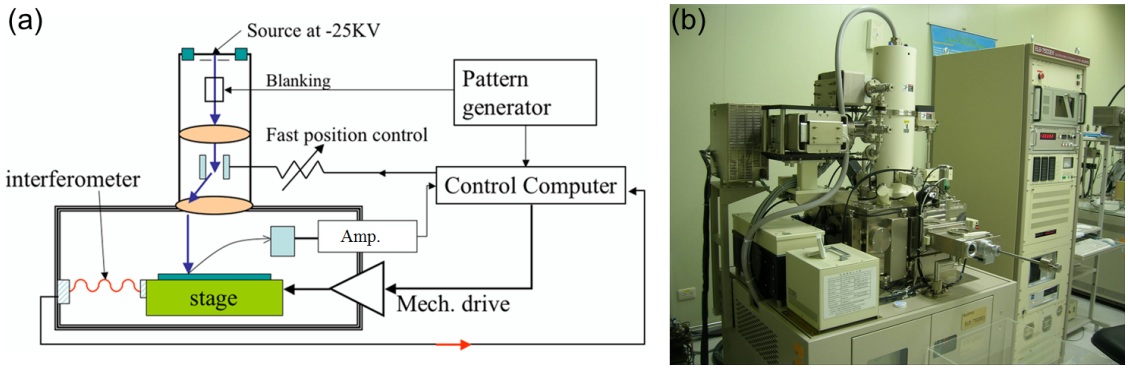

Figure 2.2: **Block diagram and commercial electron beam lithography system.** (a) Block diagram showing the major components of a typical electron beam lithography system [77]. (b) A commercial electron beam lithography system (ELIONIX Ltd. model: ELS-7500EX [78]).

Two-photon absorption ensures that only a tiny volume of the photoresist is sufficiently exposed by the light. Computer-controlled scanning of the focus and resist using piezoelectric actuators allows almost arbitrary polymer structures to be fabricated [30, 73, 74] with lateral features as small as 100 nm. This value is an order of magnitude larger than state-of-the-art electron-beam lithography. However, recent work using stimulated emission depletion direct laser writing [75] has approached lateral resolutions of 50 nm, with potential for future improvements. The progress of two-photon direct laser writing in the last decade makes fabrication of 3D photonic metamaterials possible [70].

Electron beam lithography, on the other hand, uses a focused electron beam to expose an electron beam resist. A resolution of 10 nm minimum feature size of the e-beam resist pattern has been successfully demonstrated with this method, see a commercial EBL system and block diagram [76] in Fig. 2.2. However, special resists are required for e-beam lithography, that are compatible with the high energy of forward scattered, back-scattered and secondary electrons. A common resist for sub-50nm resolution is polymethylmetacrylate (PMMA) requiring an exposure dose above 200 $\mu C/cm^2$. For highest resolution (below 20 nm) inorganic resists such as hydrogen silsesquioxane (HSQ) are also used. The exposure of a sensitive resist with an electron beam is the core of the EBL process. The resist is often a polymer dissolved in a liquid solvent, which is coated onto a surface and baked to form a thin layer. During electron beam exposure, the solubility of the resist is altered, causing a dissolution variation compared to areas that are not exposed. Following this, the pattern is developed using a liquid developer. After patterning a resist layer with e-beam lithography, the pattern must then be transferred

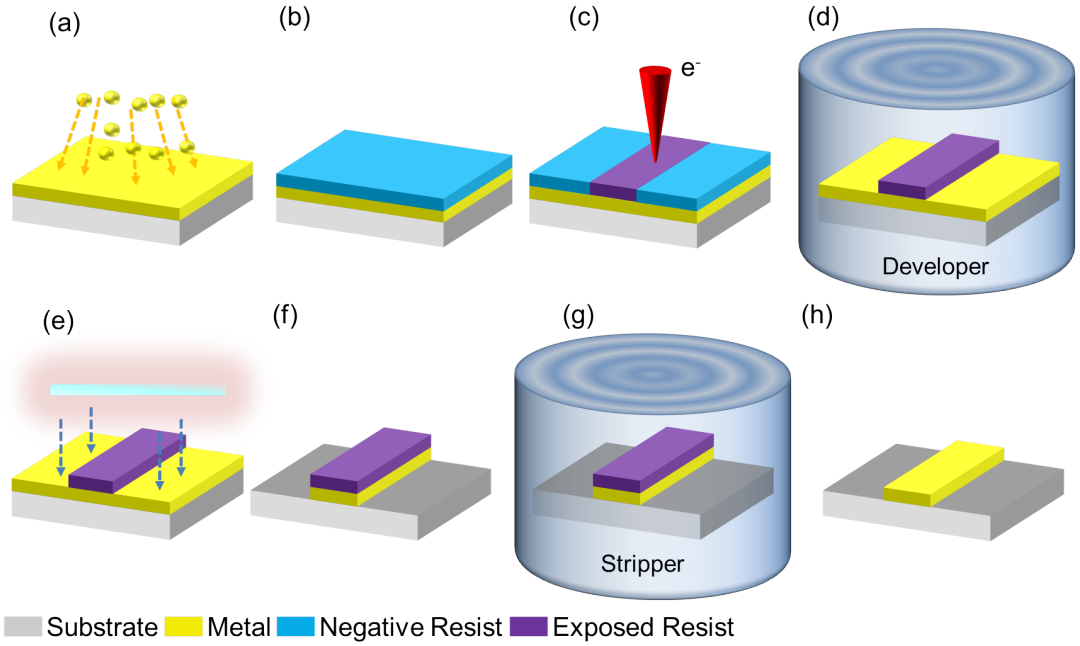

Figure 2.3: **Standard electron beam lithography in combination with dry etching process.** (a) Metal deposition. (b) Negative tone e-beam resist spin coating,. (c) E-beam exposure. (d) Resist development, removing unexposed resist. (e) Dry etching by ion milling (Ar^+ ion) or reactive ion etching. (f) Metal pattern covered by exposed resist. (g) Exposed resist stripping by stripper solvent(wet process) or oxygen plasma (dry process). (h) Desired metal structure.

to the substrate via wet etching, dry etching, ion milling, lift-off, or electrodeposition. Fig. 2.3 shows the series of nanostructuring steps during the EBL procedure. Due to being relatively slow and expensive, this high-resolution method is only used for writing photomasks for optical projection lithography and for a limited number of high-end applications. A solution to this dilemma may be the use of multi-beam electron tools [79] and electron projection lithography [80], which are under development.

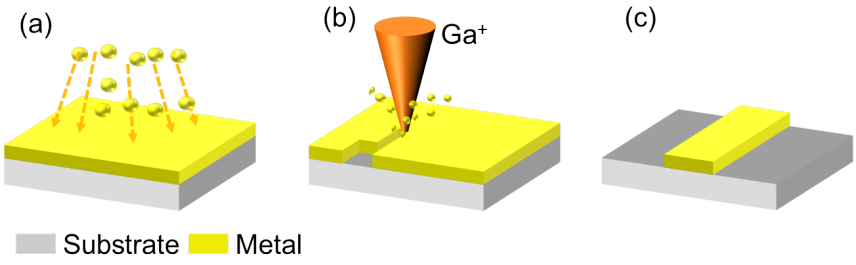

Figure 2.4: **Standard focused ion beam lithography process.** (a) Metal deposition. (b) Unwanted material removed by focused ion beam. (c) Desired metal structure.

Focused ion beam lithography is similar to EBL, but it uses Ga^+ ions or other types of ions instead of electrons. The capabilities of FIB are superior to EBL especially in low-volume nanofabrication. There is a simple comparison between the processes of EBL, shown in Fig. 2.3, and FIB lithography, shown in Fig. 2.4. When FIB is used to remove surface material by local physical sputtering of ions in order to create the desired metal pattern on a substrate, the process flow can be simplified as only two steps: (a) metal deposition and (b) FIB milling. No solvent-based chemical process is involved in FIB lithography, therefore surface adhesion of metals and surface tension issues resulting from solvent processes are not an issue. Not only can FIB lithography (i) locally mill away atoms by physical sputtering with sub-10nm resolution (subtractive lithography), but it is also capable of (ii) creating a pattern in a resist layer just like EBL, (iii) locally depositing material with sub-10nm resolution (additive lithography), (iv) local ion implantation for fabrication of an etching mask for subsequent pattern transfer and (v) direct material modification by ion-induced effects. FIB lithography will be discussed more in next the section.

2.2 Focus Ion Beam Lithography

Historically, FIB technology was mainly used for sample preparation for transmission electron microscopy (TEM), failure analysis for semiconductors and MEMS, photolithography mask repairing, and circuit edit procedures [81]. Recently, FIB lithography has been emerging as a resistless direct patterning technique. Continuously developed over the last 10 years, FIB lithography has a fast growing user community and a significant and growing number of publications cite FIB as the primary nanofabrication technique [69, 71, 82].

2.2.1 Working Principles of Focused Ion Beam

The physical picture of the solid-ion interaction explains the processes and conditions relevant to the use of FIB systems in materials science. When an ion hits on a solid, it loses kinetic energy through interactions with the sample atoms. This transfer of energy from the ion to the solid results in a number of different processes (see Fig. 2.5): ion reflection and back-scattering, electron emission, electromagnetic radiation, atomic sputtering and ion emission, sample damage, and sample heating [81]. The ion typically comes to rest in the solid, leading to implantation of the ion. With the

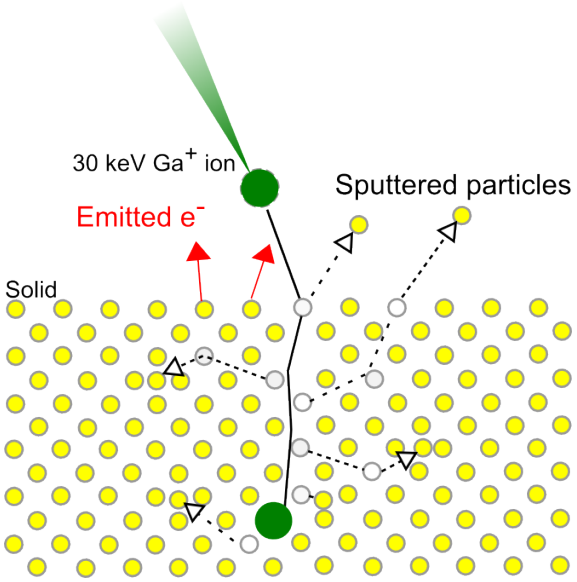

Figure 2.5: **Ion-solid interaction [83]**.

exception of electromagnetic radiation generation, all of these processes are important to FIB applications and are described in this section.

Ion kinetic energy and momentum are transferred to the solid through both inelastic and elastic interactions. In inelastic interactions, ion energy is lost to the electrons in the sample and results in ionization and the emission of electrons and electromagnetic radiation from the sample. In elastic interactions, ion energy is transferred as translational energy to target atoms and can result in damage and sputtering from the sample surface. The most widely accepted concept for ion–solid interactions is the collision cascade model [83–85](see Fig. 2.5). For the case of 5–30 keV Ga^+ ions bombarding most solids, the collision cascade involves a series of independent multiple collisions. If the translational energy transferred to a target atom during a collision exceeds a critical value called the displacement energy, the atom will be knocked out of its original site, for example, creating an interstitial–vacancy pair in a crystalline sample. This primary recoil atom may have sufficient energy to displace further sample atoms (secondary recoils), thus generating a volume where large numbers of atoms have excess kinetic energy. If a displacement collision occurs near the surface, the recoil atom may be emitted from the solid and lead to sputtering. The displacement energy (typically on the order of 20 eV) is much larger than the binding energy for the atoms (of the order of 1 eV), reflecting the fact that the collisions are nonadiabatic, because of the very short time scale. After approximately 10 ps, the 5–30 keV Ga^+ ion comes to rest in the solid, and the energies of

all particles participating in the cascade have decreased below the displacement energy. At this point, the collision cascade has ended. What remains are the emitted particles and radiation, and ion beam damage such as lattice defects, integrated Ga, and heat, all of which may continue to interact and evolve [81].

Based on the ion-solid interaction of FIB, there are three main working principles of FIB, namely (a) imaging, (b) milling, and (c) ion beam induced deposition [86], shown in Fig. 2.6.

Imaging: In a scanning electron microscope (SEM), the imaging signals can be generated from a number of electron induced processes including low energy secondary electrons, back-scattered high energy electrons, cathode luminescence, x-rays, and Auger electrons, all of which carry information about target topography or chemical composition. In the case of ion beams, the signals detected are low energy secondary electrons and/or secondary ions. Luminescence from the target has been seen as well. The secondary electron yield per incident ion is an important physical parameter in the FIB applications. Generally, the secondary electron emission by ion bombardment is much more sensitive to details of the surface structure of the target than in the SEM because the projection range of ions in the keV energy range is quite short. Many electrons are produced in collision processes between ions and target atoms, and because of momentum conservation, the electrons excited by the ions have rather low energies. The region of interaction is quite shallow and so the number of secondary electrons escaping from the surface of the target will grow with increasing angle between the target normal and the incident ion trajectory.

Since the low energy electrons produced deep below the surface cannot escape, FIB is especially sensitive to the surface topography. Low energy electrons will also be sensitive to the work function of the surface [87]. The FIB secondary electron signal will thus depend on the chemical nature of the surface as well as its morphology. This chemical effect will vary with target material, in particular there is invariably a secondary electron yield difference between oxides and clean elemental surfaces. The secondary electron yields for oxides are always higher than for metals [88, 89], as more low energy electrons will be able to surmount the surface barrier. Another feature differentiating FIB from SEM is the greater sensitivity of an incoming beam to the crystalline structure of the sample. In a crystalline sample it is possible for the primary ions to channel if the orientation of the crystal is aligned with the beam. In this case, the ions travel between the columns of atoms and their range can be quite large. Since a longer range implies

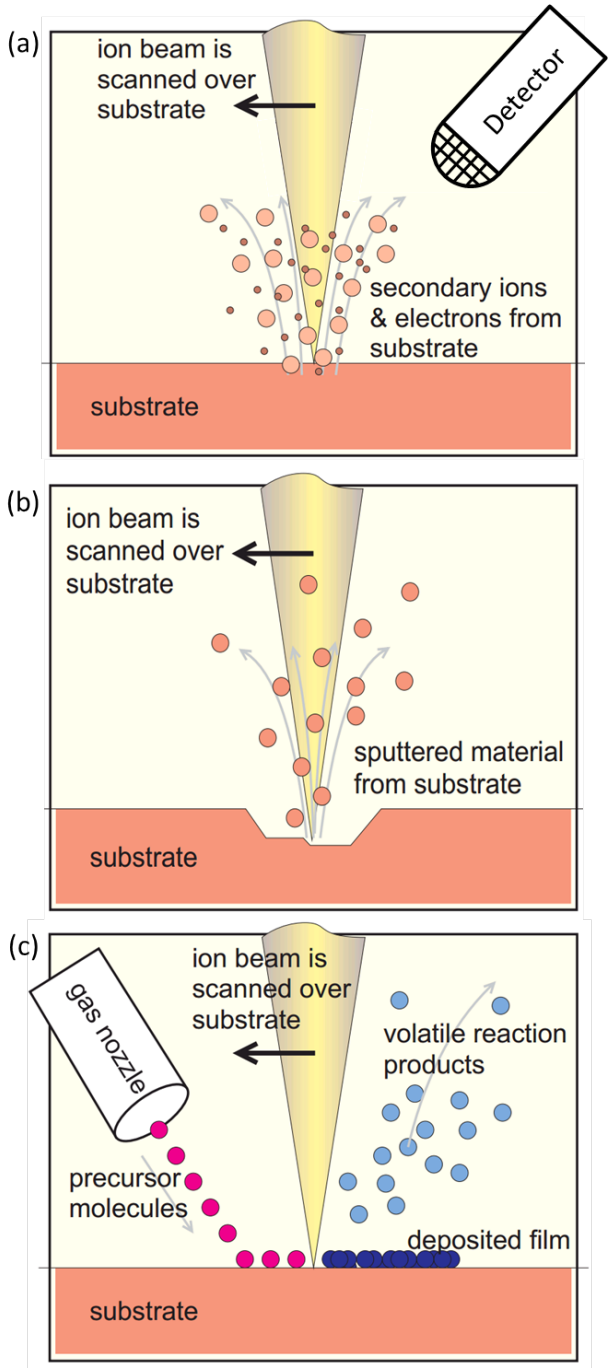

Figure 2.6: **Principle of FIB.** (a) Imaging, (b) milling and (c) ion beam induced deposition [86].

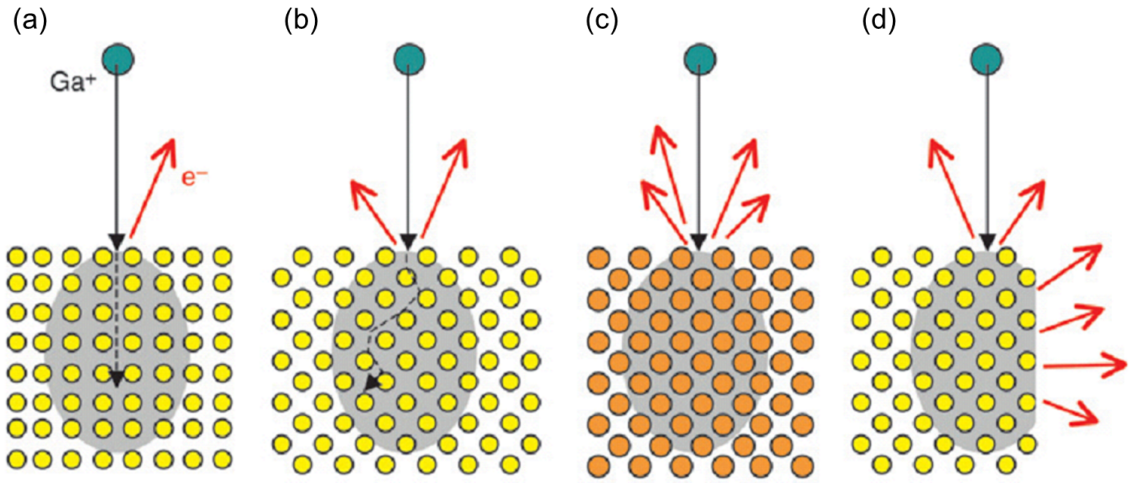

Figure 2.7: **The influence of crystal orientation, atomic mass, and surface geometry on 30 keV Ga^+ collision cascades and secondary electron generation.** The crystal orientation of a sample can affect the FIB sputtering rates, shown in (a) and (b). (c) The sputtering rate is also affected by the mass of the atoms (orange atoms are more massive) and (d) by the local geometry of the sample [83].

fewer interactions (per unit length) between ion and sample, the number of secondary electrons produced will be lower if the sample is oriented in certain directions relative to the beam. This effect induces image contrast variations depending on small changes of the angular orientation of the sample, which is called 'channeling contrast', shown in Fig. 2.7. The channeling contrast is being used for the observation of the grain structure [81, 83]. However, it is important to remember that ion beam imaging always results in some ion implantation and sputtering of the sample surface.

Milling: Ion milling is a method of material removal by means of physical sputtering phenomena. The sputtering process involves the transfer of momentum to surface and near-surface atoms from the incident ions through a series of collisions within the solid target. If the ion beam impinges on the target vertically there must be enough momentum reflected from the solid to eject one or more surface atoms. Therefore, the sputtering rate, which is defined as the ratio of the number of ejected atoms to the number of impinged ions, is a function of the angle of incidence of the ion beam as well as the mass and energy of the ions, the mass of the target atoms and the nature of the target atomic structure. FIB milling is carried out with repetitive scanning over a designated area. Arbitrary surface topologies can be created by controlling the scanning pattern, scanning location, and ion dosage. Typically, with a focused 30 keV Ga^+ ion beam of less than 5 nm diameter, structures with less than 30 nm features have been

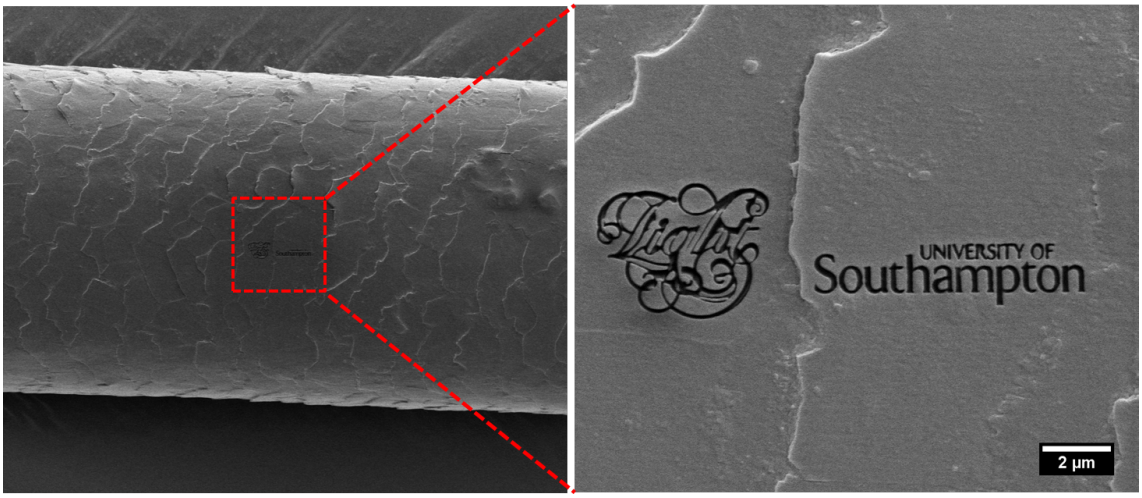

Figure 2.8: **SEM images of FIB milling results on a human hair.** An enlarged image of the structured area is shown on the right.

realized. Fig. 2.8 shows the logos of the Optoelectronics Research Centre and University of Southampton milled on a human hair, where the minimal milling line width is about 50 nm. The hair was coated with 10nm of gold in order to eliminate charging effects.

The FIB milling process can be further enhanced by introducing specific gas into the work chamber. It will increase the etching rate and the selectivity towards different materials by chemically facilitating the removal of reaction products. This technique is called gas-assisted etching. For example, XeF_2 can enhance the FIB etching rate of SiO_2 by a factor of 6 to 10 [86, 90].

Ion beam induced deposition: In contrast to ion milling, ion induced deposition is an additive process which is carried out by decomposing typically metal-bearing gas molecules adsorbed on the surface of the substrate with ion bombardment. The reactant gas, typically a metal organic compound, is delivered through a capillary nozzle which is pointed at the surface where the ion beam is incident. The molecules decomposed by ion bombardment are desorbed from the surface leaving metal atoms and forming a thin metal film on the surface. The decomposition of the precursor gas occurs only where the ion beams irradiates. Therefore, the film shape and thickness is determined by the FIB scanning pattern and dosage. An example of FIB induced deposition is shown in Fig. 2.9.

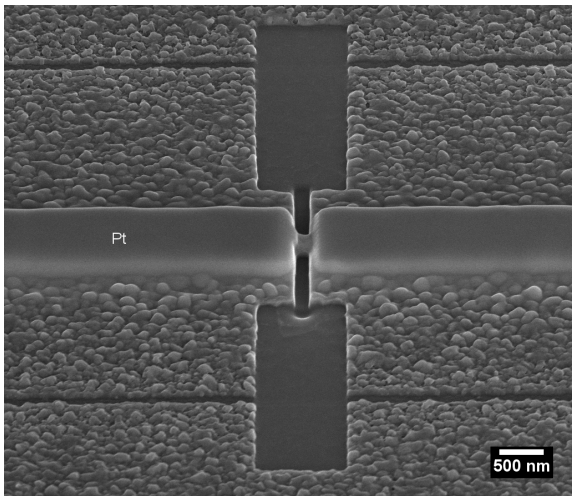

Figure 2.9: **SEM image of electrodes deposited by ion beam induced deposition.** The dark area is milled by FIB on 100nm of $Ge_{15}Sb_{85}$, and then two platinum (Pt) electrodes are deposited by ion beam induced deposition. The SEM image shows the structure as observed at 52° from the normal [91].

2.2.2 Focused Ion Beam System Architecture

The basic functions of the FIB, namely, imaging and sputtering with an ion beam, require a highly focused beam. The smaller the effective source size, the more tightly can the ion current be focused to a point. Unlike the broad ion beams generated from plasma sources, high-resolution ion beams are defined by the use of a field ionization source with a small effective source size on the order of 5 nm, therefore enabling the beam to be tightly focused. The most important components of the system are: the ion column, the work chamber, the vacuum system, the gas injection system and the computer controlled user interface [86].

The development of liquid metal ion sources (LMIS) has brought practical application of FIB technology to the semiconductor industry [83, 86]. Of the existing ion source types, the LMIS provides the brightest and most highly focused beam. There are a number of different types of LMIS sources, the most widely used being a Ga-based blunt needle source. Ga has clear advantages over other LMIS metals such as In, Bi, Sn, and Au because of its combination of low melting temperature (30°C), low volatility, and low vapor pressure. The low melting temperature makes the source easy to design and operate, and because Ga does not react with the material defining the needle (typically W) and evaporation is negligible, Ga-based LMISs are typically used for commercial FIB systems [81, 83].

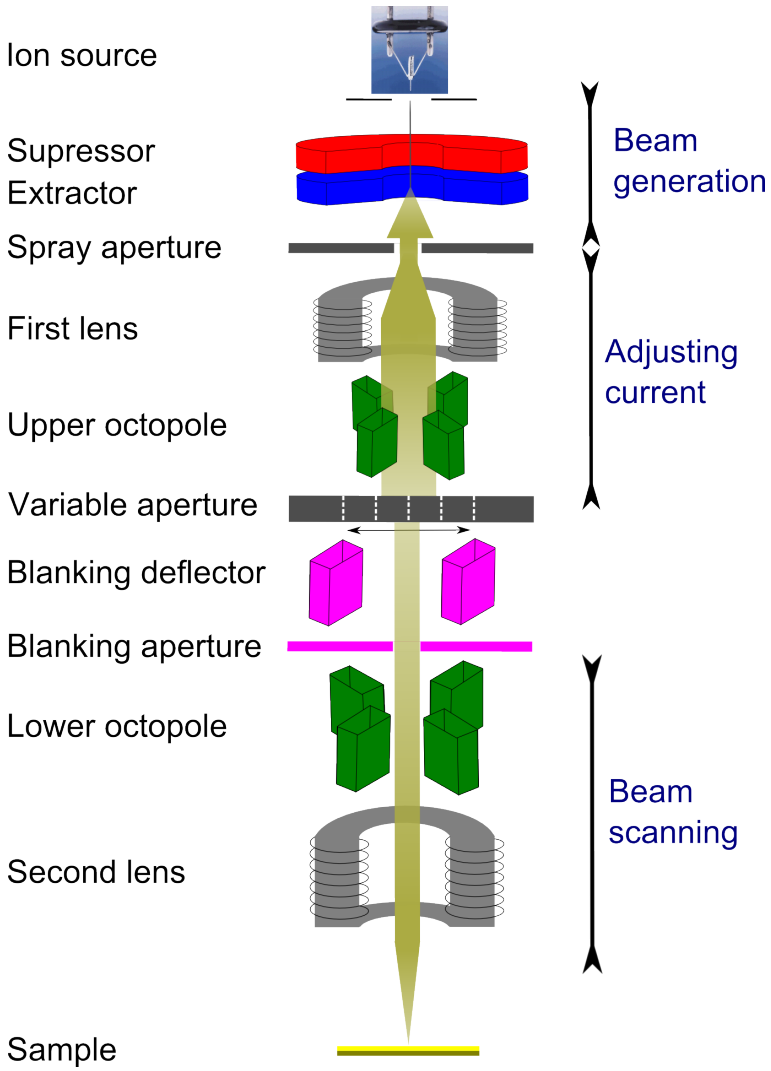

Figure 2.10: **Diagram of a FIB column** [86].

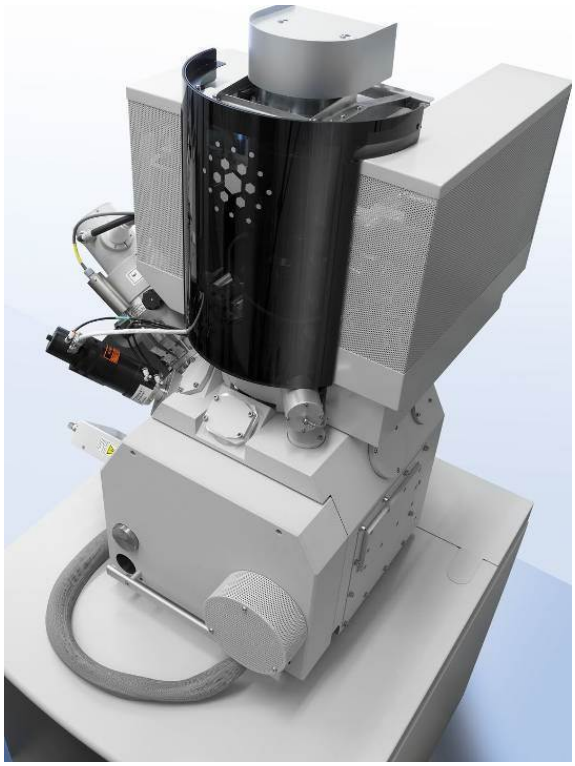

Figure 2.11: **Commercial Dual Beam^{TM} FIB-SEM system from FEI Ltd.** [94,95]**.**

A typical diagram of a FIB column is shown in Fig. 2.10. The structure of the column is similar to that of a scanning electron microscope (SEM), the major difference being the use of a gallium ion (Ga^+) beam instead of an electron beam. A vacuum of typically about 1×10^{-7} mbar is maintained inside the column by the vacuum system. After a first aperture, the ion beam is condensed by the first electrostatic lens. The upper octopole then adjusts the beam stigmatism. The ion beam energy is typically between 2 and 30 keV, with beam currents varying between 1 pA and 22 nA. Using the variable aperture mechanism, the beam current can be varied, allowing both a fine beam for high-resolution imaging on sensitive samples and a strong beam for fast and rough milling. Blanking of the beam is realized by the blanking deflector and aperture, while the lower octopole is used for raster scanning the beam over the sample in a user-defined pattern. In the second electrostatic lens, the beam is focused to a fine spot, enabling a best resolution in the sub 5 nm range. The Everhart-Thornley detector (ETD) [92] and Continuous Dynode Electron Multiplier (CDEM) [93] are used to collect secondary electrons and ions for imaging.

Imaging and milling with Ga^+ ions always result in Ga^+ ions interaction near the

sample surface. As the sample surface is sputtered away at a rate proportional to the sputtering yield and the ion flux, Ga^+ ions are implanted further into the sample. In order to minimize the ion implantation effects during sample searching and preparation, most modern FIB instruments supplement the FIB column with an additional SEM column so that the instrument becomes a versatile "dual-beam" platform, shown in Fig. 2.11. The ion beam and electron beam are placed in fixed positions and share their focal points at the "coincidence point," an optimized position for the majority of operations, including FIB sample direct writing [83]. The SEM part can be used not only to search and image the sample area for FIB processing but also to monitor the process of FIB milling in real time. Since SEM and FIB share the same working chamber and gas injection system in the FIB-SEM configuration, electron beam induced gas chemistry can be realized [90]. Furthermore, with further modification, even electron beam lithography (EBL) can be accomplished in the same instrument, in the other words, electron beam and ion beam lithography can both work in one instrument.

2.3 Focused Ion Beam Lithography Application Examples

Based on the knowledge of focused ion beam lithography from section 2.2, FIB lithography can be applied on many materials. In this section, several examples of photonic metamaterials and nanodevices fabricated by FIB lithography will be presented. I have been involved in at least the fabrication of each device which will be presented in this section.

2.3.1 Fabrication of Regular Photonic Metamaterials

Photonic metamaterials normally consist of two main bulk materials: metal (typically, gold or another plasmonic metal) and dielectric. Plasmonic metal is normally deposited on a dielectric substrate or thin film by physical vapor deposition (PVD). The general fabrication procedure is shown in Fig. 2.12.

FIB milling is very sensitive to the surface structure and crystal orientation, see section 2.2.1, therefore the deposition process plays an important role in photonic metamaterial fabrication. Fig. 2.13 shows metamaterial examples of FIB milling on poor and optimized gold surfaces. The FIB conditions are the same in both cases with 15ms dwell time and two writing passes. One can clearly see the grain boundary of gold in Fig. 2.13

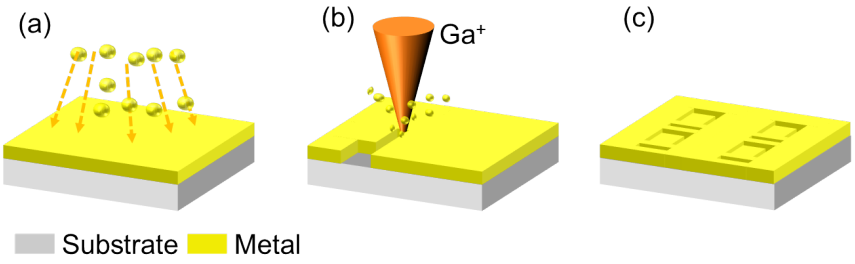

Figure 2.12: **Fabrication procedure of photonic metamaterials by FIB milling.** (a) Plasmonic metal deposited by PVD process. (b) Unwanted material removed by focused ion beam. (c) Desired photonic metamaterials structure.

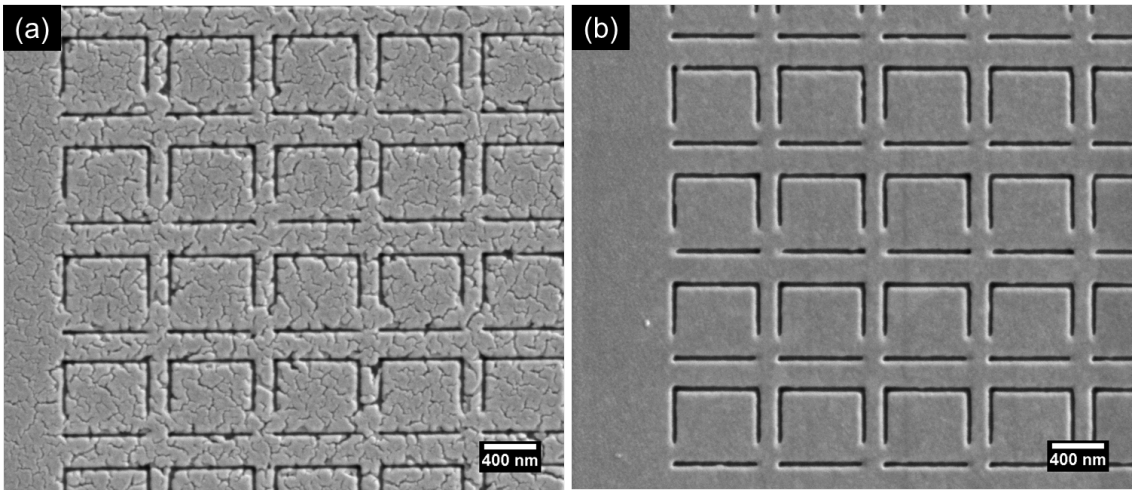

Figure 2.13: **Photonic metamaterials fabricated by FIB milling** on (a) poor and (b) optimized gold surfaces. Both of the metal films are 30nm thick and were deposited on silicon nidride by thermal evaporation.

(a) but not in Fig. 2.13 (b). The main difference between these two depositions is the deposition rate of gold which is about 0.2 nm/sec for the optimal case and 1 nm/sec for the poor quality case. Apparently, poor quality gold films cannot be used for high performance optical metamaterials. Examples presented in the following use optimized gold films in order to archive high quality photonic metamaterials.

Photonic metamaterial for quantum dot luminescence enhancement [96]: My contributions in this paper are the fabrication of various photonic metamaterials and the development of the quantum dot coating technique.

Control of Joule losses is a key challenge for plasmonic and metamaterial technologies. Although using superconducting metamaterials can largely eliminate losses in THz and microwave metamaterials [43, 48], Joule losses at optical frequencies are unavoidable.

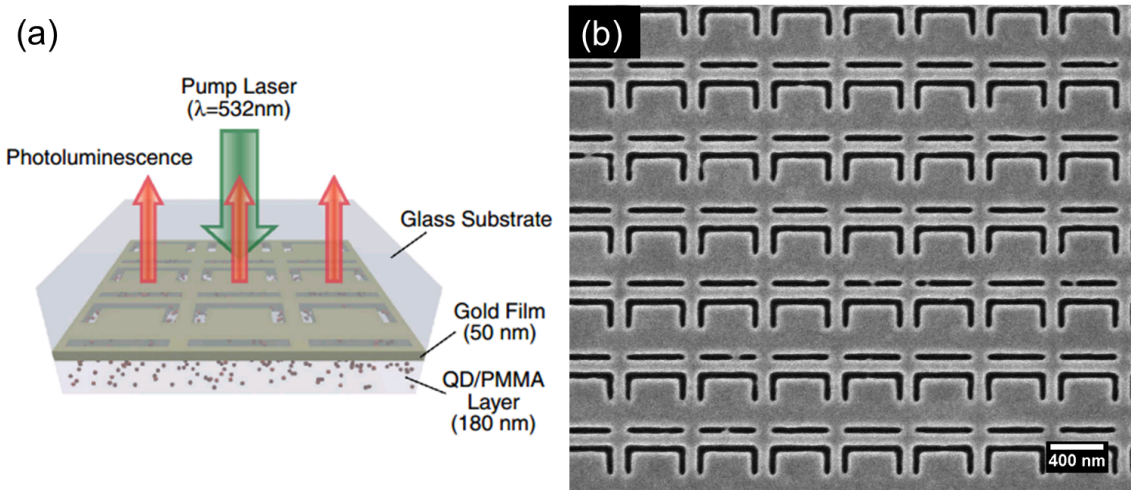

Figure 2.14: **Photonic metamaterials hybridized with quantum dots.** (a) Schematic of a plasmonic metamaterial functionalized with QDs. (b) SEM image of metamaterial aperture array with unit cell size of 545nm.

Recent works report compensation of losses with gain in plasmonic systems [97, 98], metamaterials aggregated with semiconductor quantum dots (QDs) [99], organic dyes embedded into metal nanostructures [100], and metamaterials manufactured on quantum wells [101]. In this work, we experimentally demonstrate that the photoluminescence properties of QDs can be greatly enhanced by the plasmonic metamaterial.

The photonic metamaterial aperture arrays with a total size of 40μm by 40μm were each fabricated by focused ion beam milling on a 50 nm-thick gold film thermally evaporated on a glass substrate, see Fig. 2.14 (b). Regarding FIB milling, the profile of a single point which is FIB milled into any substrate will partly be determined by the profile of the FIB itself. On the other hand, since the FIB immediately sputters away substrate material, a void forms while the FIB continues milling at the same position. Consequently, ions hit the sloped sidewalls of the forming void, especially at longer pixel dwell times. As sputter yields depend on the angle of the incident ions, milling rates depend on pixel dwell time. Another aspect that needs to be taken into consideration is the re-deposition of sputtered material that will occur inside the milled structures [102]. The FIB milling strategy here is using the 'parallel multi-passes milling' mode to eliminate redeposition of gold on the sidewall of metamaterial apertures. By using this strategy, I have pushed the minimum slit width of FIB milled photonic metamaterials to 25nm [103].

In order to systematically investigate the correlation between the QD photolumines-

cence spectrum and the spectral position of the Fano plasmonic metamaterial resonance, we manufactured five metamaterial arrays with different unit cell sizes ranging from 545 nm to 645 nm, with a slit width of 65 nm. We used lead sulfide (PbS) semiconductor quantum dots from Evident Technologies with a luminescence peak around 1300 nm and mean core diameter of 4.6 nm. These QDs were dispersed in polymethylmethacrylate (PMMA), and the QD/PMMA solution was then spin coated onto the metamaterial arrays, forming a 180 nm thick layer. We estimate the QD area density on the array to be 1.6×10^5 μm^{-2}, and thus approximately 4000 quantum dots are trapped in the grooves of each meta-molecule. Spectra (transmission, reflection, and absorption) and photoluminescence of the metamaterials with QDs were measured using a microspectrophotometer and it was found that the photoluminescence intensity was dramatically enhanced when the metamaterial was resonant at the QD emission wavelength. In this case, the Purcell enhancement factor for QDs within the metamaterial slits was estimated to be about 100.

Photonic metamaterial for enhanced terahertz bandwidth all-optical switching [28]: My contributions in this paper is development of fabrication procedure for large area (100 μm×100 μm) photonic metamaterials with various small unit cell sizes (smallest 330nm).

In this paper, we demonstrate a new strategy for achieving an extremely fast engineered optical nonlinearity through nanoscale periodic sub-wavelength patterning of thin metal films. This leads to a resonant, orders of magnitude enhancement of the cubic nonlinear response of the metal.

The nanostructure consists of a periodic array of asymmetric split ring slits cut through a 50 nm thick gold film thermally evaporated on a fused quartz substrate. The 100 μm × 100 μm metamaterial pattern was manufactured by focused ion beam milling, and is shown in Fig. 2.15. It is very challenging to manufacture such a big array with small unit cell size and without any stitching, as the writing field must be larger than the overall size of the metamaterial. Also, the resolution and stability must be kept in an acceptable range (less than few %) over a long writing time. The solutions are (1) A 16 bit DAC is used to generate such accurate patterns and to overcome part of the issues. For example, at 128 μm horizontal field of view, 128 μm can be divided into about 2 nm per pixel which means the precision of ion beam scanning is about 2 nm. (2) The stability of the ion beam is monitored and regulated within few % during the writing period of few hours.

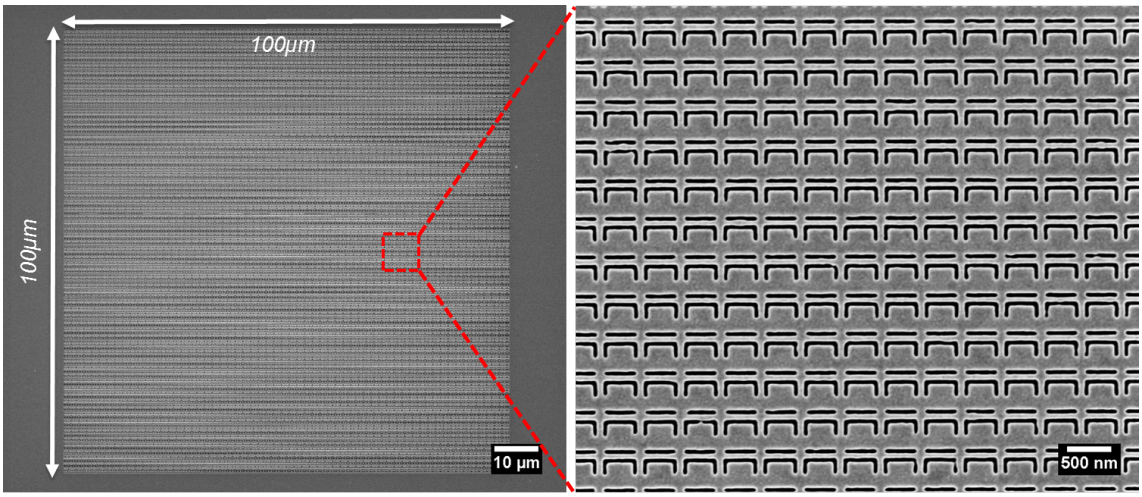

Figure 2.15: **SEM image of the photonic metamaterial aperture array for nonlinearity measurement.** The left image shows the total size of the metamaterial array of 100μm×100μm. The right one shows the enlarged metamaterial area, where the 450 nm unit cells are clearly visible.

Low-loss photonic metamaterial based on epitaxial gold monocrystal film [104]: In this paper, I contributed to epitaxially growing single crystal gold on lithium fluoride (LiF) crystal surfaces and manufacturing of photonic metamaterials.

The resonant nature of metamaterials is very sensitive to the presence of dissipative losses in the constituting metals. The losses are particularly strong in the optical regime hampering the use of metamaterials for photonic applications. The list of mainstream solutions considered at present includes, in particular, the search for better plasmonic media among metallic alloys, semiconductors and conductive oxides [105–107], as well as direct compensation of losses by combining metamaterials with various optical gain media [6, 96, 99, 101]. Those solutions, however, aim to eliminate or minimize Joule losses, while in practice dissipation rates are often much higher than expected from the Ohm's law alone. The additional significant contribution comes from surface roughness, grain boundary scattering and nanofabrication imperfections due to the polycrystalline nature of evaporated/sputtered metal films [71, 108, 109]. Nevertheless, the fabrication imperfections due to the nature of polycrystalline gold and the channeling effect [81, 83] of FIB milling appears in most fabrication results, see section 2.2 and Fig. 2.16 [109]. Therefore switching to monocrystals of noble metals alone should provide a substantial mileage in reducing losses.

Our crystal growth technique is based on epitaxial deposition, where metal vapor condenses on a crystalline substrate to a film with crystalline orientations closely related

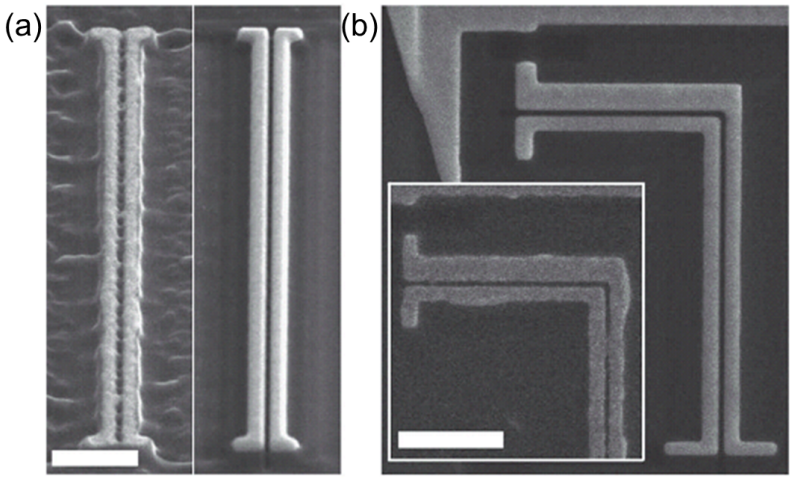

Figure 2.16: **SEM images of single- and multi-crystalline gold nanostructures.** (a) Prototype optical nanocircuits fabricated using FIB on a vapour-deposited multi-crystalline (left) and a single-crystalline gold flake deposited on a dip-coated ITosubstrate (right). The image was taken with a 52° tilt angle. (b) optical nanocircuits with a 90° corner fabricated with FIB on a multi-crystalline gold film, with a gap of about 28 nm between the two wires (inset) and a single-crystalline gold flake on top of a sputtered ITO substrate. Scale bars indicate 500 nm. [109]

to that of the substrate. Although large gold monocrystals can also be grown using the Czochralski process, they are usually difficult to obtain in the form of a thin film and therefore can be seldom considered for metamaterial and plasmonic device fabrication. Chemical synthesis process can grow gold flakes with areas of about 100 μm^2 [109], however, a more controlled deposition process is needed for general application. In the past, epitaxial growth of gold and other f.c.c. metals was demonstrated and thoroughly investigated for alkali-halide cubic crystals NaCl and KCl [110, 111]. In most of the cases, however, the growing procedure was complicated by the requirement of contaminating gases [112] or electron irradiation of the substrate [113], and often produced gold and silver films with (111) fibre texture [112, 114]. We have revisited the epitaxial growth techniques and found a combination of a substrate and deposition conditions that substantially simplified the procedure of growing gold monocrystals. As a substrate we used LiF. This ionic crystal has a face centered cubic lattice with the constant of 4.03 Å, which implies virtually no mismatch with the lattices of gold (less than 1.5%) and therefore results in a low interfacial energy for the parallel orientation of the gold film. Furthermore, LiF is a highly transparent dielectric with an exceptionally broad transmission window spanning from UV to mid-IR (0.15 to 6 μm) which makes it the ideal substrate for hosting metamaterial-based optical devices. A suitable (100) slab of LiF

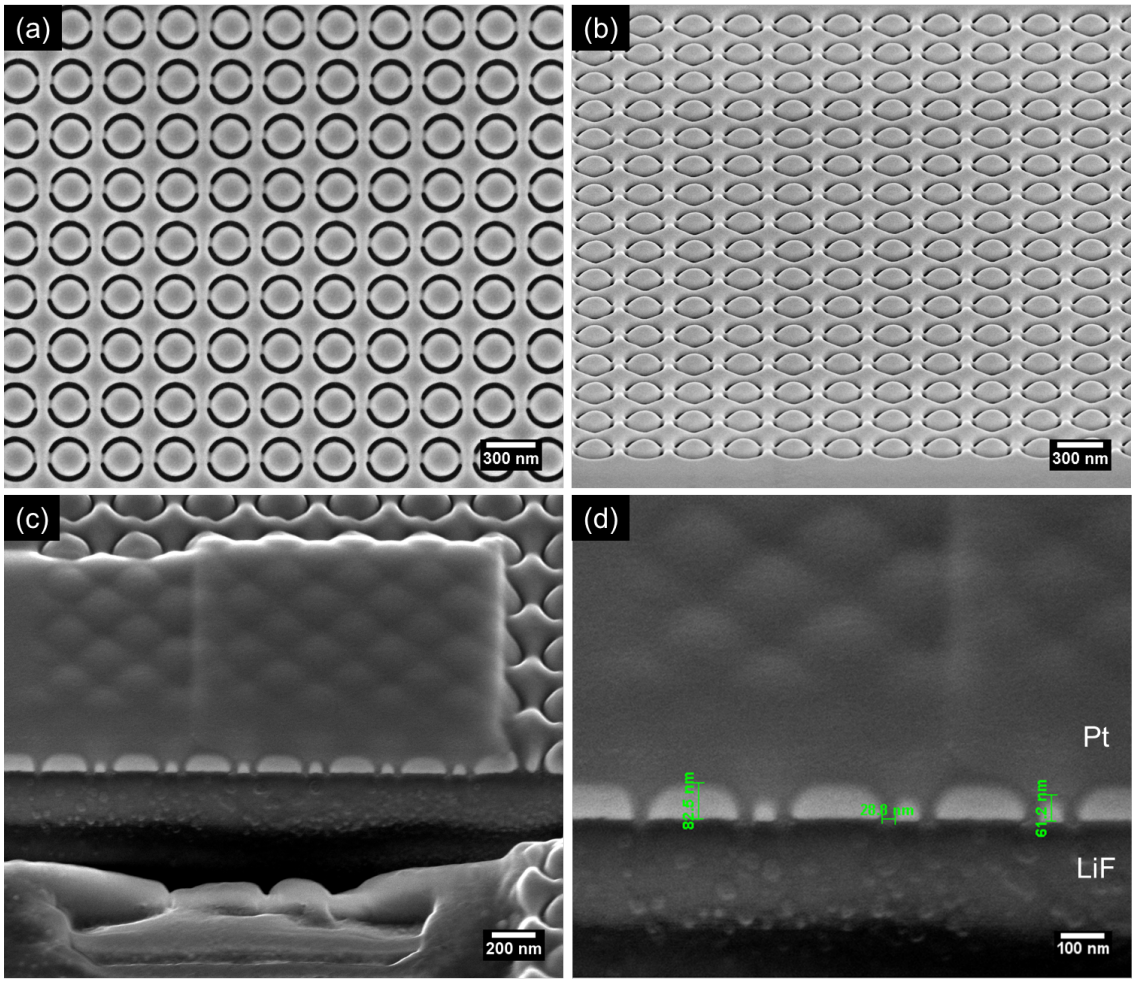

Figure 2.17: **High-finesse infrared plasmonic metamaterial.** (a) SEM image of complex asymmetrical split rings milled in epitaxial gold film. (b) shows the 52° tilted view of the milled structure. (c) and (d) show a cross section milled by FIB perpendicular to the arcs of asymmetrical split rings. Platinum (Pt) is deposited on top of the gold layer in order to get better image contrast.

was obtained by cleaving the crystal with a razor blade immediately before placing it in the high-vacuum sputtering chamber (Kurt J. Lesker sputter deposition system), where the slab was kept at 460°C during the deposition. Gold was deposited at the rate of 0.22 nm/min and base pressure of 5×10^{-6} mbar using a DC sputtering source. The sputtering produced an 80 nm thick continuous and atomically smooth film of a gold monocrystal with (100) domain orientation.

Here we have fully reproduced the shape of a well-known split ring microwave metamaterial pattern [115] on the nano-scale with the scaling ratio of about 47000:1, see Fig. 2.17 (a). The pattern was milled in the gold film using FIB, which produced metamate-

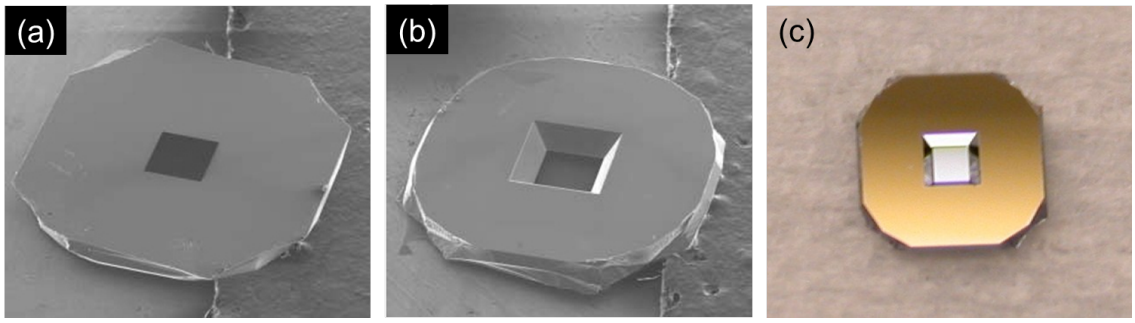

Figure 2.18: **Silicon nitride membrane.** (a) Top and (b) bottom view SEM images. (c) Optical image. The size of the outside frame is 3mm×3mm (From Norcada Ltd. [116]).

rial with the split rings defined by 30 nm wide circular slits (apertures). The rings had the diameter of 240 nm and were spaced 320 nm apart. The asymmetry of the pattern was optimized to yield a strong resonant response in the telecom range 1.3-1.5 μm: the two arcs of the split rings were 180° and 130° long and separated by equal splits of 25°. The metamaterial sample contained over 5000 sub-wavelength split ring resonators covering the area of about 23 μm × 23 μm. No defect due to redeposition or channeling is observed under SEM since the whole nanostructured area is a single crystal, see Fig. 2.17. However, re-conformation of the rim of structures resulted from FIB milling reducing the thickness of gold by about 20 nm between two neighboring split rings, see Fig. 2.17 (c) and (d).

2.3.2 Fabrication of Reconfigurable Photonic Metamaterials

Tuning of reconfigurable photonic metamaterial is realized in response to three different kinds of control signals: ambient temperature (Chapter 3), an applied voltage (Chapter 4) and a laser (Chapter 5). The realization of three types of reconfigurable photonic metamaterials and related fabrication techniques will be described and discussed in this section. The fabrication starts from a commercially available silicon nitride membrane supported by a silicon window in all cases, see Fig. 2.18.

Temperature-controlled reconfigurable photonic metamaterials: The concept of ambient temperature-controlled actuation of a NEMS cantilever/bridge is that a bilayer of two materials with different thermal expansion coefficients will bend upon temperature change , see section 3.2.1. For the cantilever type reconfigurable metamaterial, 50nm thick gold was thermally evaporated on a 100nm thick silicon nitride membrane. A “C”-slit plasmonic resonator pattern was milled from the silicon nitride side into the

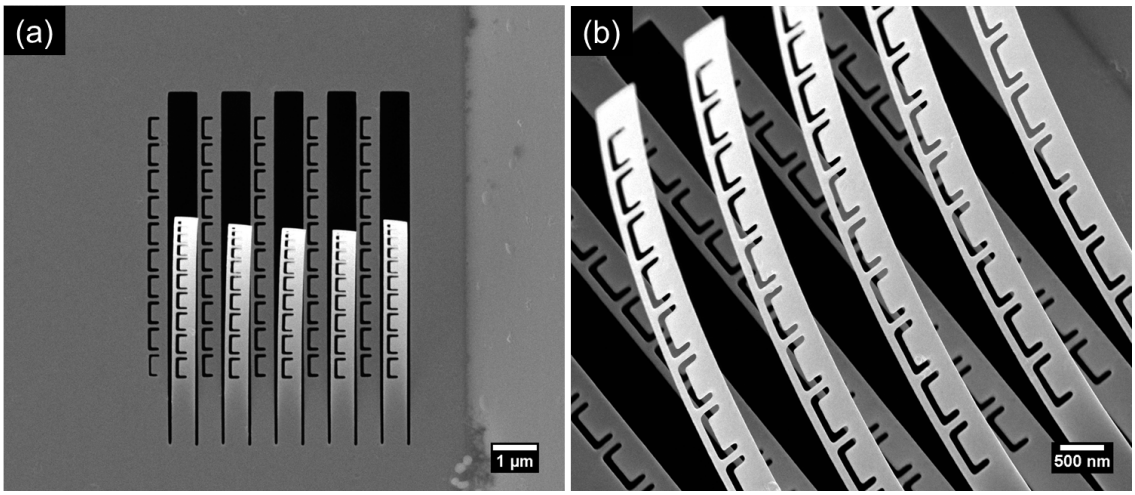

Figure 2.19: **SEM images of cantilever type thermally reconfigurable photonic metamaterial.** (a) Top view and (b) 52° tilted view of the milled structure. Images are taken from the silicon nitride side.

gold layer covering the back of the membrane. Next the metamaterial membrane was cut into 8 µm long and 525 nm wide bridges separated by 100 nm gaps. In order to create reconfigurable and non-reconfigurable support structures, one end of every second bridge was freed by FIB milling. The SEM images are taken from the silicon nitride side and the cantilevers bend out of the plane due to differential thermal expansion, between gold and silicon nitride, see Fig. 2.19.

The second type of temperature-controlled reconfigurable photonic metamaterial consists of reconfigurable and non-reconfigurable bridges that are fixed at both ends. Thermally reconfigurable support structures can be fabricated from a bi-layer consisting of two materials with different thermal expansion coefficients, for example a plasmonic metal and a dielectric. Bending of the bi-material structure will be caused by differential thermal expansion of the constituent materials. On the other hand, non-reconfigurable support structures can consist of either a single material or bending may be suppressed by using a symmetric sequence of layers such as metal-dielectric-metal. This concept will be discussed in detail in chapter 3. The fabrication process flow is shown in Fig. 2.20. The metamaterial consists of nanoscale "C"-shaped aperture plasmonic resonators (split rings) supported by alternating thermally reconfigurable and non-reconfigurable bridges. The entire structure was fabricated by focused ion beam milling from a 100 nm thick silicon nitride membrane covered by 50 nm thick thermally evaporated gold layers on both sides, shown in Fig. 2.20 (a). Next the "C"-slit plasmonic resonator pattern was milled into the gold layer covering the front of the membrane, Fig. 2.20

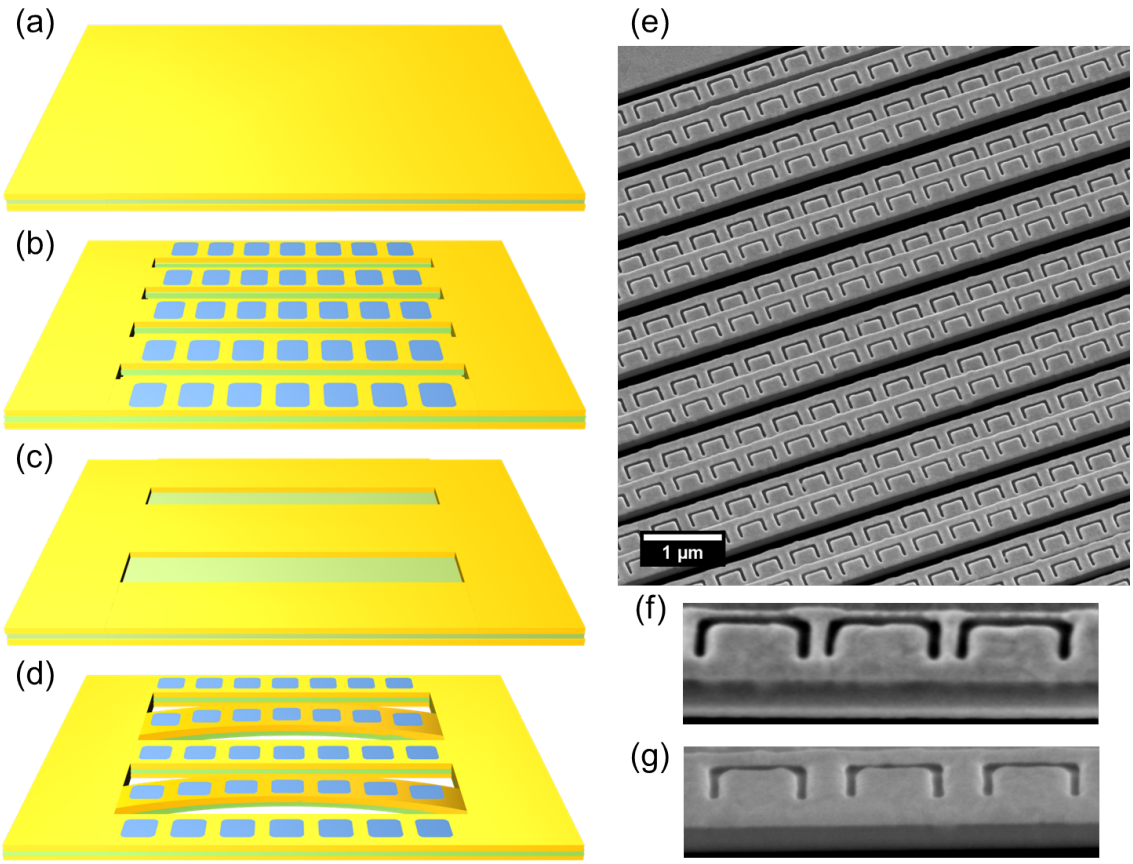

Figure 2.20: **Fabrication procedure of thermally controlled reconfigurable photonic metamaterials.** (a) 50 nm of gold is deposited on both sides of a 100 nm thick silicon nitride membrane. (b) "C"-slit plasmonic resonators are milled into the gold layer covering the front of the membrane. (c) The gold underlayer is removed from every second bridge. (d) The metamaterial membrane is cut into 50 µm long and 390 nm wide bridges separated by 110 nm gaps. (f) SEM image of the fabricated structure. (f) SEM image of a non-reconfigurable bridge showing the gold/silicon nitride/gold tri-layer structure. (gold layers are brighter) (g) SEM image of a reconfigurable bridge showing the gold/silicon nitride bi-layer structure.

(b). In order to create reconfigurable and non-reconfigurable support structures, the gold underlayer was removed from every second bridge, shown in Fig. 2.20 (c). And finally the metamaterial membrane was cut into 50 μm long and 390 nm wide bridges separated by 110 nm gaps, shown in Fig. 2.20 (d) and (e). SEM images are taken to confirm that the non-reconfigurable bridges consist of a gold/silicon/gold tri-layer, while the reconfigurable bridges consist of a gold/silicon nitride bi-layer, shown in Fig. 2.20 (f) and (g).

Electrostatically controlled reconfigurable metamaterial: As discussed in section 4.2.1, nano-electro-mechanical actuation can be realized based on electrostatic forces acting on the nanoscale. While the synchronous reconfiguration of sub-micron metamaterial blocks across large metamaterial arrays presents a formidable technological challenge, working on the nanoscale also gives some incredible opportunities by exploiting a changing balance of forces: as inertia of metamaterial elements and elastic forces scale differently with size, mechanical frequencies of the system are inversely proportional to its size reaching megahertz for mechanical structures 10s of microns in size. It appears that the electrostatic force, which is inversely proportional to the distance, becomes the dominant force at the nanoscale at potential difference of only a few volts and can drive such actuators. Another advantage of electrostatic forces is that the Joule losses associated with their engagement are small.

Fabrication starts with a commercially available 50 nm thick low stress silicon nitride membrane, a 50 nm thick gold layer for the plasmonic metamaterial and the contact electrodes was thermally evaporated through a shadow mask. The gold-coated membrane was structured with FIB, where the contact electrodes were connected to a source measurement unit (Keithley 2636) through a vacuum feedthrough for in-situ electrical characterization. Using FIB milling, first a "meander near the wire" pattern was milled to provide a continuous conductive pattern that supports a plasmonic resonance. Then the membrane was cut into suspended silicon nitride strings with tapered ends and finally the electrical terminals at the string ends were electrically separated by removing the gold film in selected areas, see Fig. 2.21. This structure is characterized in detail in chapter 4.

Optically controlled reconfigurable metamaterial: The fabrication of optically controlled reconfigurable photonic metamaterial is very similar to the electrostaticlly controlled one, but without electrical contacts. No electrical contact need to be considered in this case. The optomechanical photonic metamaterials studied here rely on

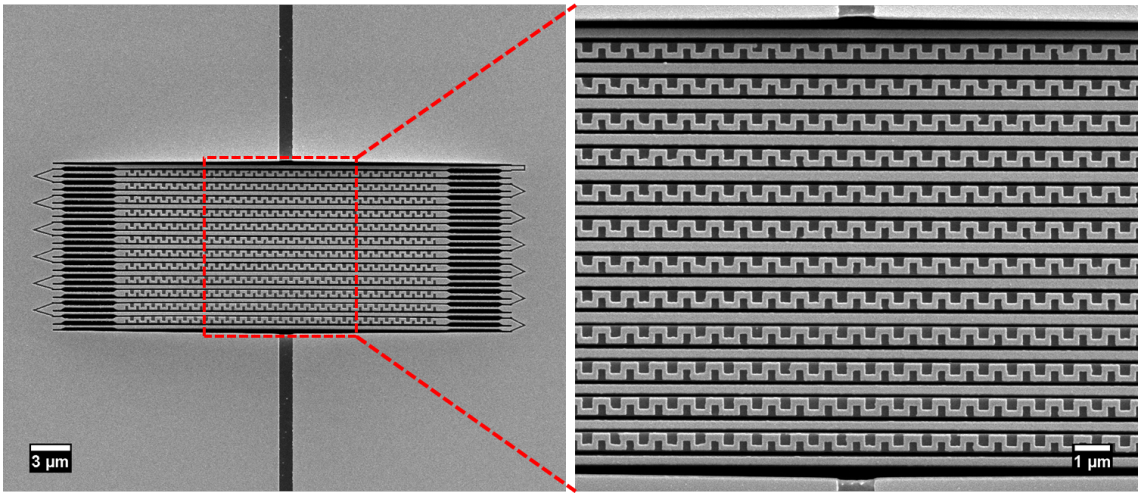

Figure 2.21: **SEM images of electrostatically controlled reconfigurable photonic metamaterial.** The right image shows the central part of the metamaterial. The brightest areas correspond to gold and the dark gray areas are silicon nitride.

the concepts introduced in section 5.2.1 and are based on a Π-shaped resonator design known for exhibiting plasmon-induced transparency [117, 118], see Fig. 2.22. In order to allow mechanical deformation of the plasmonic Π meta-molecules, the horizontal and vertical bars have been supported by different flexible dielectric bridges. The nanostructures were fabricated by FIB milling from a 50 nm thick silicon nitride membrane covered with a 50 nm thick thermally evaporated layer of gold. The unit cell is 700 nm × 700 nm in size and the supporting silicon nitride bridges are 28 μm long. This structure is characterized in detail in chapter 5.

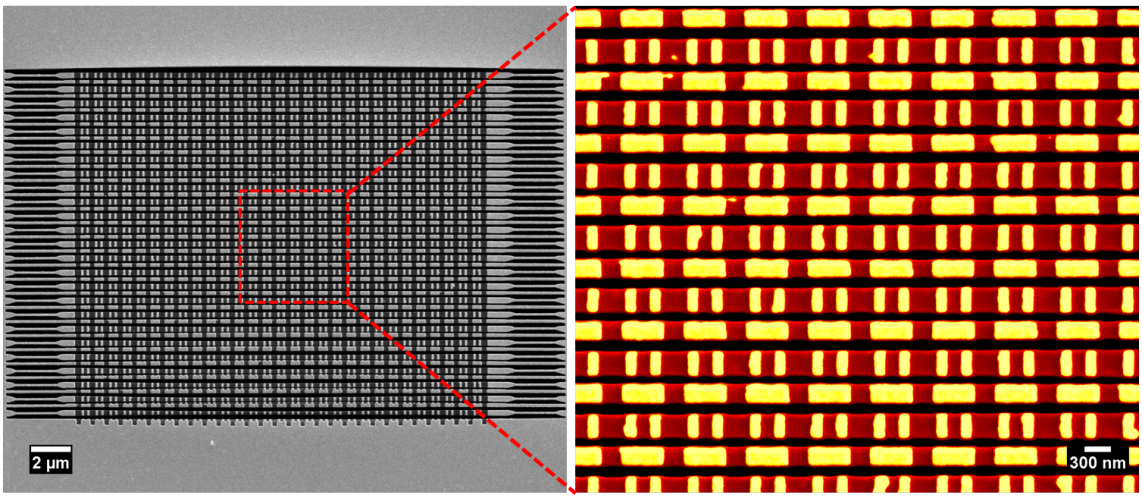

Figure 2.22: **SEM images of optically controlled reconfigurable photonic metamaterial.** False colour is used in zoom-in image to identify materials (gold coloured yellow and silicon nitride coloured dark red.).

2.3.3 Other Nanostructures and Nanodevices

The FIB system which I used for fabrication is a FIB-SEM configuration. Since the SEM and FIB share the same working chamber and gas injection system in the FIB-SEM configuration, electron/ion beam induced gas chemistry [90] and electron beam (e-beam) lithography can be realized in the same instrument. An example presented in this section shows a device fabricated by integration of e-beam lithography, FIB lithography, and e-beam induced gas deposition with alignment techniques.

Germanium antimony lateral nanowire phase change memory [119]: My contributions to this paper consist of developing a complex fabrication process involving FIB lithography plus e-beam lithography and partially characterizing the Ge-Sb lateral type phase change memory device.

The phase change technology behind the current rewritable optical disks and the latest generation of electronic memories has provided clear commercial and technological advances for the field of data storage; by virtue of the many key attributes chalcogenide materials offer [120]. In this work, germanium antimony (Ge-Sb) lateral nanowire phase change memory devices have been fabricated from thin films deposited by chemical vapor deposition (CVD). The fabricated devices have been characterized electrically demonstrating reversible phase change, while a lowering in power consumption in these memory cells is observed with scaling of the geometry of the nanowire cells. The results are investigated by electrothermal modeling to understand the temperature of the devices during

operation. These prototype CVD-grown Ge-Sb lateral nanowire devices show promise for applications such as phase-change memory and optical, electronic, and plasmonic switching.

The main target here is to make a nanowire type of phase change electronic device. For electrical measurement, one needs large area electrodes connected to the nanowire and external instruments; however, FIB milling is only good for fast prototyping in small areas. Therefore, we combine the FIB process for nanowire fabrication and interconnection between large electrodes and nanowire, and EBL plus metallization for large area electrodes. The fabrication process for Ge-Sb nanowire devices consists of five steps as shown in Fig. 2.23. Firstly, the Ge-Sb($Ge_{15}Sb_{85}$) thin films with thickness of 100 nm were prepared on SiO_2/Si substrates by the CVD technique as shown schematically in step A. Secondly, the Ti-W electrical contact pads with dimensions of about 45μm × 65 μm × 50nm were fabricated in combination of standard e-beam lithography and sputtering (using a Kurt J Lesker Nano38 RF Sputterer) in step B. Thirdly, the electrical isolation and Ge-Sb nanowires were milled by FIB in step C. Then, the Pt electrical contacts between Ti-W electrical contact pads and Ge-Sb nanowire were defined by electron beam induced deposition using the gas injection in the dual beam system in step D. Finally, the structure was covered by a protection layer of Si_3N_4 with thickness of 80 nm using standard e-beam lithography in combination with sputtering deposition in step E.

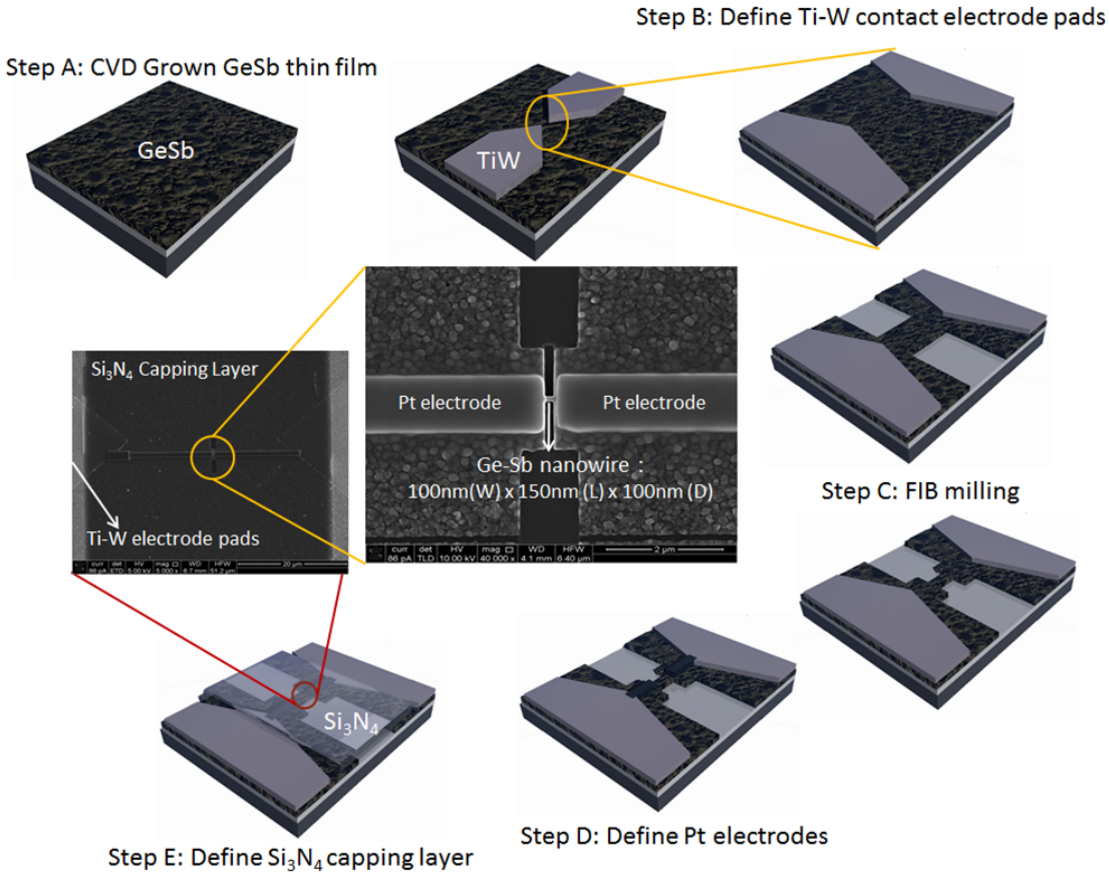

Figure 2.23: **Ge-Sb nanowire device fabrication process utilizing a top down approach.** The phase change film is deposited by CVD, contact pads defined by e-beam lithography and deposited via RF sputtering. Pt electrodes were deposited by e-beam assisted deposition while the nanowire is defined by focused ion beam (FIB) milling. The final capping layer is defined by e-beam lithography and deposited via RF sputtering [119].

3

Temperature Controlled Reconfigurable Photonic Metamaterials

3.1 Introduction

The work presented here is the result of a collaboration between the Optoelectronics Research Centre and the School of Engineering Sciences at University of Southampton. I have designed and fabricated the metamaterials and I have carried out the experiments. Furthermore, I have been involved in the interpretation of experimental results. Most of the following work has also been published as [46].

Temperature-controlled reconfigurable photonic metamaterials (RPMs) operating at visible and near-infrared frequencies require the development of components and actuators operating on the scale of a few tens of nanometers. Here we demonstrate that RPM nanostructures based on metal-dielectric films of nanoscale thickness provide a generic platform for achieving large-range continuous reversible tuning of metamaterial properties in the optical part of the spectrum. By placing metamaterial resonators (meta-molecules) on a thermally reconfigurable bi-material scaffold we control inter-metamolecular coupling leading to a profound reversible change of the metamaterial's transmission of up to 50%.

3.2 Towards Temperature Controlled Reconfigurable Photonic Metamaterials

3.2.1 Temperature Control of Bimaterial NEMS Cantilevers

A recent study on classifying MEMS/NEMS actuators into families based on their actuation principle and their performance provides a basis by which to identify areas of overall improvement in actuator design [121]. Electrothermal actuators in general, are particularly promising for delivering large displacements (1–100μm) and/or high forces (10–100μN). Thermal bimaterial actuators made by simple MEMS fabrication processes provide an easy means to obtain out-of-plane actuation which is otherwise difficult to achieve. Their actuation typically utilizes resistance heating of the actuator elements resulting in differential thermal expansion.

Several bimaterial electrothermal actuators have been studied: a diamond-like carbon/Ni microcage, a polymeric microgripper made of SU8 integrated with Ti/Pt and gold polyimide on silicon wafers have been suggested as biocompatible actuators for handling living cells in certain biomedical and biological applications [122]. Thermally actuated probe arrays made of gold on silicon nitride were used for nanolithography applications [123]. In all these applications, it is clear that the choice of materials has been largely driven by what was available to the designers rather than what should be considered for an optimal performance.

In metallic systems, the conduction electron charge density and the corresponding electromagnetic field can undergo plasmon oscillations. Because of the nature of the optical constants for noble metals such as gold and silver, the charge oscillations can propagate along the surface (rather than vanish evanescently) at optical frequencies. These surface plasmons can be excited by incident light in a process that depends on the dielectric constant of the material at the metal's surface [124]. In particles of dimensions on the order of the plasmon resonance wavelength, such as the meta-molecules of photonic metamaterials, this surface plasmon dominates the electromagnetic response. Therefore, we chose gold as a chemically inert good plasmonic metal with a relatively large thermal expansion coefficient (14.4×10^{-6}/K) as one layer for our bimaterial cantilever-based NEMS metamaterials. As the second bimaterial layer we chose silicon nitride(Si_3N_4) which is a dielectric with low thermal expansion coefficient (2.8×10^{-6}/K), which is avaliable in thin membranes.

The maximum free end slope of a bimaterial cantilever follows the relation [125]:

$$\theta = \frac{3}{2}(\Delta\alpha)\frac{L}{t}\Delta T \tag{3.1}$$

where $\Delta\alpha$ is the difference between the thermal expansion coefficients of the materials, L is the length of the bimaterial cantilever, t is the thickness of the cantilever and ΔT is a given temperature change. The maximum free end slope θ is a achieved for the optimum layer thickness ratio, which depends on the Young's modulus ratio (stiffness ratio) of the used cantilevers [125]. The optimum thickness ratio is satisfied by, for example, 37 nm gold on a 20 nm Si_3N_4 membrane. For example, a free end slope of 0.1 rad (6°) can be achieved with an aspect ratio of $L/t = 65$ and a temperature change (ΔT) of 200K (for optimum layer thicknesses of Si_3N_4 and Au). For the above thickness parameters, this corresponds to a cantilever length of 1.9μm. Reconfigurable elements fitting into meta-molecules for the visible/near infrared would have to be extremely thin and would be extremely difficult to achieve. Therefore we will focus on bimaterial structures supporting long strips of meta-molecules. This allows reconfigurable metamaterials for the visible/near infrared by removing the need for moving parts on the size scale of the unit cell, thus allowing substantial movement based on bimaterial structures of realistic total thickness on the order of 100 nm.

3.2.2 Reconfigurable Asymmetric Split Ring Resonators

Reconfigurable metamaterial structures have been pioneered in the GHz [44] and THz [16] spectral ranges. In the early work illustrated by section 1.2.2.2 Fig. 1.2(b) rapid thermal annealing has been used to lock split ring resonators in fixed tilted positions [16]. The same idea is applied to photonic metamaterials in this section.

Here, a first NEMS metamaterial test structure is discussed, which is based on asymmetric split rings (ASRs) and bimaterial NEMS cantilevers discussed in the previous section. The meta-molecules are asymmetric split rings with 900nm period and a 587nm $\times$ 437nm mechanical moving part based on a bimaterial cantilever consisting of a 37nm gold on 20nm Si_3N_4 bilayer, as discussed in section 3.2, see Fig. 3.1. The gold layer was formed by e-beam evaporation on a 20nm Si_3N_4 membrane and the structure was milled by FIB. After fabrication, the mechanical moving part naturally bent about -5° towards the Si_3N_4 side due to thermal expansion at room temperature. After 1 minute of 350 °C rapid thermal annealing (RTA) treatment, the moving part bent to 0° parallel to the

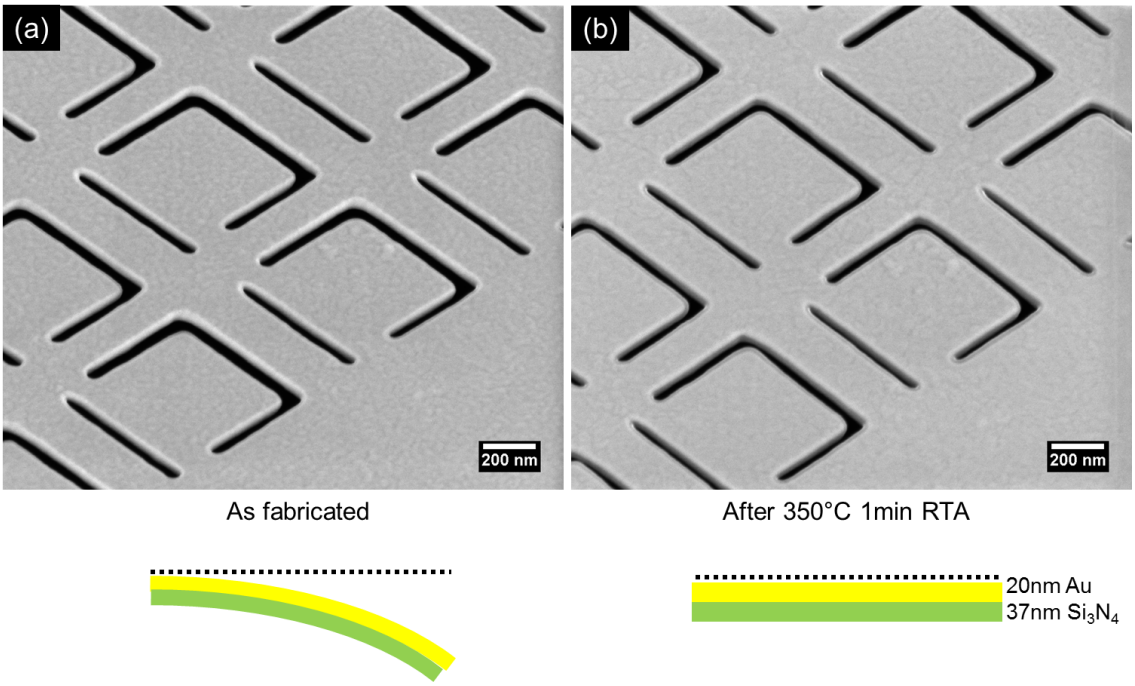

Figure 3.1: **Concept of reconfigurable asymmetric split rings.** SEM images and illustrations showing the meta-molecules (a) before and (b) after RTA.

metamaterial plane as the stress of the bimaterial was released by the RTA treatment. Fig. 3.2 measured by a microspectrophotometer (CRAIC Technologies) shows the difference between the structure before and after RTA. In detail, RTA treatment changes the wavelengths of the transmission maximum and reflection minimum near 1500nm by 47.7 nm and 24.4 nm respectively. Moreover, RTA changes the transmission and reflection intensity by 77.6 % and 4.35 % at the wavelength of 1538nm and the transmission difference ($\Delta T/T$) that resulted from RTA reaches more than 100 % as shown in Fig. 3.2 (b). RTA can introduce dramatic changes of the photonic metamaterial's optical properties by two factors: (i) RTA improves the quality factor of metamaterial resonances by gain size rearrangement of crystalline gold, see discussion in section 2.3.1. (ii) RTA changes the physical angle of moving part of meta-molecules, see Fig. 3.1. Nevertheless RTA can only lock the moving part of the meta-molecules in a certain position and continuous tuning cannot to be realized by RTA technique. In order to understand the possibilities of continuous tuning in this structure, temperature-dependent measurements were carried out.

The reconfigurable asymmetric split rings' temperature-dependent transmission spectrum, which is shown in Fig. 3.4, was measured using a microspectrophotometer (CRAIC

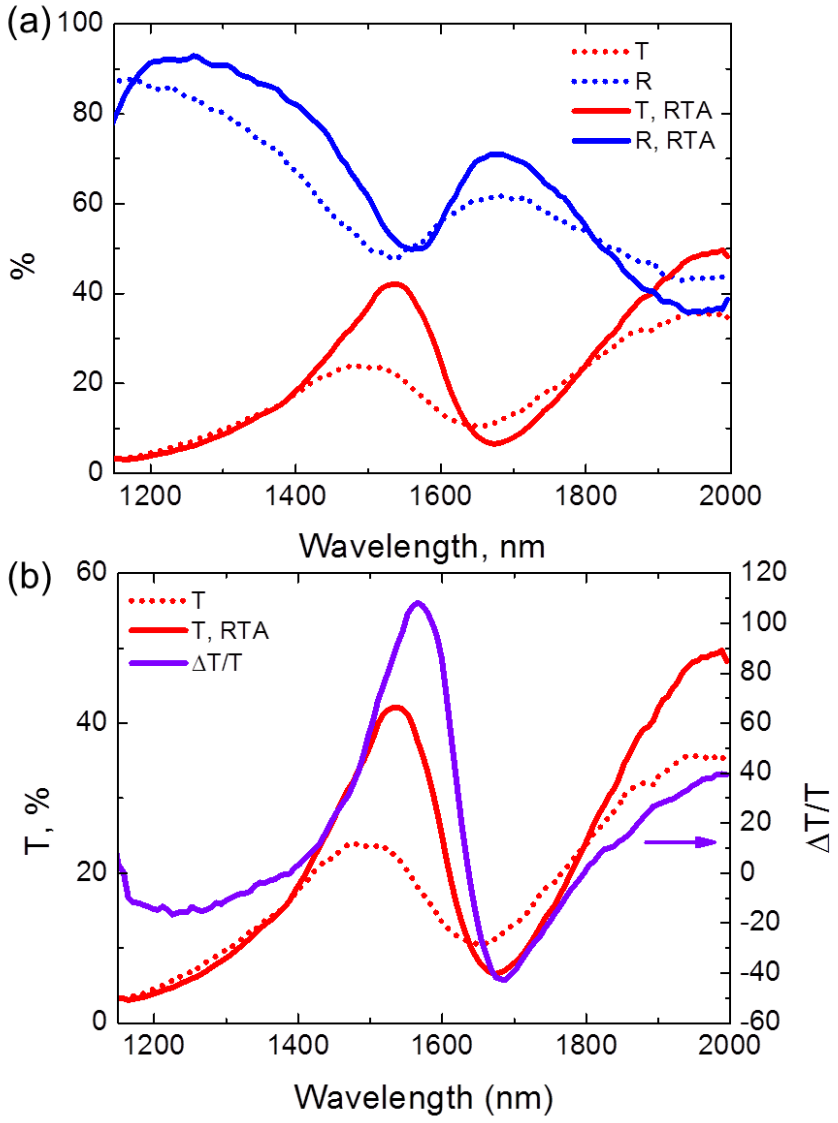

Figure 3.2: **Optical properties of reconfigurable split rings** for waves polarized perpendicular to the straight slit of ASR. (a) Transmission and reflection spectra of reconfigurable asymmetric split rings before and after RTA. (b) Transmission spectra before and after RTA and the relative transmission change.

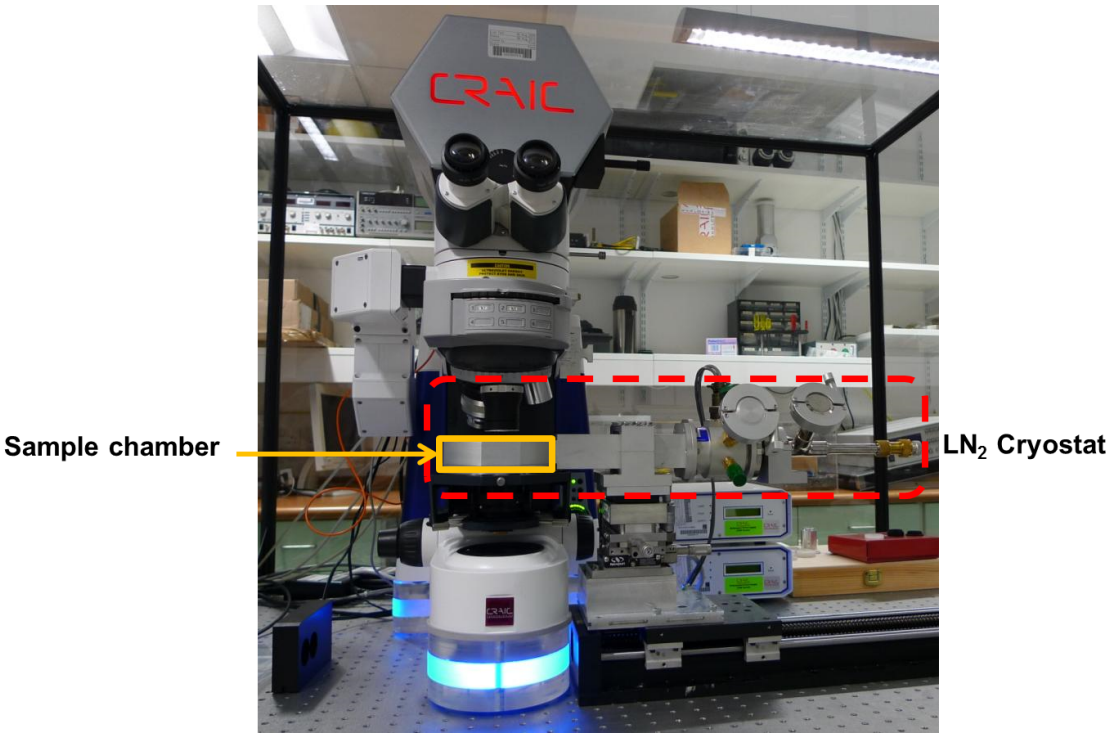

Figure 3.3: **Experimental setup for measuring temperature dependent optical spectra.** Microspectrophotometer equipped with a cryostatic sample stage.

Technologies) equipped with a cryostatic sample stage, see Fig. 3.3. In detail, the maximum transmission values vary from 22.3 % to 26.4 % depending on the ambient temperature of the sample, however, there is no clear tendency between transmission changes and differences of ambient temperature. Also, the wavelengths of the maximum transmission (peak positions) are fixed at 1531 nm. Based on these observations in Fig. 3.4, we conclude that the angle change of the moving part of the meta-molecules could be very small, with associated changes of the metamaterial's optical properties below the noise level of the spectrometer. The temperature dependent angle change of the moving part of the meta-molecules can be estimated by equation 3.1. In this case, a free end slope of only 0.036 rad (2.06°) can be achieved with the aspect ratio of $L/t = 10.3$ (length of moving part is 587nm) and a temperature change (ΔT) of 200 K (for optimum layer thicknesses of 20 nm Si_3N_4 and 37 nm of Au). The control experiment (RTA for metamaterial with no moving part) indicates that the RTA process mainly improves the quality of plasmonic metal films in reconfigurable metamaterial with short moving parts.

In order to obtain a larger free end slope, for example 0.1 rad (6°), with a temperature difference of 200 K and the above thickness parameters, a cantilever length of

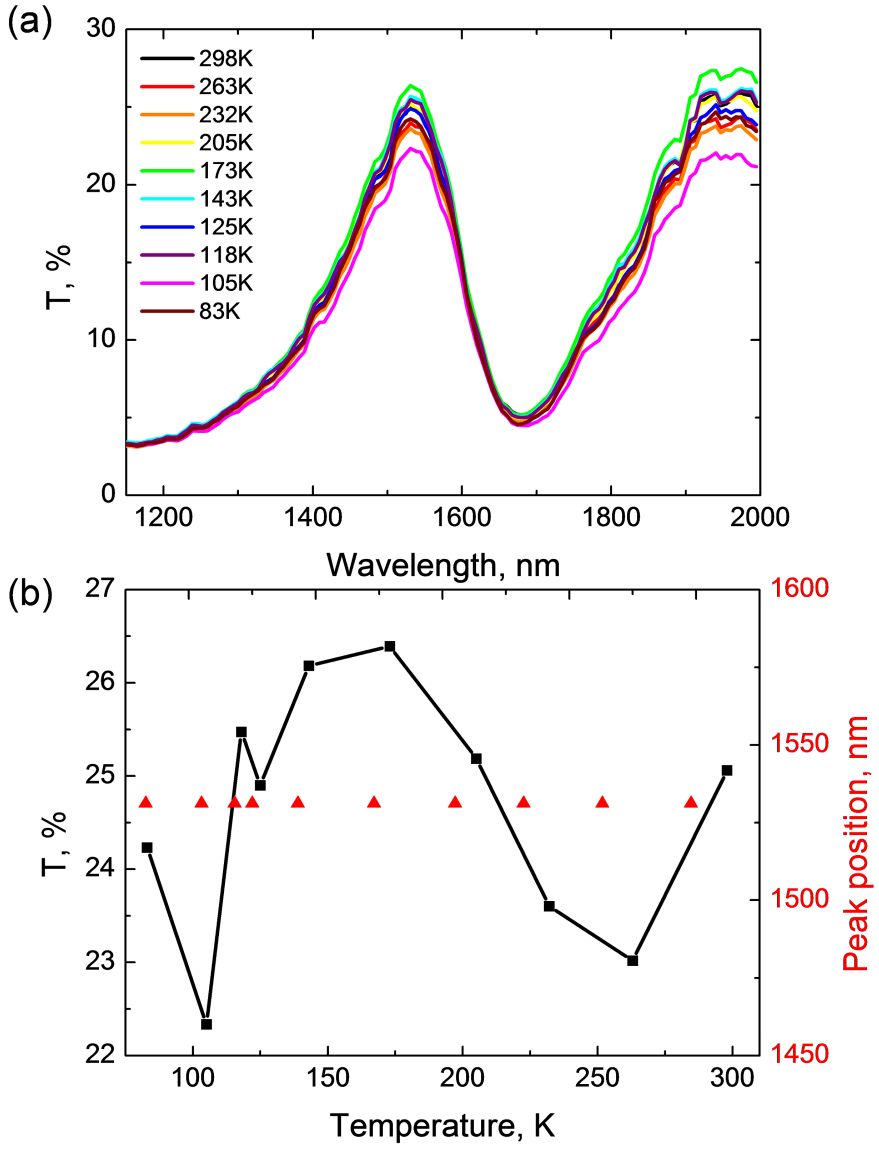

Figure 3.4: **Temperature dependent optical characteristics of reconfigurable asymmetric split rings.** (a) Transmission spectra of reconfigurable asymmetric split rings measured at various temperatures from 295 K to 83 K. (b) Temperature dependent maximum transmission and variation of maximum transmission peak positions.

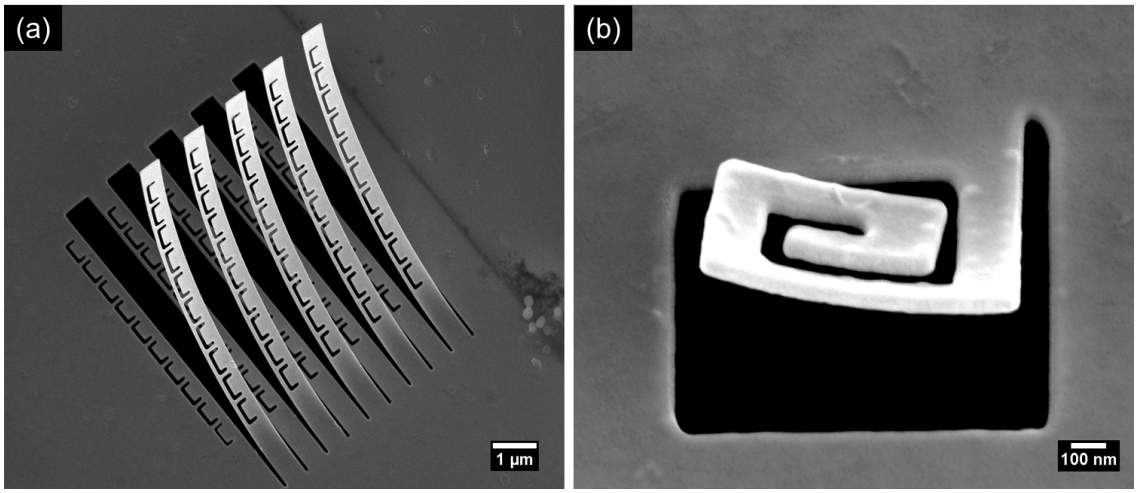

Figure 3.5: **Examples of cantilever type thermally reconfigurable photonic metamaterial.** (a) Meta-molecules supported by reconfigurable cantilevers and non-reconfigurable bridges. (b) A meta-molecule with longer cantilever. Images are taken from the silicon nitride side with a viewing angle of 52° from the normal.

1.9μm would be required. Reconfigurable elements fitting into meta-molecules for the visible/near infrared would have to be extremely thin and would be extremely difficult to achieve. Therefore, one can either increase the length of the moving cantilever within a meta-molecule or place meta-molecules on top of long support cantilevers in order to obtain larger angle differences upon ambient temperature changes, shown in Fig. 3.5. However, useful reconfigurable elements fitting into meta-molecules for the visible/near infrared would have to be extremely thin and would be extremely difficult to achieve.

3.2.3 Cantilever Type Reconfigurable Metamaterials

RPMs offer an opportunity to achieve precise control of metamaterial properties through mechanical deformation of nanoscale metamaterial structures. The difficulty of achieving a large deformation within an individual meta-molecule has been circumvented by placing nanoscale metamaterial resonators on 10s of micrometer long bimaterial cantilevers, which bend upon temperature changes. By alternating double-connected and single-connected cantilevers, we create locally periodic structures in which the distance (and thus coupling) between neighboring resonator strips is controlled by temperature. The cantilever-bending results from the different thermal expansion coefficients of the gold plasmonic resonators and the supporting silicon nitride membrane.

Fig. 3.6 illustrates this concept for the simplest case of simple rectangular plasmonic resonators cut by focused ion beam milling from a 50nm gold layer covering a 100nm

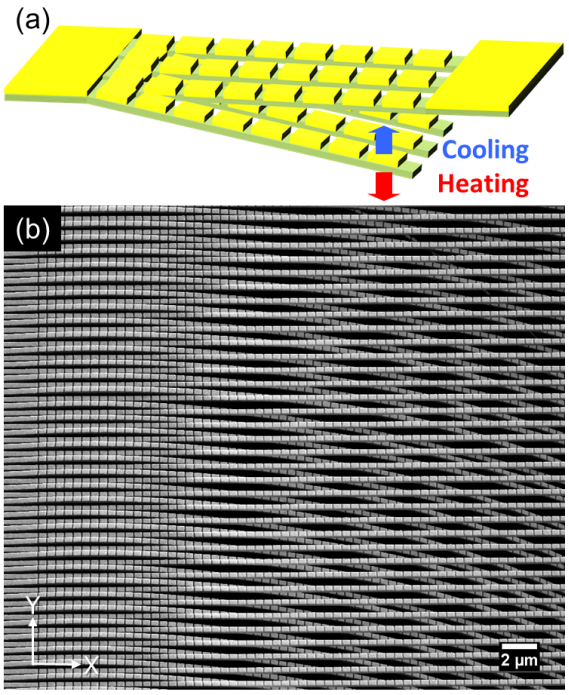

Figure 3.6: **Cantilever type locally periodic reconfigurable metamaterial with dipole resonators.** (a) Concept of thermally controlled cantilever type reconfigurable metamaterial. (b) SEM micrograph of the metamaterial consisting of 500nm×450nm×50nm gold dipole resonators fabricated by focused ion beam milling on a 100nm thick silicon nitride membrane.

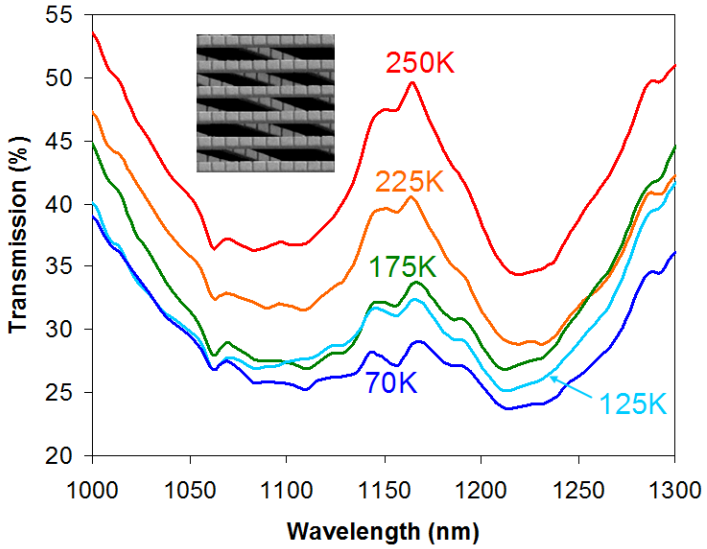

Figure 3.7: **Y-polarized transmission spectra as a function of temperature acquired close to the disconnected end of the cantilevers.** The inset shows the locally periodic 5µm×5µm measurement area.

thick silicon nitride membrane. The structure is periodic in the y-direction and locally periodic in the x-direction on length scales up to about 5µm. Fig. 3.7 illustrates for a measurement area close to the disconnected ends of the 50µm long cantilevers how dramatically the metamaterial properties depend on temperature. At a temperature of 250K two transmission resonances at 1100nm and 1220nm and a pass band in between can be clearly identified. As the temperature is decreased to 70K the disconnected end of the cantilevers bends towards the metamaterial membrane and the pass band vanishes almost completely, here the relative transmission change is -50%. The pass band recovers when the temperature is increased back to 250K, indicating reversible tuning. However, there is no clear spectrum shift resulting from temperature turning. A possible explanation is that the distance between resonators on supporting bridges and cantilevers is too far to introduce coupling effects between them, and the transmission difference results from either change of the length in a cavity between resonators or redirection of the light into another direction through structure bending.

Cantilever type RPMs give a chance to control tunability of metamaterials by temperature, however such long free end cantilevers are not very stable upon thermal cycles, see Fig. 3.8. Therefore we design more stable and more homogeneous supporting structures with two fixed ends for the temperature controlled RPMs which will be presented in the next section.

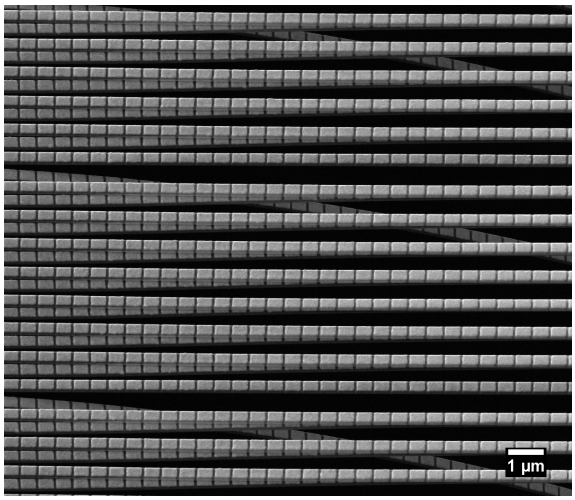

Figure 3.8: **Cantilever type reconfigurable metamaterial after few thermal cycles.**

3.3 Temperature Controlled Reconfigurable Photonic Metamaterials

3.3.1 Basic concept

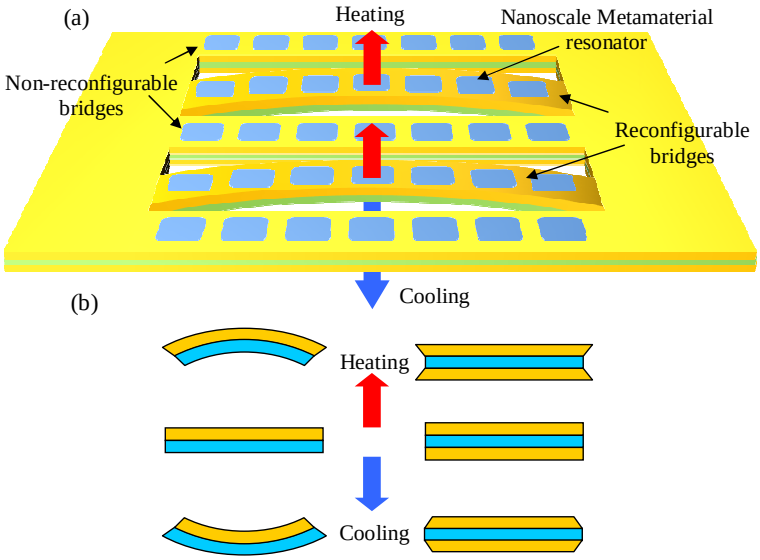

Figure 3.9: **Concept of thermally controlled metamaterial.** (a) Thermally tunable metamaterial support structure consisting of alternating reconfigurable and non-reconfigurable bi-material bridges. (b) Bi-layered support beams consisting of materials with large (orange, e.g. gold) and small (blue, e.g. silicon nitride) thermal expansion coefficients will bend in response to temperature changes, while bending is inhibited for a symmetric layer sequence.

The basic approach is illustrated by Fig. 3.9(a). Tunability will be introduced in almost any metamaterial system, if the distance and thus the coupling between neighboring meta-molecules can be controlled. For example, this may be achieved by placing the meta-molecules on alternating reconfigurable and non-reconfigurable support structures. This approach has two key advantages: (i) As it does not depend on the details of the meta-molecule design it is applicable to a huge range of metamaterial patterns. (ii) It eliminates the need for reconfigurable elements on the size scale of the meta-molecules, which would be extremely challenging to achieve for the optical part of the spectrum.

As illustrated by Fig. 3.9(b), thermally reconfigurable support structures can be fabricated from a bi-layer consisting of two materials with different thermal expansion coefficients, for example a plasmonic metal and a dielectric. Bending of the bi-material structure will be caused by differential thermal expansion of the constituent materials.

On the other hand, non-reconfigurable support structures can consist of either a single material or bending may be suppressed by using a symmetric sequence of layers such as metal-dielectric-metal.

3.3.2 Structure Description and Fabrication

Here we illustrate this concept for the reconfigurable photonic metamaterial shown in Fig. 3.10. It consists of nanoscale "C"-shaped aperture plasmonic resonators (split rings) supported by alternating thermally reconfigurable and non-reconfigurable bridges. Due to the patterned and unpatterned gold layers on their front and back, the "non-reconfigurable" support structures will bend slightly in the opposite direction to the "reconfigurable" support structures in response to changes of the ambient temperature. The entire structure was fabricated by focussed ion beam milling from a 100 nm thick silicon nitride membrane covered by 50 nm thick thermally evaporated gold layers on both sides. In order to create reconfigurable and non-reconfigurable support structures, the gold underlayer was removed from every second bridge. Next the "C"-slit plasmonic resonator pattern was milled into the gold layer covering the front of the membrane. And finally the metamaterial membrane was cut into 50 μm long and 390 nm wide bridges separated by 110 nm gaps. A more detailed description of the fabrication process is presented in section 2.3.2 and illustrated by Fig. 2.20.

Due to the large thermal expansion coefficient of gold (14.4×10^{-6}/K), which exceeds that of silicon nitride (2.8×10^{-6}/K) by a factor of 5, the metamaterial bridges without gold underlayer will arch upwards (downwards) upon heating (cooling) [125], see the lowered bridges in Fig. 3.10. On the other hand, thermal bending is suppressed for the more symmetric bridges with gold underlayer, which are raised in the scanning electron micrograph. We note that the metamaterial properties are position-dependent towards the end of the support structures, where the spacing between the metamaterial resonators gradually decreases. Therefore we investigated the central part of the structure, which is homogeneous and experiences the largest temperature-dependent changes.

3.3.3 Experimental results

The metamaterial's temperature-dependent transmission spectrum, which is shown in 3.11(a), was measured using a microspectrophotometer (CRAIC Technologies) equipped with a cryostatic sample stage, see Fig. 3.3. It reveals that the structure has resonant

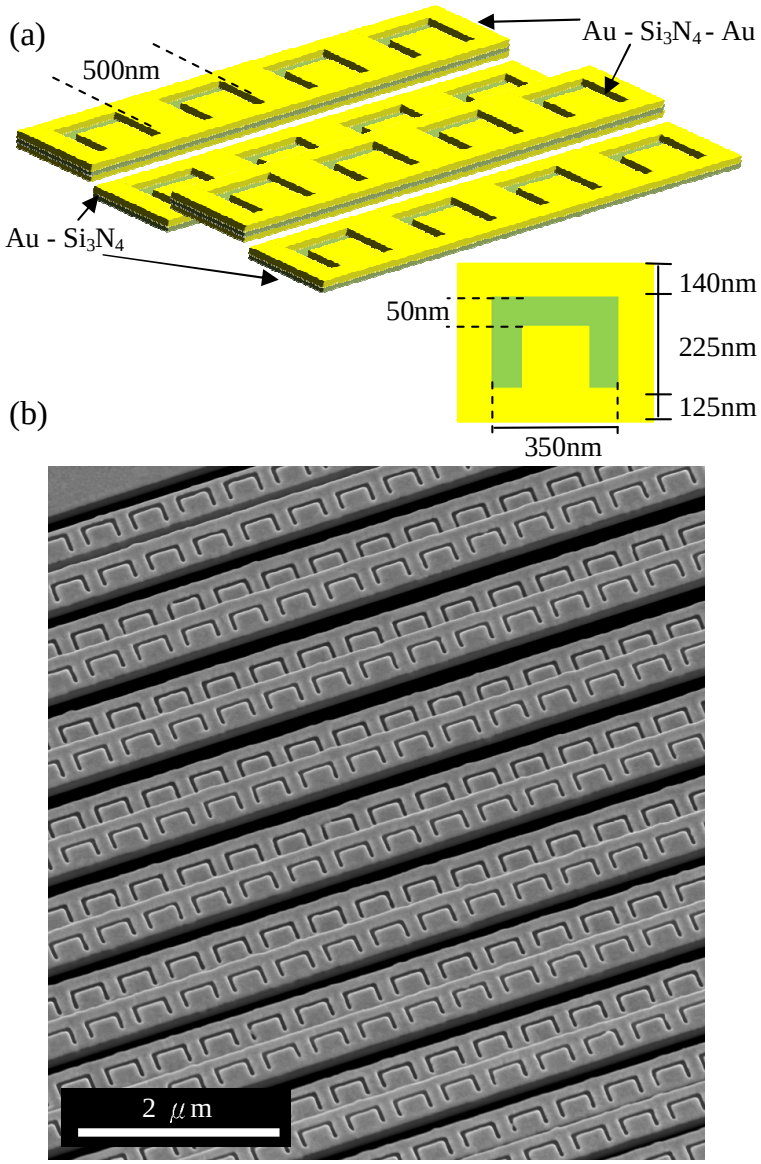

Figure 3.10: **Thermally controlled reconfigurable photonic metamaterial.** (a) Schematic with dimensions. (b) Scanning electron micrograph taken at room temperature.

transmission minima in the near infrared at about 1140, 1400 and 1670 nm. The resonant modes themselves are quite complex excitations of the coupled system of "C"-slit resonators and the gold underlayer on every second bridge. Importantly the resonant properties of this system strongly depend on the coupling between neighboring bridges and therefore a continuous change of the physical configuration of the nanostructure drives a dramatic change of its optical properties.

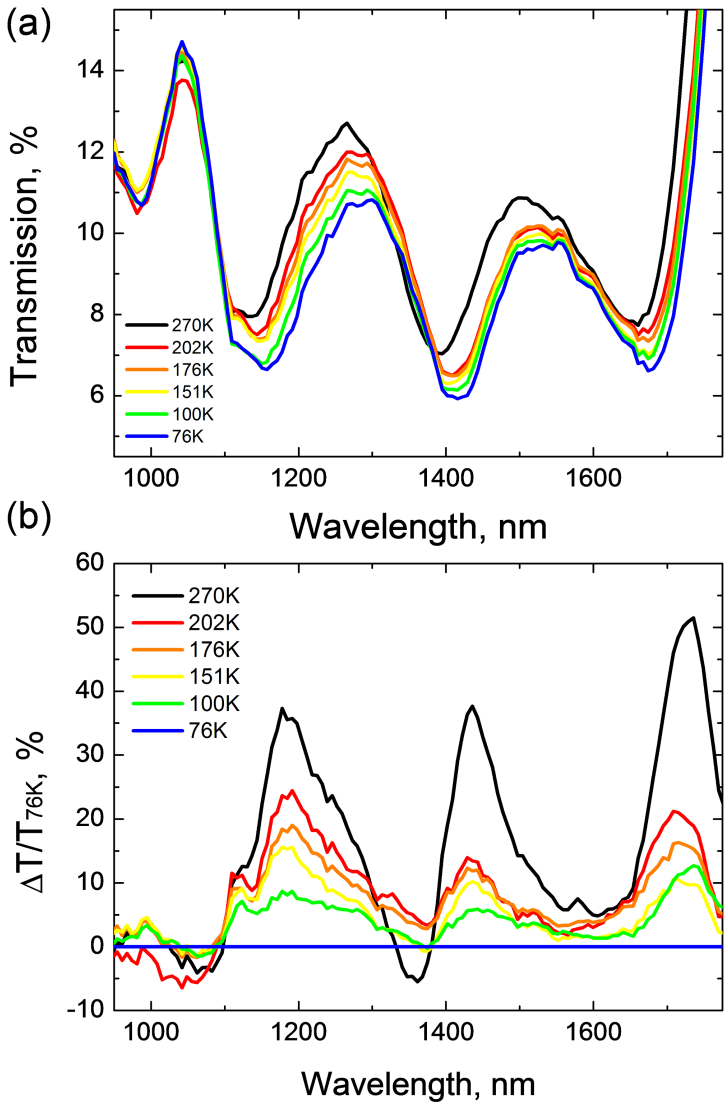

Figure 3.11: **Temperature dependence of the reconfigurable metamaterial's transmission characteristics** for waves polarized perpendicular to the supporting beams. (a) Transmission spectra measured at different temperatures. (b) Relative change of the metamaterial transmission normalized to a reference temperature of 76K.

Fig. 3.11(b) shows the change of the reconfigurable metamaterial's transmission characteristics relative to a reference temperature of 76K. As the metamaterial is heated to 270K, we observe dramatic 37%, 38% and 51% relative increases of its transmission near its resonant transmission minima at 1180, 1435 and 1735 nm, respectively. These remarkably large relative increases in transmission are due to a 20 nm blue-shift of the metamaterial spectrum combined with an overall transmission increase as the plasmonic resonators are moved closer together by differential thermal expansion driven by the

ambient temperature increase. Importantly, as the structure is cooled back to its initial temperature of 76K these changes of its transmission spectrum are reversed, indicating that the reconfigurable metamaterial returned to its initial state.

For practical applications, it may be important to achieve large-range tuning of metamaterial properties with much smaller temperature changes. This may be achieved with longer and thinner reconfigurable support structures and optimized material choices and layer thicknesses, as the mechanical tuning range of the reconfigurable bi-material beams is proportional to $\Delta T \Delta \alpha L/t$, where ΔT and $\Delta \alpha$ are the temperature and thermal expansion coefficient differences and L/t is the length/thickness aspect ratio of the support structures, see also section 3.2.1. We chose gold for its good plasmonic properties and silicon nitride for its easy availability in form of membranes of nanoscale thickness. However, silicon nitride could be replaced by glass, which has a significantly smaller thermal expansion coefficient of only 0.4×10^{-6}/K [125]. Furthermore, intermetamolecular coupling could be enhanced by placing the supporting beams closer together and the relative thermal displacement of neighboring resonators could be doubled by alternating metal-on-dielectric and dielectric-on-metal reconfigurable structures, which would bend in opposite directions.

3.4 Electro-Thermal Control

Indeed, reconfigurable photonic metamaterials provide a flexible platform for the realization of tunable metamaterials for the optical part of the spectrum. By placing nanoscale plasmonic resonators with useful functionalities at optical frequencies on reconfigurable support structures, their interaction can be controlled, which leads to large-range tunability of the system's electromagnetic properties. Although the control of metamaterial properties by ambient temperature may be suitable for some application such as sensors, it is impractical in most applications.

In this section we will focus on electrothermal control, where the resonator spacing is controlled via thermal expansion of the supporting structure resulting from Joule heating by an applied electrical current. The concept is illustrated by Fig. 3.12. Here, we use "meander"-shaped and "wire" plasmonic resonators as an example, however, it is possible to replace "meander" and "wire" plasmonic resonators with any other kind of plasmonic resonators for which tunability is needed. The supporting structure spacing is controlled via thermal expansion resulting from Joule heating by an applied electrical current.

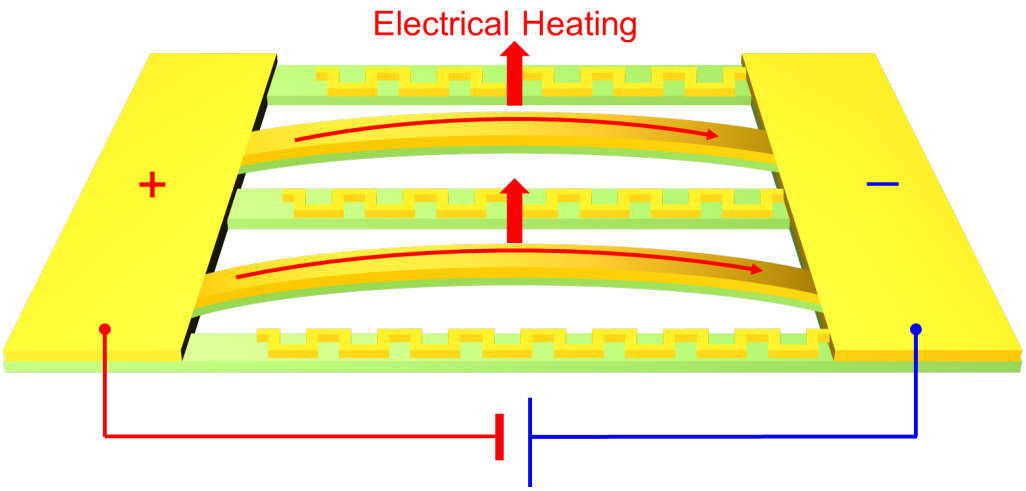

Figure 3.12: **The concept of electrothermally controlled RPMs.** The supporting structure spacing is controlled via thermal expansion resulting from Joule heating by an applied electrical current. When electrical current is applied to alternating supporting beams, the supporting bimaterial beams lift because of local heating induced bending. The temperature difference between current-carrying supporting beams and isolated supporting beams controls the distance of neighboring supporting beams.

When electrical current is applied to "wire" beams, the supporting bimaterial beams lift because of local heating induced bending. The temperature difference between current-carrying supporting beams (wire) and isolated supporting beams (meander) controls the distance of neighboring supporting beams.

An example of an electrothermally controlled reconfigurable photonic metamaterial is shown in Fig. 3.13. It consists of 35 μm long silicon nitride bridges alternatingly covered with nanoscale "meander"-shaped plasmonic resonators and straight wires. The entire

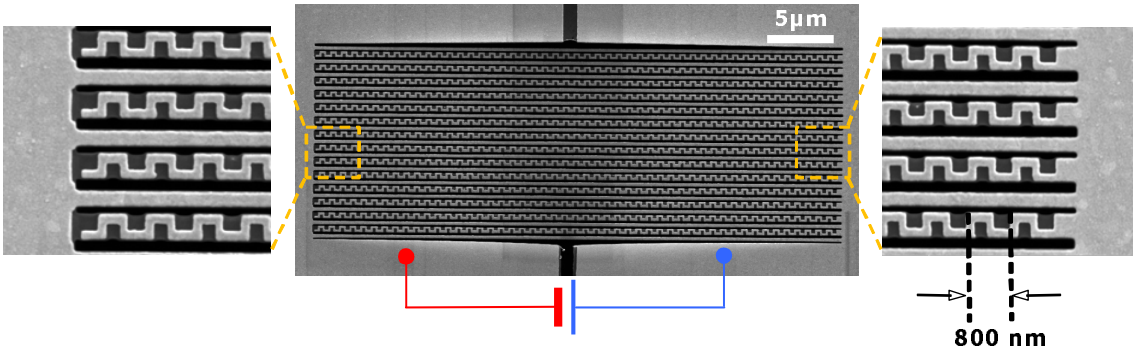

Figure 3.13: **Realization of an electrothermally controlled RPM.** Scanning electron micrograph with insets showing the electrical connections at the ends of the support structures.

structure was fabricated by focussed ion beam milling from a 50 nm thick silicon nitride membrane covered by a 50 nm thick thermally evaporated gold layer. The bridges are separated by 125 nm gaps for electrical isolation and every second bridge is connected to both electrical contacts for electrothermal control of the device.

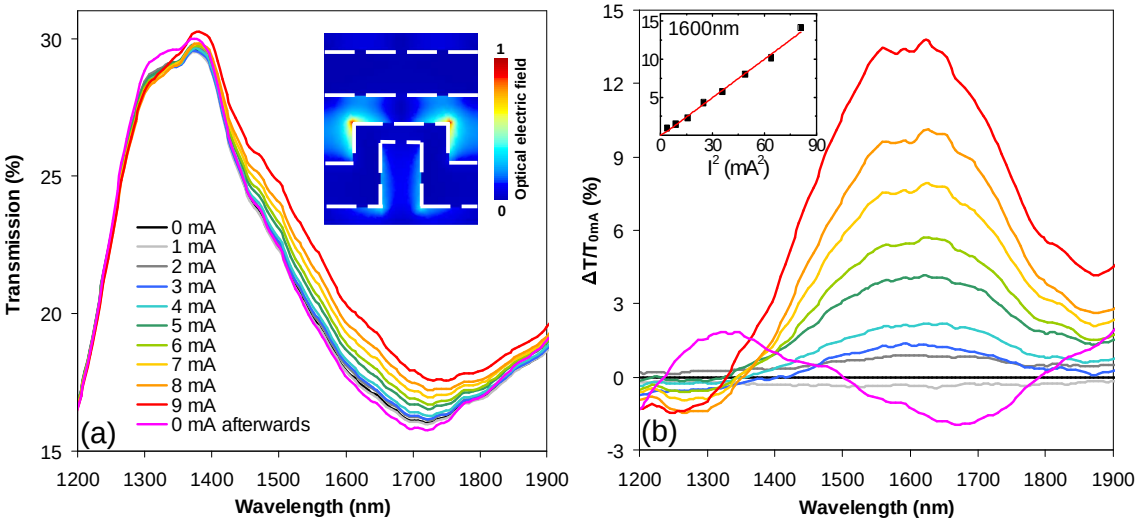

Figure 3.14: **Electrical current dependence of the electrothermally reconfigurable metamaterial's transmission characteristics** for waves polarized perpendicular to the supporting beams. (a) Transmission spectra measured at different electrical currents. (b) Relative change of the metamaterial transmission normalized to a reference current of 0 mA.

Preliminary results are presented by Fig. 3.14 and discussed in this paragraph. A current applied to the metamaterial device raises the local temperature of the electrically connected "wire-bridges" relative to the electrically disconnected "meander" bridges. When the electrical current is increased, the local temperature of the gold wires increases resulting a transmission increase around the wavelength of 1600 nm as shown in Fig. 3.14 (a). Fig. 3.14(b) shows the change of the electrothermally reconfigurable metamaterial's transmission characteristics relative to the reference case of 0 mA applied current. As the applied current is increased to 9 mA, we observe a substantial 14% relative increase of the metamaterial's transmission near its resonant transmission minimum at 1600 nm. This large relative increase in transmission is due to a red-shift of the metamaterial spectrum combined with an overall transmission increase as the plasmonic resonators are moved further apart by differential thermal expansion driven by the electrical current induced local temperature increase. The heated gold wires move up relative to the nearby

meander bridges due to their higher temperature and more complete gold coverage (gold expands more than silicon nitride). Importantly, as the applied current is reduced back to 0 mA these changes of the metamaterial's transmission spectrum are reversed, indicating that the electrothermal reconfigurable metamaterial returned to its initial state.

3.5 Conclusion

In conclusion, using bi-material layers one can construct a planar metamaterial which is reconfigurable via the ambient temperature or electric heating due to differential thermal expansion. One could manufacture rows of resonators on alternating metal-on-dielectric and dielectric-on-metal support structures, which would bend in opposite directions in response to temperature changes, thus driving a change of the nanostructure's physical configuration and optical properties. Specifically we have realized a thermally controlled reconfigurable photonic metamaterial exhibiting reversible relative changes in transmission of up to 50 %.

4

Electrostatically Controlled Reconfigurable Photonic Metamaterials

4.1 Introduction

In this chapter, I have designed and manufactured the electrostatically controlled metamaterials and carried out the experiments. Furthermore, I have been involved in the interpretation of experimental results. Most of the work has also been published as [126].

Tuning, switching and modulating metamaterial properties in the visible and near-infrared range remain major technological challenges: the existing microelectromechanical solutions for the sub-THz [41] and THz [17–19] regimes cannot be shrunk by 2-3 orders of magnitude to enter the optical spectral range. By using the temperature-controlled reconfigurable metamaterial reported in chapter 3, one can easily access the optical range. However, temperature control is inherently slow as it is limited by the device cooling time scale. Detailed calculations based on the law of heat conduction and literature values for the thermal properties of 50 nm thick films of gold [127] and silicon nitride [128] predict conductive cooling timescales on the order of 20-30 μs, implying that thermal modulation processes become inefficient at 10s of kHz.

Here we develop a new type of metamaterial operating in the optical part of the spectrum which is 3-4 orders of magnitude faster than previously reported electrically reconfigurable metamaterials [17–19]. Moreover, the operation speed is not limited by the thermal time scale of the nanostructures reported in chapter 3. The metamaterial is actuated by electrostatic forces arising from the application of only a few volts to its nanoscale building blocks, the plasmonic meta-molecules, which are supported by pairs of parallel strings cut from a nanoscale thickness flexible silicon nitride membrane.

These strings of picogram mass can be synchronously driven to megahertz frequencies to electromechanically reconfigure the meta-molecules and dramatically change the metamaterial's transmission and reflection spectra. The metamaterial's colossal electro-optical response allows for both fast continuous tuning of its optical properties (up to 8% optical signal modulation at up to megahertz rates) and high-contrast irreversible switching in a device of only 100 nm thickness without the need for external polarizers and analyzers.

Engineering fast, dynamically reconfigurable metamaterials for the optical spectral range with meta-molecular features on the scale of tens of nanometers is a formidable technological challenge, however, working on the nanoscale also has some important advantages as the electrostatic force, which is inversely proportional to distance, becomes dominant, allowing potential differences of only a few volts to overcome the elastic response of suitable nanostructures. Moreover, inertial and elastic forces scale differently with size, driving mechanical frequencies of microscale reconfigurable elements to megahertz values. Existing electrically reconfigurable THz metamaterials, however, where external comb-drive actuators drive the mass of the entire metamaterial [17–19], would not allow high-frequency operation even if they could be scaled to the optical spectral range. Similarly, approaches based on deformation of elastomeric substrates [53] lead to low resonance frequencies as they require macroscopic displacement of a comparatively high mass of low stiffness material.

4.2 Towards Electrostatically Controlled Reconfigurable Photonic Metamaterials

4.2.1 Electrostatic Control of NEMS Actuation

Elastic nanostructures can also be moved by electrostatic forces between electrically charged objects. At the nanoscale, a small voltage of e.g. 1 V applied across a narrow gap of e.g. 100 nm leads to exceptionally large electric fields on the order of 10 MV/m and thus significant electrostatic forces acting on small charged objects. The electrostatically actuated tuning and switching characteristics can be easily understood theoretically. For a simple estimate in the electrostatic (low frequency) limit we may consider the equilibrium of elastic restoring force and electrostatic attraction between two elastic support structures separated by a gap g. The restoring force is $F_r = k(g_0 - g)/2$, where g_0 is the

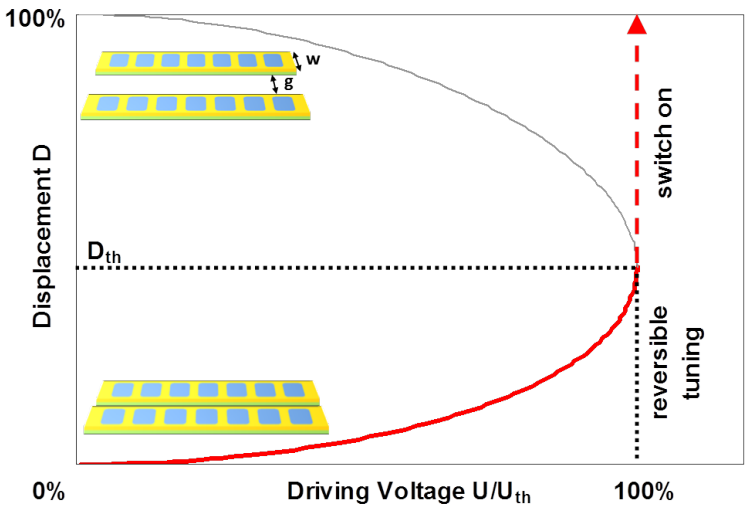

Figure 4.1: **Electrostatically actuated bridge beam.** Bridge displacement D (normalized by half of the initial gap size $g_0/2$) as a function of the voltage applied to a pair of parallel bridge beams.

initial gap size and $k = 32Etw^3/L^3$ [129] is the spring constant for lateral displacement of a bridge beam that is connected on both ends, with Young's modulus E and bridge thickness t, width w and length L. It can be shown from Gauss law that the electrostatic force between two parallel wires with charge Q is $F_e = Q^2/(2\pi\varepsilon_0 L(g+w))$ and their gap-dependent capacitance (which determines Q) is $C = Q/U = \pi\varepsilon_0 L/\cosh^{-1}(1+g/w)$, where U is the applied voltage [130]. From $F_r = F_e$ follows that

$$U = U_0\sqrt{D(1+W-D)}\cosh^{-1}\tfrac{1+W-D}{W}, \tag{4.1}$$

$$U_0 = \sqrt{\frac{32Etw^3g_0^2}{\pi\varepsilon_0 L^4}}, \tag{4.2}$$

where $D = 1 - g/g_0$ and $W = w/g_0$ are the relative displacement and relative width of the support structure. Fig. 4.1 illustrates the expected tuning and switching behavior (stable and instable solutions $D(U)$ for $W = 1$). For a small applied voltage, the elastic beams will bend towards each other until the elastic restoring force of the bridge beams is strong enough to balance the electrostatic attraction, leading to a regime of continuous tuning of the gap size. However, as the electrostatic force tends towards infinity as the gap size approaches zero, there is a threshold voltage, where the elastic restoring force cannot balance the electrostatic force anymore. At this voltage, the gap between the bridge beams will collapse, leading to a switching transition. In general (for any W),

Applied Voltage, V	Switching Time, ns
2	No switching, oscillation at 1MHz
2.24	1300
2.47	500
5	200

Table 4.1: **Switching time with for several voltages applied to two beams with initial separation of 125nm.**

switching occurs approximately at $D_{th} \sim 0.5$ and a threshold voltage of $U_{th} \sim U_0$.

For example, a bilayered structure consisting of gold on silicon nitride layers of equal thickness can be described by an average Young's modulus of about $E = 169$ GPa ($E_{SiNx} = 260$ GPa and $E_{Au} = 77$ GPa [125]). Having the structure discussed in section 4.3 in mind, we may consider an initial gap size $g_0 = 125$ nm, bridge thickness $t = 100$ nm, length $L = 35$ μm and typical width of $w = 375$ nm. Using this, a typical switching voltage of about $U_0 \sim$3V according to equation (4.2) should be expected.

Switching Dynamics

The numerical analysis of switching dynamics of an electrostatic NEMS actuator is presented in this section. Here, we consider two parallel beams in response to an applied voltage, and the total force F_{total} in the system , which is the combination of the electrostatic force $F_e = Q^2/(2\pi\varepsilon_0 L(g+w))$ and the restoring force $F_r = k(g_0 - g)/2$ described in last section. We use the example given in the last section: two beams consisting of gold and silicon nitride layers of equal thickness with an initial gap size $g_0 = 125$ nm, bridge thickness $t = 100$ nm, length $L = 35$ μm and typical width of $w = 375$ nm.

For two identical beams in response to an applied voltage, the numerical solutions of beam potential energy W as function of gap size g can be derived by solving $dW = -F_{total}dg$. The gap size as function of time can be derived by solving the equation of motion from $F_{total} = ma$, where m is the bridge mass and a is acceleration, see Fig. 4.2.

While we solve these equations numerically, we take few factor into account which are the linear elastic restoring force based on beam theory, the electrostatic force between two parallel wires, and the capacitance of two parallel wires (which affects the charge Q and therefore also the force). For simplifications, curvature of beams is ignored in calculation of electrostatic force/capacitance, each beam's gold layer is assumed to be continuous, and all beams are assumed to have the same width of 375 nm. The resulting

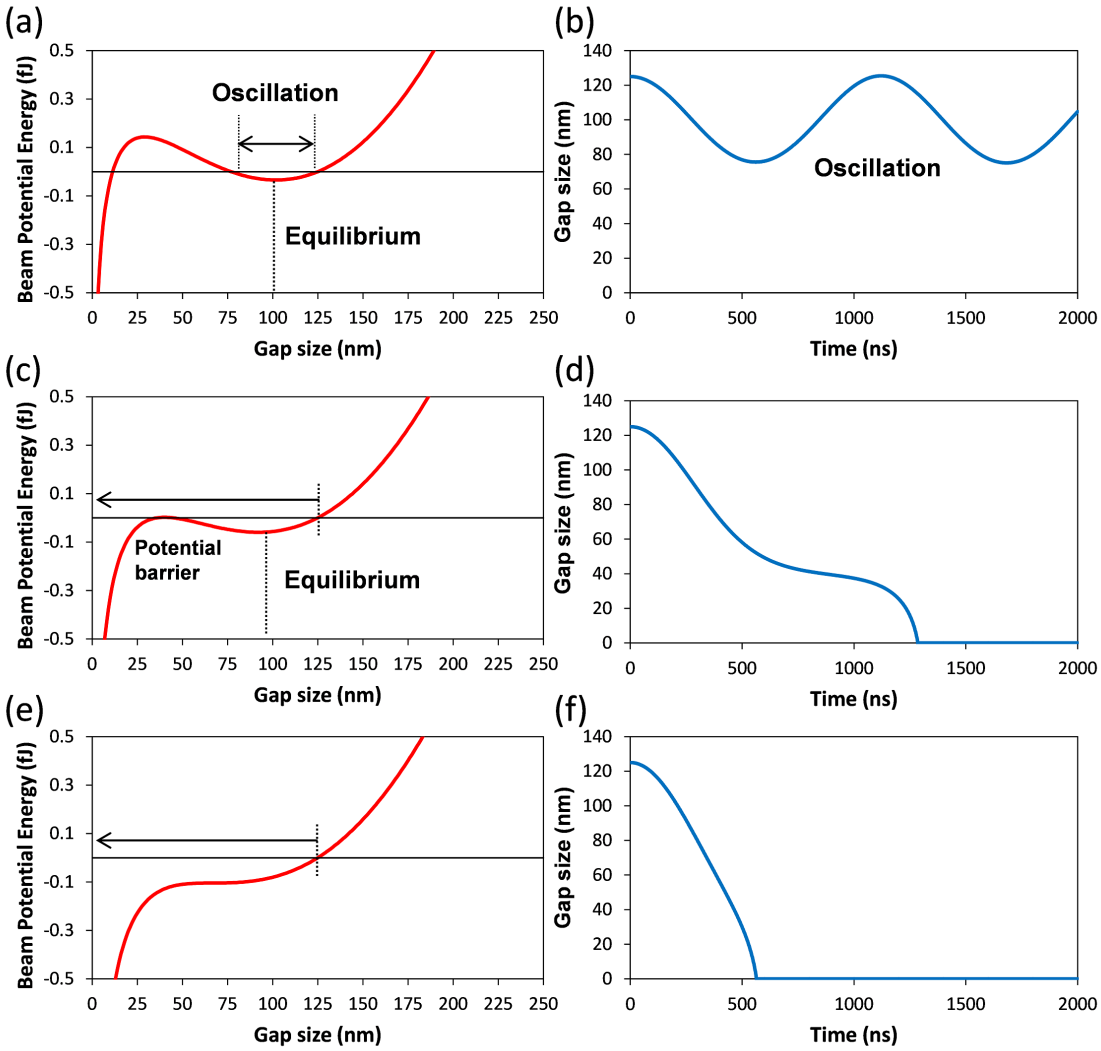

Figure 4.2: **Dynamics of electrostatically driven beams.** (a), (c), and (e) show the numerical solutions of beam potential energy as function of gap size in response to applied voltages of 2V, 2.24V, and 2.47V. (b), (d), and (f) illustrate the gap size as function of time for instantaneous application of voltages of 2V, 2.24V, and 2.47V at time $t = 0$.

switching time for several voltages applied to the pair of beams with initial gap size of 125 nm is presented in Table 4.1. There are three characteristic cases when voltage is applied to two elastic beams. Firstly, when the applied voltage is less than 2.2 V, the applied potential energy of the beams is not enough to overcome the potential barrier resulting from the restoring force and the the beams oscillate around an equilibrium separation, see Fig. 4.2 (a) and (b). In the case of $2V$ applied voltage, the beams oscillate around a separation of 107nm, and the oscillation frequency is about 1MHz, see Table 4.1. The second case is that the beam potential energy for a gap of 125nm (initial separation) is the same as the potential barrier, therefore the beams slow down as they overcome the potential barrier. Fig. 4.2 (c) and (d) illustrate a situation that is close to this case with an applied voltage of 2.24 V and the a switching time of two beams as slow as 1300 ns. In principle, switching could become arbitrarily slow for a precisely adjusted applied voltage. Finally, for voltage above 2.47 V, there is no potential barrier during the switching process. As a result, the switching time is only a few 100s of ns depending on the applied voltage, see Table 4.1 and Fig. 4.2 (e) and (f).

In summary, the switching time depends on the applied voltage magnitude and it will also depend on the speed of voltage application. Instantaneous application of the static switching voltage ($2.47V$) will lead to switching in about 500 ns, and the instantaneous switching voltage (2.24 V) is about 10% lower than the static switching voltage ($2.47V$). Also we can estimate the energy required to charge a bridge pair to the switching point as about 6 fJ. Therefore, the device of section 4.3, which consists of 12 bridge pairs, can be switched with $<$100 fJ.

4.2.2 Concept, Simulations and First Attempt Device

Here we demonstrate that electrostatically controlled reconfigurable photonic metamaterials provide a flexible platform for tuning and switching of metamaterial properties at optical frequencies. We illustrate this concept with a high-contrast metamaterial electro-optic switch operating in the telecommunications band from 1.3-1.7 μm.

The properties of almost any metamaterial system strongly depend on coupling between metamaterial resonators. Therefore tuning and switching of metamaterial properties will be achieved if the distance between the metamaterial resonators can be controlled. This may be achieved by placing the meta-molecules on reconfigurable support structures. Compared to existing MEMS metamaterials for the far-infrared, this approach has two key advantages: (i) Being independent of the specific meta-molecule

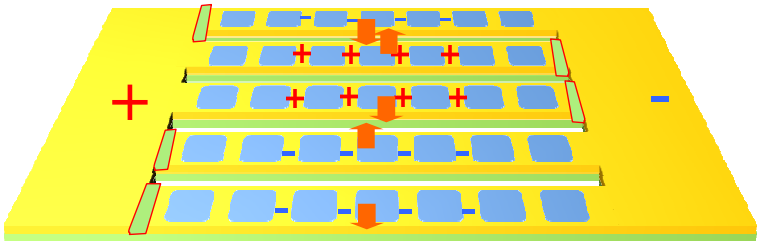

Figure 4.3: **The concept of electrostatically controlled RPMs.** The spacing of the supporting structure is controlled via attractive and repulsive electrostatic forces resulting from an applied voltage. When electrical potrntials applied to neighboring supporting beams are + and -, the neighboring supporting beams are attracted to each other. On the other hand, when electrical potentials applied to neighboring supporting beams are - - or ++, the neighbors repel each other.

design it is applicable to a huge range of metamaterial patterns. (ii) There is no need for reconfigurable elements on the size scale of the meta-molecules, which would be extremely challenging to achieve for optical frequencies.

Reconfigurable support structures may be realized in the form of support beams with controllable spacing. Here we will focus on electrostatic control, where the beam spacing is controlled via attractive and repulsive electrostatic forces resulting from an applied voltage as shown by Fig. 4.3.

Simulation results for an electrically controlled reconfigurable photonic metamaterial are shown by Fig. 4.4. It consists of silicon nitride bridges of 50 nm thickness alternatingly covered with nanoscale "meander"-shaped plasmonic resonators and continuous gold wires of 50 nm thickness. In the model, the bridges were initially separated by 125 nm (separation of gold edges). The transmission and reflection optical spectra were simulated by COMSOL with incident light polarized parallel to the bridges (x-polarization), shown in Fig. 4.4(a) and (b). The simulation results show that when the distance between "meander"-shaped plasmonic resonators and continuous gold wires decreases from 125 nm to 35 nm, the interaction between "meander"-shaped plasmonic resonators and continuous gold wires becomes stronger as shown in Fig. 4.4(c) and a dramatic red shift of the spectrum can be observed, see Fig. 4.4(a) and (b). The inset of Fig. 4.4(a) shows characteristic modes of excitation, where the charge distribution is labeled as "+" and "−". The incident light polarized in x-direction can easily excite the electric quadrupole resonance of the "meander" resonator, which corresponds to the transmission minimum and reflection maximum around 1300 nm. In principle, the "wire" resonators can sup-

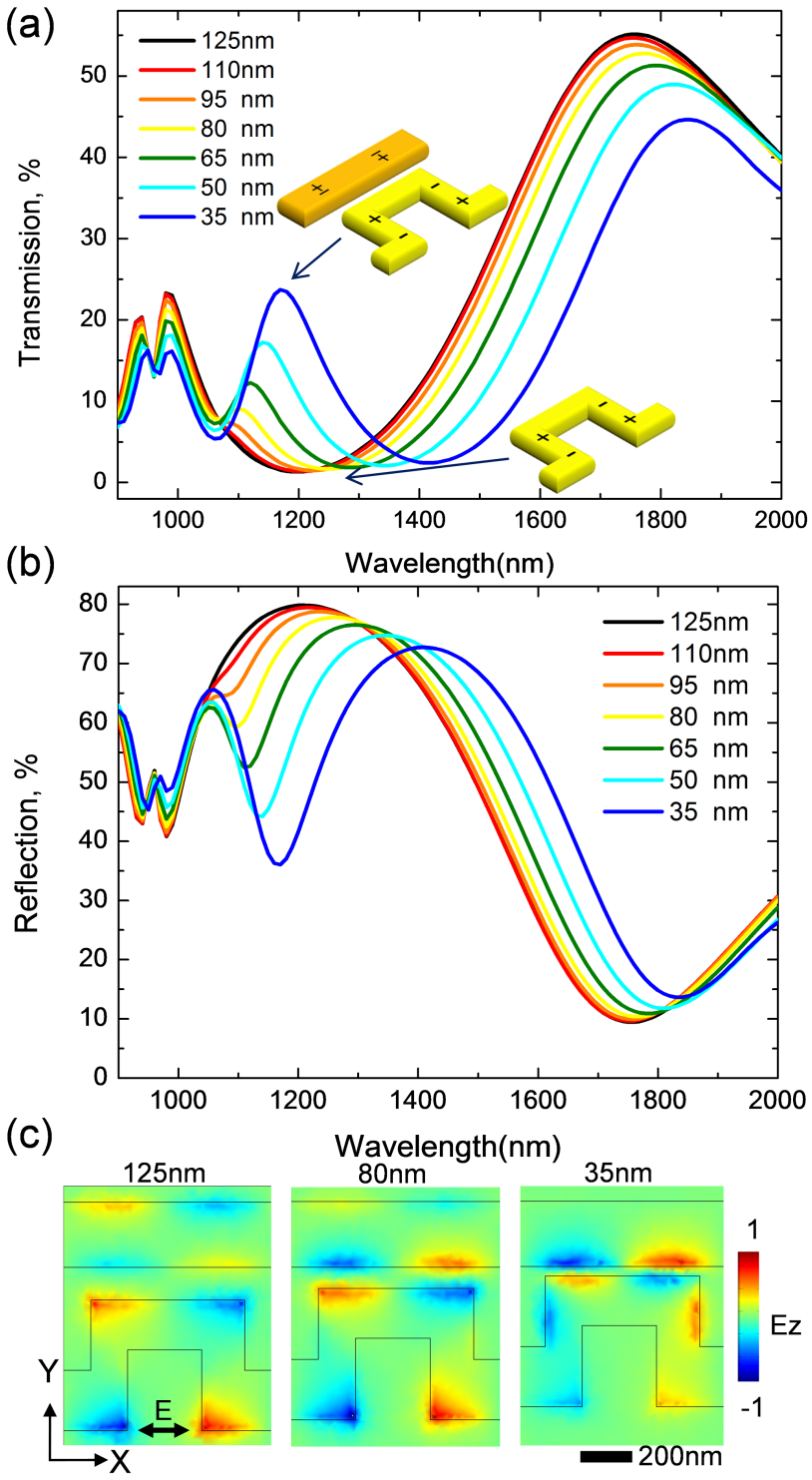

Figure 4.4: **Simulation results for an electrostatically controlled RPM.** (a) Transmission and (b) reflection optical spectra indicate a dramatic red shift with decreasing distance between "meander"-shaped plasmonic resonators and continuous gold wires. (c) The z-component of the electric field distribution at wavelength of 1170nm shows that the interaction increases as the distance between "meander"-shaped plasmonic resonators and continuous gold wires decreases. Gap sizes of 125 nm, 80 nm and 35 nm are shown.

port charge oscillations in the y-direction, however, these cannot be excited directly by x-polarized light and thus the excitation of this dark mode (forbidden mode) depends on coupling to the "meander" resonators. When both resonators move towards each other with x-polarized light illumination, the dark mode of the "wire" is excited by the electric quadrupole mode of "meander" resonator and hybridizes into a coupled mode, which is shown by Fig. 4.4 (c) and corresponds to the transmission peak and reflection minimum that emerge around 1170 nm wavelength for small gap sizes. As the coupling becomes stronger with decreasing gap size, the coupled resonance becomes more pronounced and shifts to lower energy. A similar red shift is also seen for the quadrupole resonance (reflection maximum around 1300 nm) and associated spectral features. In general, as the gap size decreases, increasing bridge coupling results in increasing displacement sensitivity of the nanostructure's optical properties. This effect will be confirm experimentally in section 4.3.2.

A first attempt device of electrically controlled reconfigurable photonic metamaterial was manufactured and is shown by Fig. 4.5. It consists of 35 μm long silicon nitride bridges alternatingly covered with nanoscale "meander"-shaped plasmonic resonators and continuous gold wires. The entire structure was fabricated by focused ion beam milling from a 50 nm thick silicon nitride membrane covered by a 50 nm thick thermally evaporated gold layer. The bridges were separated by 125 nm gaps for electrical isolation and pairs of bridges were alternatingly connected to two electrical contacts for electrostatic control of the device.

A voltage applied to the metamaterial device leads to alternating attractive and repulsive electrostatic forces between "meander" and "wire"-bridges. At small voltages the electrostatic forces are in equilibrium with the restoring force of the elastic bridges, leading to only small displacements. However, as the restoring force is proportional to the bridge displacement, while the electrostatic forces are inversely proportional to the bridge separation, there is the threshold voltage where the electrostatic force overcomes the restoring force, see section 4.2.1. At the threshold voltage U_{th} =5.7 V the structure switches into a brige-pair configuration, compare Figs. 4.6 (a) and (b), showing the "off" and "on"-states respectively.

Switching of the metamaterial state leads to dramatic changes of its optical properties. Fig. 4.7 (b) shows the metamaterial's reflection characteristics relative to the "off"-state. Switching the metamaterial to its "on"-state by applying a voltage above

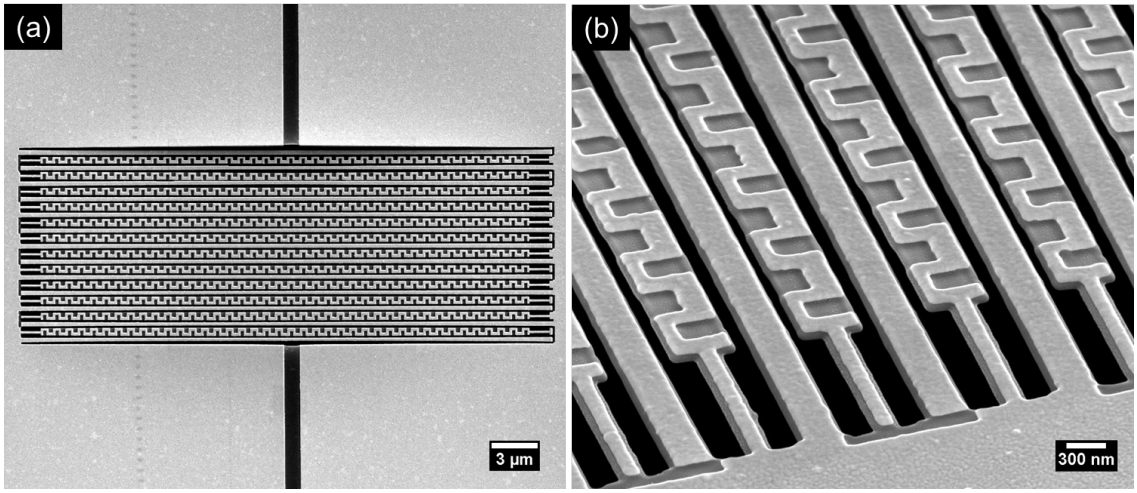

Figure 4.5: **SEM images of a first attempt device of electrically controlled reconfigurable photonic metamaterial.**

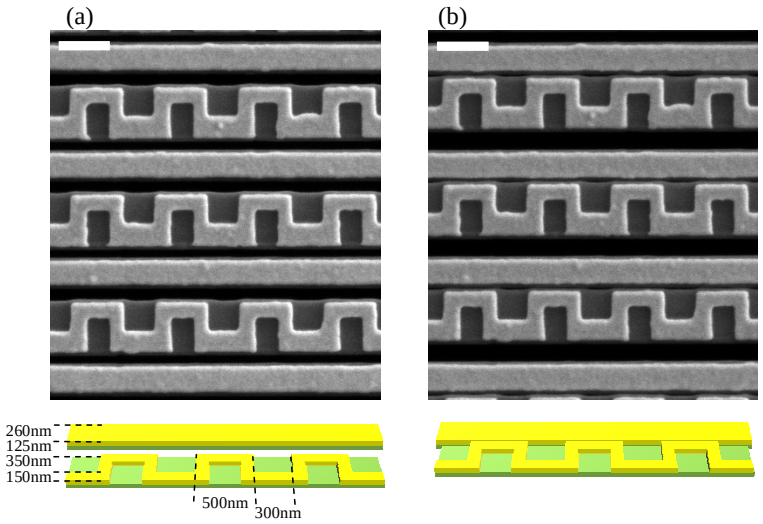

Figure 4.6: **Metamaterial electro-optic switch.** (a) "Off" state and dimensions. (b) "On" state. The scale bar is 500 nm long.

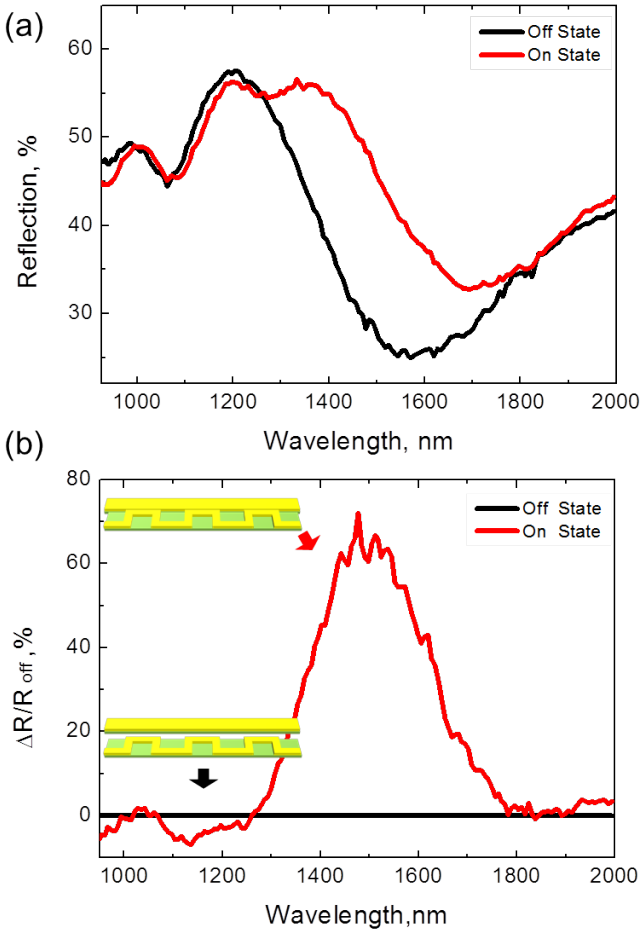

Figure 4.7: **Optical characteristics of electrostatically reconfigurable metamaterial switching between "on" and "off" states.** (a) Reflection spectrum of "on" and "off" states of the metamaterial electro-optic switch. (b) Contrast between "on" and "off" states of the metamaterial electro-optic switch: $(R - R_{\text{off}})/R_{\text{off}}$.

U_{th} increases its reflectivity by 72% in the telecommunications band around 1.5 μm. This remarkably large change in reflectivity is linked to a resonant mode of the coupled system of meander structure and straight wires. The resonant properties of this system strongly depend on coupling between neighboring bridges and switching the metamaterial to its "on"-state red-shifts the resonance by about 15% as the plasmonic structures are moved together by electrostatic forces.

Specifically, in this section a metamaterial electro-optic switch providing large contrast (up to 72%) between its reflective "off" an "on"-states in the telecommunications band around 1.5 μm has been demonstrated. However, the bridges ends are too stiff to move freely, as a consequence, the threshold voltage is high and the modulation depth is low in this structure. In order to address these issues, the bridge ends have been modified to increase flexibility, see section 4.3.

4.3 Electrostatically Controlled Reconfigurable Photonic Metamaterials

4.3.1 Concept and Device Fabrication

The new electro-optical photonic metamaterial, which is presented in Fig. 4.8, is a continuous plasmonic metallic "meander near the wire" pattern manufactured on a grid of flexible dielectric strings with picogram mass and megahertz mechanical resonances. On application of a few volts to neighboring strings ("wire" and "meander" conducting patterns) an attractive electrostatic force of a few nanonewtons moves the strings in the metamaterial plane, thus closing the gap between them. This strongly affects the "meander" pattern's resonant optical response, which is linked to the excitation of a plasmonic mode [131–133], allowing reversible transmission and reflection modulation with megahertz bandwidth as well as non-volatile switching of the metamaterial.

The nanostructure was manufactured by focussed ion beam milling on a 50 nm thick silicon nitride membrane that provides a stable and flexible base for the plasmonic pattern consisting of alternating 50 nm thick gold straight and meander wires. These were placed on 500 nm and 250 nm wide strings cut from the membrane and separated by 125 nm gaps to provide room for mutual motion. Pairs of strings were alternatingly connected to two electrical terminals on opposite sides of the device. To increase flexibility, string ends were narrowed to about 200 nm as shown by the SEM image (Fig. 4.8a). The entire nanostructure is $12\mu\text{m} \times 35\mu\text{m}$ in size.

Reconfigurable photonic metamaterial fabrication: Starting with a commercially available 50 nm thick low stress silicon nitride membrane, a 50 nm thick gold layer for the plasmonic metamaterial and the contact electrodes was thermally evaporated through a shadow mask. The gold-coated membrane was structured with a focussed ion beam system (FEI Helios 600 NanoLab), where the contact electrodes were connected to a source measurement unit (Keithley 2636) through a vacuum feedthrough for in-situ electrical characterization. Using focussed ion beam milling, first the "meander near the wire" pattern was milled, then the membrane was cut into suspended silicon nitride strings with tapered ends and finally the electrical terminals at the string ends were electrically separated by removing the gold film in selected areas. A more detailed description of the fabrication process is presented in section 2.3.2.

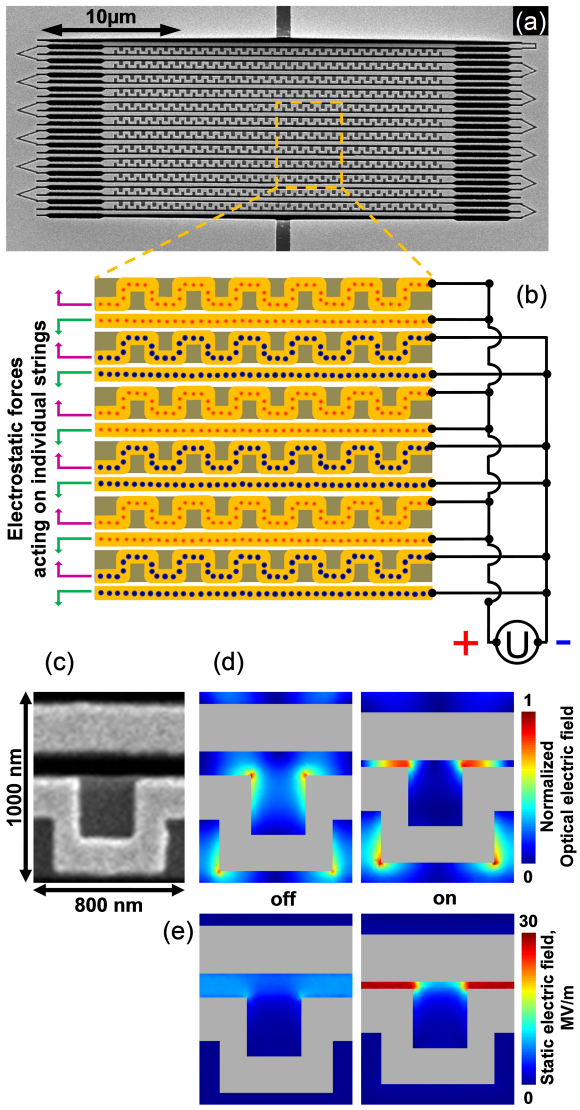

Figure 4.8: **Electrically reconfigurable photonic metamaterial**: (a) Scanning electron microscope image of the device; (b) Schematic of a section of the metamaterial pattern and driving circuit; (c) Detail of a single meta-molecule; (d) Plasmonic field distribution for the device's "off" and "on" states (excitation wavelength 1.6 μm and polarization E); (e) Static electric field for 1 V applied voltage.

4.3.2 Device Characterization

Experimental characterization: All imaging of the nanostructure was conducted in the focussed ion beam system, see Figs. 4.8 and 4.11. For the video recording of the switching process[1], the source measurement unit was used to induce switching.

The reconfigurable metamaterial's transmission and reflection spectra were recorded

[1] http://www.nature.com/nnano/journal/v8/n4/extref/nnano.2013.25-s1.mov

using a microspectrophotometer (CRAIC Technologies) while applying various DC voltages via the source measurement unit to tune the nanostructure's mechanical configuration, see Figs. 4.9 and 4.11.

High frequency electro-optical modulation was studied by measuring the modulation of a 1.3 μm laser beam transmitted through the nanostructure, while modulating the metamaterial using a signal generator (Tabor 8551, rectangular modulation between 0 V and 1.1 V). The modulated signal was detected by an InGaAs photodetector (New Focus 1811) and a lock-in amplifier (Stanford Research SR844), see Fig. 4.10. In all optical experiments the incident electric field was polarized parallel to the strings.

When a voltage is applied across the device terminals, the strings are exposed to electrostatic forces resulting from strong fields in the gaps between them ($\sim$8 MV/m at 1 V of applied control signal), see Fig. 4.8e. In response pairs of strings bend towards each other. While the restoring force grows linearly with string displacement, the electrostatic attraction grows infinite as the gap approaches zero: at a critical voltage the electrostatic attraction irreversibly overcomes the restoring force. For driving voltages below this threshold, reversible modulation of metamaterial pattern and optical properties is possible.

Exceeding the critical voltage results in step-like non-volatile switching and an abrupt change of the structure's optical properties. The critical voltage can be estimated from the balance of electrostatic attraction between two strings and their elastic restoring force as about

$$U_0 = \sqrt{\frac{32Etw^3g_0^2}{\pi\varepsilon_0 L^4}} \approx 3V$$

, as discussed in section 4.2.1. Here the average Young's modulus of silicon nitride and gold is $E = 169$ GPa and the initial gap size $g_0 = 125$ nm. The string dimensions are thickness $t = 100$ nm, length $L = 35$ μm and average width $w = 375$ nm. Below we will present both regimes of operation separately.

In the device reported here the critical voltage was measured to be about 3 V and continuous electro-optic modulation is possible at lower driving signals. Fig. 4.9 shows the spectral dependence of the induced reversible changes of the metamaterial's transmission and reflection relative to a reference case where no voltage is applied. Here the transmittance may be modulated by about 5% around wavelengths of 1.1 μm and 1.3 μm and reflectance can be modulated up to 8% around 1.5 μm. Below the threshold voltage, the bridge spacing will be larger than half of the initial gap size (compare Fig. 4.1) and

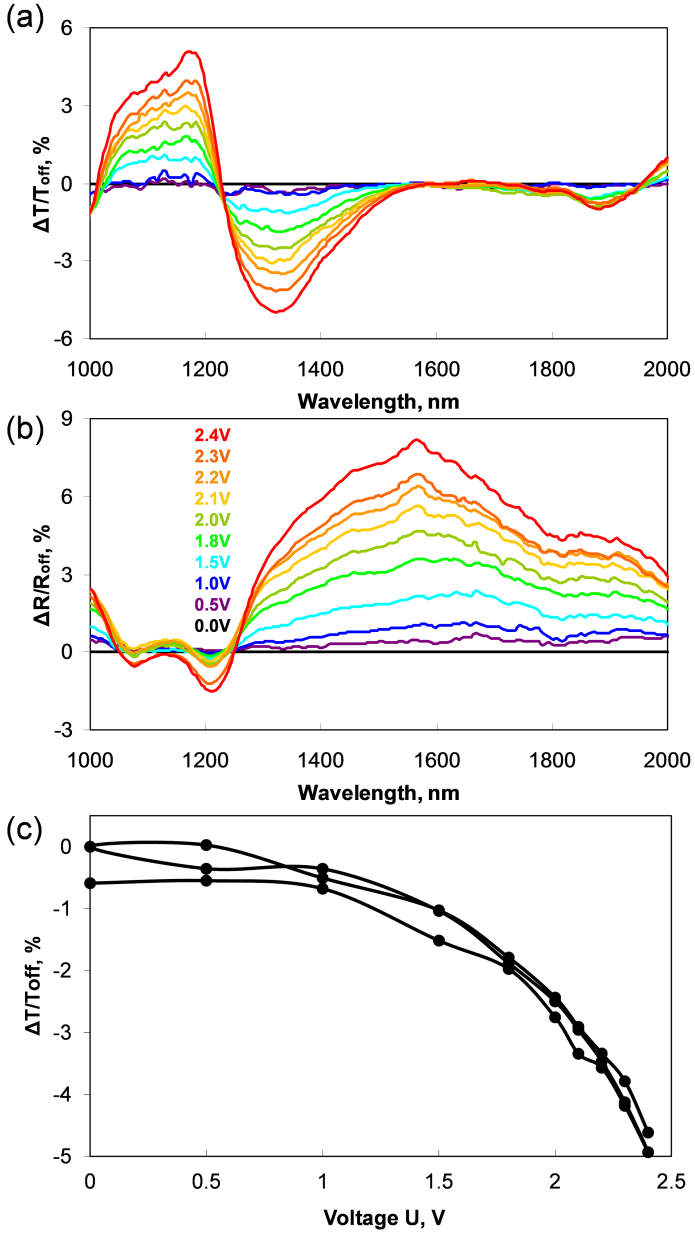

Figure 4.9: **Reversible electro-optical tuning and modulation**: Spectral dependence of (a) transmission and (b) reflection changes induced by applying a static voltage to the reconfigurable photonic metamaterial. (c) Repeatability of transmission changes at wavelength of 1330nm.

in case of the modulation experiments shown here the estimated gap size reduction is few 10s of nm. The observed transmission and reflection modulation is generally similar to that expected from simulations for such displacements (compare Fig. 4.4). It is noted that the magnitude of the observed relative transmission modulation is smaller than

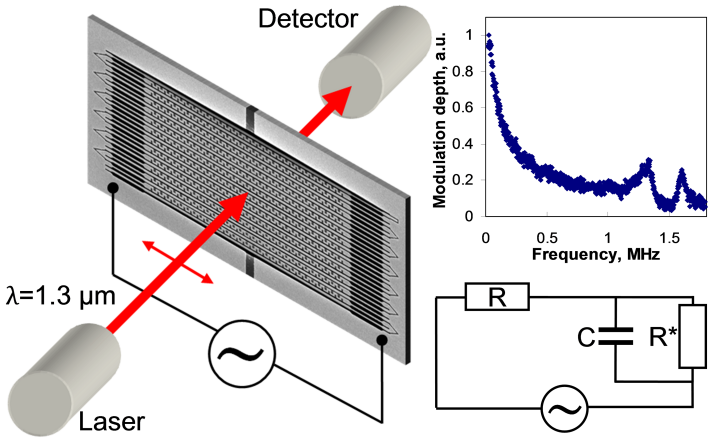

Figure 4.10: **MHz bandwidth electro-optical modulator**: Modulator schematic, frequency response function and equivalent electric circuit diagram.

predicted by simulations largely because of the very small reference transmission around 1200 nm wavelength of $< 2\%$ in simulations compared to about 6% in experiments (see Fig. 4.11 for experimental reference curves).

To understand the potential of electrostatically reconfigurable nanostructures for high-frequency modulation of metamaterial optical properties we have estimated the fundamental mechanical resonance frequency of the strings with rectangular cross-section based on classical beam theory as (see detail in section 5.2.2)

$$f = \frac{1}{2\pi}\sqrt{\frac{32E}{\rho}}\frac{w}{L^2} \approx 1 \text{ MHz}$$

where $\rho = 11.4$ g/cm^3 is the average density of gold and silicone nitride. This simplified formula does not take into account the incomplete gold coverage and narrowing of string ends.

Mechanical systems can be easily driven to frequencies up to their fundamental resonance, although in reality the frequency response is complicated by the resonant properties of the feeding electrical network. Indeed, when measuring the frequency dependence of optical modulation at the wavelength of 1.3 μm, we saw a complex spectral response with initial roll-off at about 0.5 MHz and then two resonance peaks at 1.3 MHz and 1.6 MHz, in a reasonable agreement with our estimates of the fundamental frequency f, see Fig. 4.10.

By increasing the applied voltage beyond the structure's threshold voltage we enter the regime of step-like switching. Here switching occurs at $U_c = 3$ V and the opti-

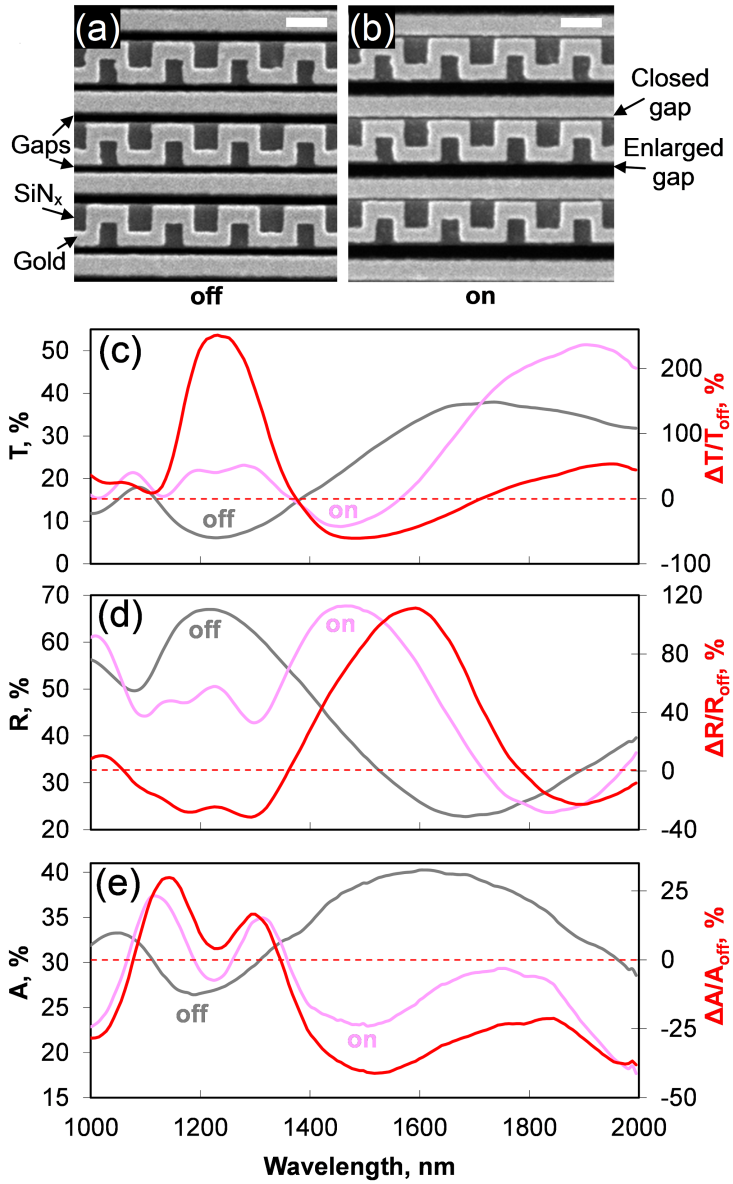

Figure 4.11: **High-contrast, non-volatile switch**: SEM images of the metamaterial in its (a) "off" and (b) "on" states. A white 500 nm scale bar is shown. (c) Transmission, (d) reflection and (e) absorption spectra of the device in the "off" and "on" states (left axis) and the corresponding switching contrast (right axis).

cal characteristics of the device's "on" and "off" states are presented in Fig. 4.11. In the telecommunications band, the metamaterial's transmission, reflection and absorption spectra red-shift by about 20% when the device switches, leading to dramatic 250% transmission changes around 1.2 μm and 110% reflectivity changes around 1.6 μm. Qualitatively similar switching behaviour is also predicted by numerical simulations, see Fig.

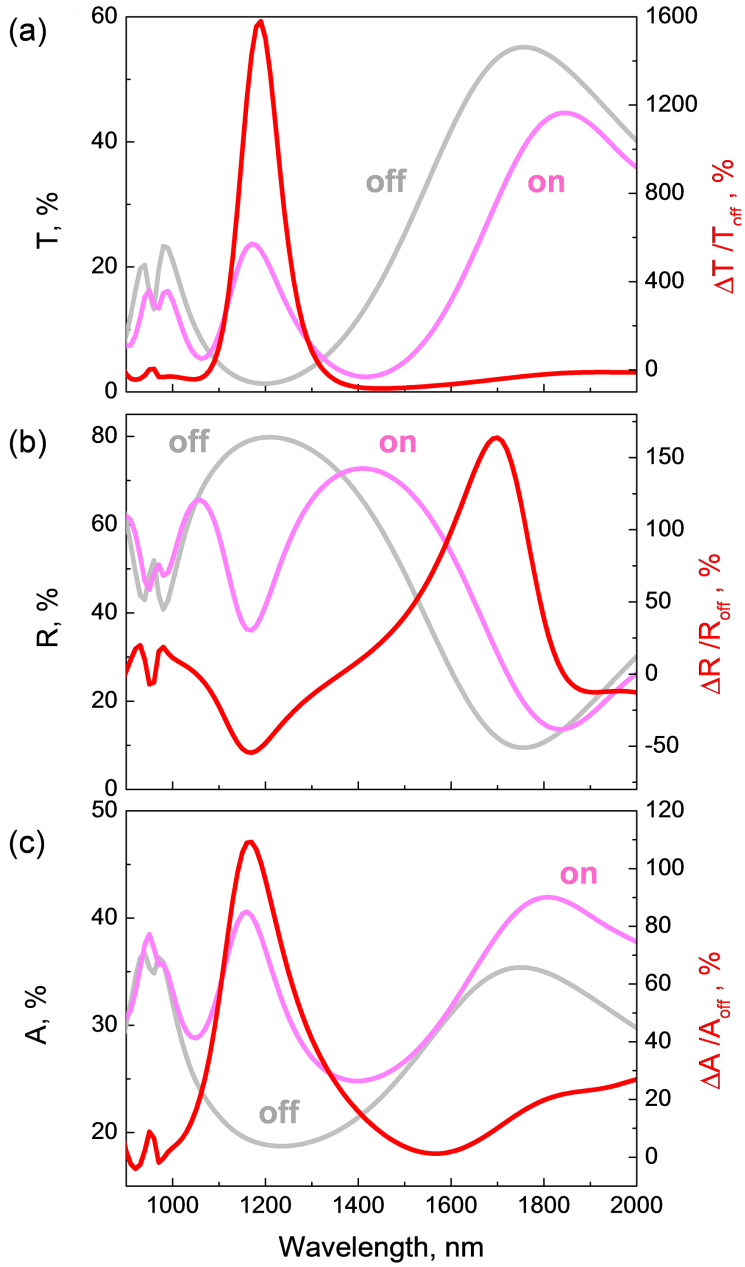

Figure 4.12: **Simulation of high-contrast switch**: (a) Transmission, (b) reflection and (c) absorption spectra of the device in the "off" and "on" states (left axis) and the corresponding switching contrast (right axis).

4.12. Simulated and experimental transmission and reflection spectra show the same qualitative behaviour. It is noted that simulations predict a much larger switching contrast $(T_{on}-T_{off})/T_{off}$ in transmission than experiments, as the minimum reference level T_{off} is almost zero in simulations. Overall, inhomogeneous broadening due to fabrication imperfections leads to smaller resonance quality factors in experiments compared to simulations.

Such switching is irreversible as on withdrawal of the driving voltage the metamaterial remains in its "on" configuration supported by the electrostatic force resulting from residual charges accumulated in the edge of dielectric surfaces after the driving field is withdrawn. (This "sticking" effect could be eliminated by resorting to modified designs, materials and chemical surface treatments [134].) The origin of the drastic switching-induced change of the metamaterial's optical properties can be understood from Fig. 4.8(d), which shows the optical electric field distribution before and after switching. For light polarized parallel to the wires, the metamaterial's resonances are mainly caused by the excitation of plasmonic standing waves along the meander pattern. In the "off" state, interaction with the straight wires is relatively weak and the electromagnetic field is mainly localized around the meander pattern. However, as straight and meander wires move closer together, their interaction becomes much stronger, the field redistributes into the narrow gap and the resonances shift to longer wavelengths. In such a highly nonlinear system the switching dynamics are complex and strongly depend on initial conditions and the shape of the control signal. However, by numerically solving the nonlinear equations of motion of a pair of strings, the characteristic switching time can be evaluated as about 500 ns for the metamaterial going from the initial "off" state to the fully switched "on" state, if a control signal equal to the static switching voltage U_c is applied abruptly, see section 4.2.1.

In order to evaluate the device's power consumption we approximated it with the equivalent circuit presented in Fig. 4.10. The leak resistance of $R^* = 400\ k\Omega$ dominates the power consumption in the low frequency limit: $P = U^2/R^*$ gives the power needed to drive the modulator at $U = 1$ V to be only about $\approx 2.5\ \mu W$. Simplifying the nanostructure as 12 parallel wire pairs, its capacitance can be estimated analytically as about $C_0 = 15$ fF, increasing to about 20 fF at the static switching voltage U_c due to the decreasing gap between the wires. The energy required to switch the device from "off" state to "on" state can be estimated as the energy required to charge the capacitive nanostructure to the static switching point and was determined numerically as about

100 fJ, a very small amount of energy.

It is interesting to compare the metamaterial's electro-optic properties to conventional electro-optic materials. Electro-optic modulation usually results from minute refractive index changes achieved by application of electric field across an electro-optic crystal, which is why applications require long crystals, high-voltage driving signals and polarizers to exploit birefringence-induced polarization effects, while a similar solution using liquid crystals yields a slow response. In conventional electro-optic media such as perovskite-type ferroelectric lithium niobate the electro-optic effect mainly comes from field-induced relative displacement of the central metal ion and the surrounding oxygen octahedron. This displacement changes the electronic band wave functions through electron-phonon coupling, which affects the lattice's refractive index [135]. Similarly, in the reconfigurable metamaterial an electro-optic effect arises from electric field-induced relative displacement of its constitutive parts. This displacement changes the structure's collective plasmonic wave function, which affects the lattice's effective refractive index. In light of these intriguing similarities of microscopic mechanism and macroscopic manifestation we estimate the reconfigurable metamaterial's effective electro-optic coefficient. Full three-dimensional Maxwell calculations show that "off" to "on" switching of the 100 nm thick structure changes the transmitted wave's phase by up to $\pi/5$ at around 1.6 μm, corresponding to an effective refractive index change $\Delta n = 1.6$. This results from applying U_c=3 V across L=35 μm of metamaterial. Thus the effective electro-optic coefficient of the metamaterial is about $\Delta nL/U_c \sim 10^{-5}$ m/V in the non-volatile regime, and about $\sim 10^{-6}$ m/V in a fully reversible regime, which is about 5-4 orders of magnitude greater than for typical electro-optic media such as lithium niobate ($3 \cdot 10^{-11}$ m/V [136]). This makes the metamaterial suitable for light modulation in small low-voltage devices without polarizers.

The novel technology presented here provides opportunities for further development, but it also has some limitations. Larger modulation depths can be achieved with metamaterial patterns that have narrower resonances [137]. Even faster modulation would result from smaller reconfigurable elements, where GHz modulation can be anticipated for electrostatic actuation within the individual meta-molecules. On the other hand, larger reconfigurable metamaterials based on longer strings will tend to be slower modulators, which can only be partially addressed by using stiffer materials. Also, bowing of the strings necessarily introduces some inhomogeneity, which can be reduced but not prevented by tapered string ends.

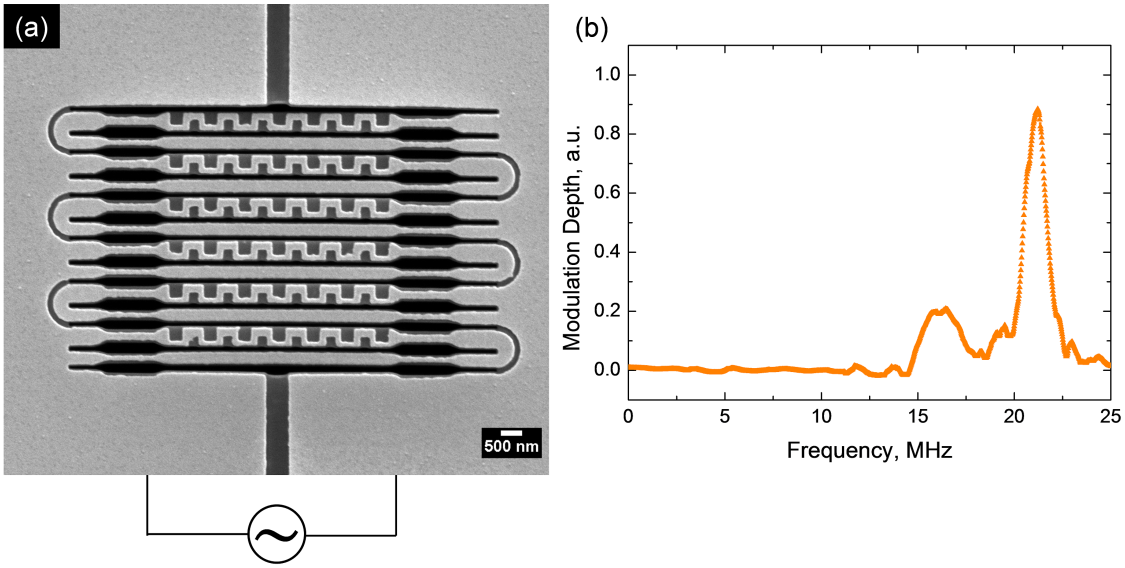

Figure 4.13: **High-frequency electrostatically reconfigurable metamaterial.** (a) Scanning electron micrograph (SEM) of the metamaterial. (b) Modulation depth as a function of modulation frequency.

4.3.3 20MHz Electro-Optic Modulation

We have demonstrated an electrostatically reconfigurable metamaterial providing high contrast switching and electro-optical modulation at modulation frequencies up to 1 MHz as presented in the previous section. Building on this work and aiming to develop the potential of reconfigurable metamaterials for fast electro-optic modulation and addressable modulators, we shrink the characteristic size of the electrostatically driven metamaterial from 35 μm to 9 μm, see Fig. 4.13(a). As the mechanical resonance frequency of the bridges is inversely proportional to the square of their length, this increases the achievable modulation speed. The metamaterial, which consists of alternating straight and meander bridges, was fabricated by focused ion beam milling starting from a 50 nm thick silicon nitride membrane coated with a 50 nm thick layer of gold. Pairs of bridges are alternatingly connected to the electrical terminals on either side, so that application of an electric potential leads to alternating attractive and repulsive forces which reconfigure the metamaterial. The electrical modulation of the metamaterial's optical properties can be detected up to its mechanical resonances around 20 MHz, see Fig. 4.13(b).

4.4 Conclusion

In summary, the novel class of reconfigurable nanostructures introduced here transfers electrically reconfigurable metamaterials from the terahertz to the optical part of the spectrum, while simultaneously increasing their modulation speed by 4 orders of magnitude. Such structures, with some modifications, are compatible with low-cost production using high-resolution CMOS fabrication techniques and nano-imprint. The approach based on engaging elastic properties of a nanoscale thickness dielectric membrane and nanoscale electrostatic forces in a planar plasmonic structure provides a powerful generic platform for achieving tunable metamaterial characteristics in the optical spectral range. Such reconfigurable metamaterials can be operated at microwatt power levels and can provide continuous modulation of optical signals with 10s of megahertz bandwidth. We expect that, in principle, reconfigurable elements on the size scale on the meta-molecules would allow GHz modulation rates. A compact design integrating the actuation mechanism into the metamaterial, low power consumption and direct control with a few volts make electrostatically reconfigurable photonic metamaterials compatible with optoelectronic systems, for example as tunable spectral filters, switches, modulators and adaptable transformation optics devices. The low energy, high-contrast, non-volatile switching mode of these devices may also have applications in protective optical circuitry and reconfigurable optical networks.

5

Optically Reconfigurable Photonic Metamaterials

5.1 Introduction

Optical forces resulting from electromagnetic field gradients, radiation pressure and interaction between resonators play a key role for optical tweezing, manipulation and binding [138–142] and they form the basis for the emerging areas of optomechanical cavities and crystals [143–149] and optical actuation of nanophotonic devices [150–157]. Recent works on optical forces between metamaterial resonators [45,158–160] and nearby interfaces [161] suggest that optical forces in metamaterials provide a novel opportunity for all-optical control of metamaterial properties. Here we demonstrate that metamaterials assembled from essentially linear components can be reconfigured by light itself, providing a novel route to highly nonlinear optical media. We report an optomechanical nonlinearity that is 7 orders of magnitude greater than nonlinear absorption in the nonlinear reference medium GaAs.

Metamaterials derive a huge range of novel or enhanced properties from artificial structuring on the sub-wavelength scale [162]. Reconfigurable metamaterials achieve tuning and modulation of these optical functionalities by rearranging the metamaterial building blocks, the meta-molecules. Reconfigurable photonic metamaterials, where components of thousands of meta-molecles must be synchronously moved over distances on the order of 10 nm, present a formidable technological challenge. However, working on the nanoscale also opens up important opportunities: (i) Elastic restoring forces become weak in structures of nanoscale thickenss, while optical forces become significant in the optical near-field, particularly across nanoscale gaps between plasmonic resonators. At the same time, nanoscale movements of meta-molecular components are sufficient

to induce a profound change in a metamaterial's optical properties. In this way, the nanoscale is the key to optomechanically reconfigurable metamaterials providing large optical nonlinearities at low intensities. (ii) Inertial and elastic forces scale differently with size, in a way that drives mechanical frequencies to large values, providing an opportunity for fast modulation of metamaterial properties, for example MHz electro-optical modulation has been reported recently [126].

5.2 Towards Optically Reconfigurable Photonic Metamaterials

5.2.1 Optical Forces in Photonic Metamaterials

Photonic metamaterials provide a unique platform for manipulating electromagnetic fields and thereby optical forces on the nanoscale. There has been quite a lot of interest in demonstrating negative radiation pressure in artificial media exhibiting a negative refractive index [21]. Besides there are also many other interesting phenomena and functionalities that could be achieved by harnessing optical forces via metamaterials. Their ability of trapping light through plasmonic resonances and generating strong variations of electromagnetic field, for example, can be utilized for efficient enhancement of optical forces [137]. The complex electromagnetic fields and nanoscale localization of light produced by metamaterials also show potential for optical manipulation [23, 163]. Moreover, optical forces combined with suitable mechanical designs can be harnessed to drive the reconfiguration of metamaterials, providing opportunities for all optically controlled active metamaterials and for optomechanical metamaterials displaying novel nonlinear effects via mutual interactions between light and mesoscopic structures [45, 164].

Within the framework of classical electrodynamics the components of the total time-averaged force $< F >$ acting on a metamaterial structure illuminated with light can be calculated using a surface integral [130]:

$$< F_i >= \oiint_s < T_{ij} > n_j dS \tag{5.1}$$

, where S is a bounding surface around the metamaterial element and $< T_{ij} >$ is the time-averaged Maxwell stress tensor:

$$< T_{ij} >= \frac{1}{2} Re \left[\varepsilon\varepsilon_0 \left(E_i E_j^* - \frac{1}{2}\delta_{ij} |E|^2 \right) + \mu\mu_0 \left(H_i H_j^* - \frac{1}{2}\delta_{ij} |H|^2 \right) \right] \tag{5.2}$$

The stress tensor integral equation 5.1 encompasses both the radiation pressure and the near-field gradient force. It does not include Casimir forces, which are derived from vacuum quantum fluctuation and thus exist even in the absence of illumination [165]. Radiation pressure arises through transfer of momentum between photons and any surface on which they impinge. It depends on the reflection R and absorption A coefficients of the surface. At normal incidence, the associated force on the surface follows $F_r = (2R + A)P/c$, where c is the speed of light in vacuum and P is the power of the incident light, and it assumes a maximum value of $2P/c$ when the reflectivity of the surface is 100%. In section 5.3, forces acting on metamaterial structures are evaluated via the Maxwell stress tensor integral equation 5.1 with electric E and magnetic H field distributions obtained from fully 3D finite element Maxwell solver simulations (COMSOL MultiPhysics).

5.2.2 Mechanical Resonance Frequency Analysis of NEMS Actuators

It is essential to understand the mechanical properties of NEMS actuators in order to develop a suitable platform for reconfigurable photonic metamaterials. The restoring force of an elastic NEMS actuating beam can be formulated as $F_r = -kx$, where x is the displacement and $k_n = 32Ewt^3/L^3$ and $k_l = 32Etw^3/L^3$ [129] are the spring constants for normal and lateral displacement of a bridge beam that is connected on both ends, with Young's modulus E and bridge thickness t, width w and length L. The fundamental normal and lateral resonance frequencies are given by

$$f_n = \frac{1}{2\pi} \frac{t}{L^2} \sqrt{\frac{32E}{\rho}} \tag{5.3}$$

$$f_l = \frac{1}{2\pi} \frac{w}{L^2} \sqrt{\frac{32E}{\rho}} \tag{5.4}$$

where ρ is the density of the mechanical beam. For instance, a bilayered structure consisting of equal volumes of gold on silicon nitride can be described by an average Young's modulus of about $E = 169$ GPa ($E_{\mathrm{SiNx}} = 260$ GPa and $E_{\mathrm{Au}} = 77$ GPa [125]) and an average density of 11200 kg/m^3(ρ_{SiNx} =3100 kg/m^3 and ρ_{Au} =19300 kg/m^3).

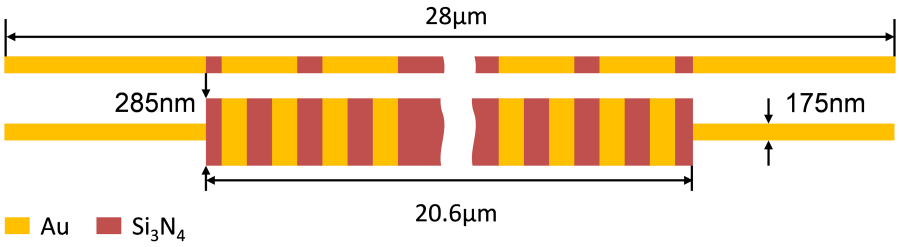

Figure 5.1: **Dimensions of the simulated NEMS actuators.** 29 pairs of Π-shaped gold (yellow) resonators are arranged on the central part of the silicon nitride (red) beams.

Material Property	Silicon Nitride	Gold
Density (ρ)	3100 kg/m^3	19300 kg/m^3
Young's modulus (E)	260 GPa	77 GPa
Poisson's Ratio	0.23	0.44

Table 5.1: **Material properties of simulated NEMS actuators.**

Having the structure discussed in section 5.3 in mind, we may consider bridge thickness $t = 100$ nm, length $L = 28$ μm and average width of $w = 175$ nm. Using this, normal and lateral fundamental resonance frequencies of about $f_n \sim 450\,\text{kHz}$ and $f_n \sim 1$ MHz according to equations 5.3 and 5.4 should be expected.

In reality, the exact mechanical resonance frequencies depend on details of the plasmonic resonator design and the bridge design, making an exact analytical description impractical. Therefore, we use COMSOL Multiphysics for finite element method numerical modeling of mechanical eigenfrequencies. The optically reconfigurable metamaterial consists of two different mechanical silicon nitride beams with Π-shaped gold resonators known for exhibiting plasmon-induced transparency [117,118,166], see Fig. 5.4(a). Both the silicon nitride layer of the beams and all gold structures have a thickness of 50 nm. The narrow beam consists of silicon nitride with dimensions of length 28 µm and width of 175 nm; it supports 29 gold resonators with dimensions of length 483 nm and width of 175 nm with 700 nm periodicity, see Fig. 5.4(a). The wide beam consists of a central part of silicon nitride with dimension of length 20.6 µm and width of 285 nm connected to two narrow beams with dimensions of length 3.7 µm and width of 175 nm; it supports 29 pairs of gold resonators with dimensions of length 140 nm and width 285 nm located on center silicon nitride beam with 700 nm periodicity, and continuous gold coverage 50 nm on top of the narrower beam ends, see Fig. 5.1.

The eigenfrequency analysis was carried out using the material properties in Table

Modes	Frequency	Mode description
Mode 1	716 kHz	Narrow beam, out of plane
Mode 2	764 kHz	Wide beam, out of plane
Mode 3	1.22 MHz	Narrow beam, in plane
Mode 4	1.58 MHz	Wide beam, in plane
Mode 5	1.89 MHz	Narrow beam, 2^{nd} order out of plane
Mode 6	2.00 MHz	Wide beam, 2^{nd} order out of plane

Table 5.2: **Eigenfrequency analysis of a pair of mechanical beams.**

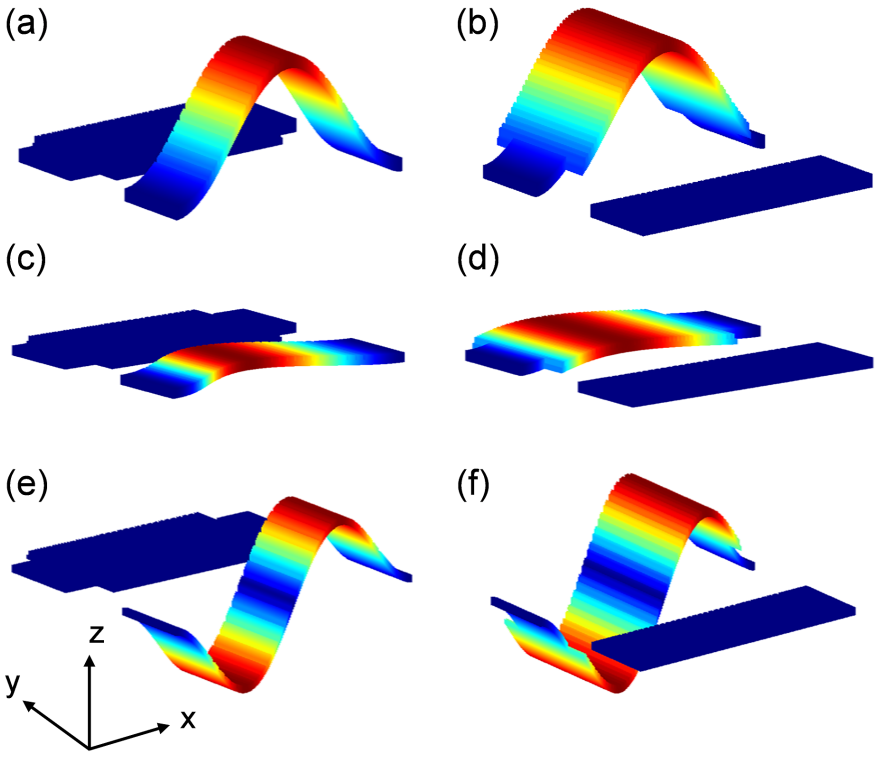

Figure 5.2: **Illustration of mechanical resonant modes of a pair of NEMS actuators at different eigenfrequencies.** (a) 716 kHz (b) 764 kHz (c) 1.22 MHz (d) 1.58 MHz (e) 1.89 MHz (f) 2.00 MHz

5.1 and it revealed 6 mechanical resonances at frequencies up to 2 MHz. The lowest frequency for which these stationary waves are formed is called fundamental harmonic. The modes of oscillation have different shapes for different frequencies, see Table 5.2 and Fig. 5.2. Based on this mechanical mode analysis, there are two main categories of the mechanical modes in simulated NEMS actuating beams which correspond to out of plane and in-plane motions. The out of plane oscillation would be easy to excite by force action normal to the metamaterial plane (z-axis), on the other hand, the in-plane motion would be triggered by force action in the plane (y-axis).

5.2.3 Thermal Time Scale Analysis of NEMS Actuators

Optically reconfigurable metamaterial is driven by strong laser radiation which results in optical heating in addition to the optical forces discussed in section 5.2.1. Therefore, it is essential to understand the thermal dynamics and time scale of the nanostructure to distinguish effects driven by electromagnetic forces and optical heating. Cooling of the nanostructure is mainly controlled by conductive heat transport.

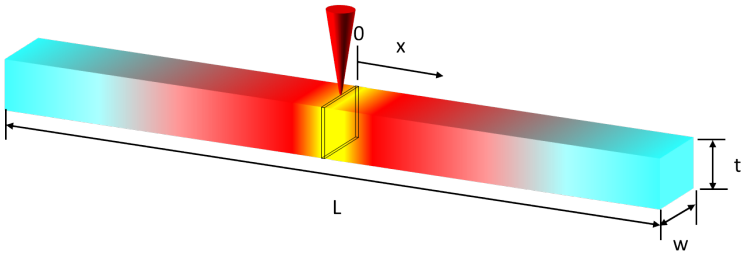

Figure 5.3: **Dimensions of the NEMS actuator heated by a laser beam.**

From Fourier's Law [167], we can determinate the heat flux from knowing the temperature (T) distribution in a medium:

$$\frac{\text{energy flow}}{\text{crossection}} = -k_t \frac{dT}{dx} \tag{5.5}$$

where k_t is the thermal conductivity and the direction of heat flow is pointing to both cold ends of the bridge. We consider a silicon nitride/gold bridge with dimension of length L, thickness t and width w which is covered by gold meta-molecules of unit cell width u and absorption A. A laser beam of intensity I illuminates the entire bridge and heat flows from the bridge centre at $x = 0$ towards both cold ends. From equation 5.5,

we have:

$$\frac{1}{2}\frac{IAuL}{wt}\frac{x}{L/2} = -k_t\frac{dT}{dx} \tag{5.6}$$

Integrating from the centre of the bridge to its end we get:

$$\int_0^x -\frac{IAu}{wtk_t}xdx = \int_{T_0}^{T} dT \tag{5.7}$$

and:

$$-\frac{IAu}{w}\int_0^x \frac{1}{t(x)k_t(x)}xdx = T(x) - T_0 \tag{5.8}$$

Taking the partial gold coverage of the silicon nitride bridges into account, the quantiy $1/(tk_t)$ is averaged over the unit cell, $< \frac{1}{tk_t} >= \frac{P_{Au}}{tk_{Au}} + \frac{1-P_{Au}}{t_{SiNx}k_{SiNx}}$, whereP_{Au} is the fraction covered by gold, t is the combined thickness of the gold and silicon nitride layers and k_t is the average of the thermal conductivities weighted by the layer thicknesses . Using the constant $< \frac{1}{tk_t} >$we can easily solve the integral of equation 5.8:

$$T(x) = T_0 - \frac{IAu}{w} < \frac{1}{tk_t} > \frac{1}{2}x^2$$

$$T_0 = T_{bridge\,end} + \frac{IAu}{w} < \frac{1}{tk_t} > \frac{L^2}{8}$$

where $\Delta T_{max} = \frac{IAu}{w} < \frac{1}{tk_t} > \frac{L^2}{8}$ is the temperature difference between the center of the bridge and its ends..

Now, we consider the thermal energy stored in the bridge which is the integration of the temperature distribution $T(x)$ multiplied by the heat capacity per unit length C_{length} along the bridge, where $< C_{length} >= \frac{V_{Au}C_{Au,vol}+V_{SiNx}C_{SiNx,vol}}{w}$,V_{Au}, V_{SiNx} are volume of gold and silicon nitride, and $C_{Au,vol}$,$C_{SiNx,vol}$ are volume heat capacities of gold and silicon nitride. The thermal energy corresponding to the temperature increase relative to the bridge ends is:

$$\int_{-L/2}^{L/2}[T(x) - T_{bridg\,end}]C_{length}dx =< C_{length} > \frac{IAu}{w} < \frac{1}{Tk_t} > 2\int_0^{L/2}\frac{L^2}{8} - \frac{x^2}{2}dx \tag{5.9}$$

We get the stored thermal energy by integrating equation 5.9:

$$\frac{IAu}{w} < \frac{1}{tk_t} > \frac{L^2}{8}\frac{2}{3}L < C_{length} >$$

Materials	Thermal Conductivity	Heat Capacity	Volume Heat Capacity
Units	W/K m	J/K kg	J/K m^3
Gold	146	129	2489700
SiNx	2	650	1742000

Table 5.3: **Thermal properties of gold and silicon nitride [127, 128].**

and using $\Delta T_{max} = \frac{IAu}{w} < \frac{1}{tk_t} > \frac{L^2}{8}$, the store energy can be written as

$$Stored\,Energy = \frac{2}{3} L \Delta T_{max} < C_{length} > \tag{5.10}$$

The conductive cooling timescale can be estimated as Timescale=Energy stored/Rate of energy in $(IAuL)$:

$$TimeScale = \frac{L^2 < C_{length} >}{12w} < \frac{1}{tk_t} > \tag{5.11}$$

Having the structure discussed in section 5.3 in mind, we may consider bridge thickness $t = 100$ nm, length $L = 20.6$ μm (length covered with meta-molecules, see Fig. 5.1), average total width of $w = 460$ nm (combining both bridges), metamaterial absorption $A = 30\%$, pump laser peak intensity I =250 W/cm^2 and thermal material parameters in table 5.3 with gold coverage of 51%. Using equation 5.11, we can evaluate that the conductive cooling timescale is about 20-30 μs.

5.3 Optically Reconfigurable Photonic Metamaterials

5.3.1 Concept and Structure Fabrication

The optomechanical photonic metamaterials studied here are based on a Π-shaped resonator design known for exhibiting plasmon-induced transparency [117, 118, 166], see Fig. 5.4a,b. In order to allow mechanical deformation of the plasmonic Π meta-molecules, the horizontal and vertical bars have been supported by different flexible dielectric bridges. The nanostructures were fabricated by FIB milling from a 50 nm thick silicon nitride membrane covered with a 50 nm thick thermally evaporated layer of gold. The unit cell is 700 nm × 700 nm in size and the supporting silicon nitride bridges are 28 μm long; the fabrication steps are described in detail in chapter 2. Our experimental samples are characterized by the spacing of the bridges, which is similar for the more "symmetric" sample (110 nm and 130 nm) and dissimilar for the "asymmetric" sample

(95 nm and 145 nm), respectively. Detailed dimensions of the unit cells are given in Fig. 5.4(a) and Fig. 5.5(a). For an ideally symmetric structure, in-plane forces between any bridge and its neighbors would have to cancel, while optical forces F_{y1} and F_{y2} should be expected to displace bridges within the metamaterial plane in the asymmetric case. As shown numerically by [160] for a dielectric reconfigurable metamaterial, different optical forces F_{z1} and F_{z2} along the propagation direction should be expected for both structures and should be strongest near absorption resonances.

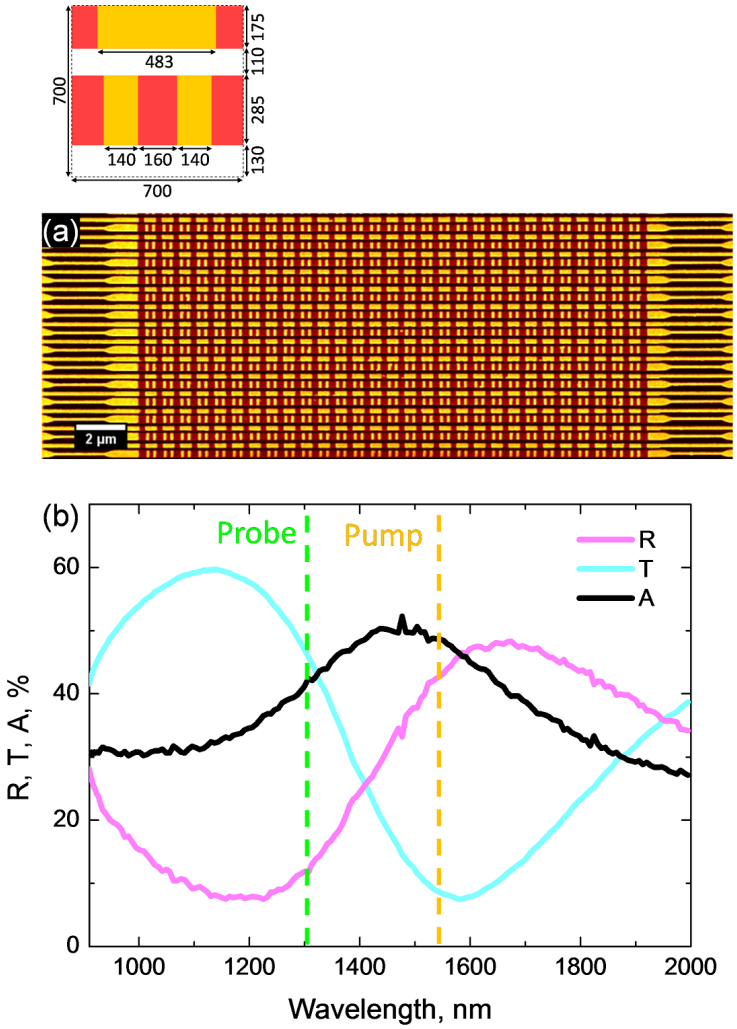

Figure 5.4: **Optically reconfigurable photonic metamaterial with symmetric plasmonic resonators.** (a) Scanning electron microscope image of a metamaterial nanostructure consisting of symmetrically spaced gold (yellow) resonators on silicon nitride bridges (red). The inset shows detailed dimensions of the unit cell in nanometers. (b) Transmission T, reflection R and absorption A spectra of the symmetric metamaterial for x-polarized light. Dashed lines indicate the optical 1310 nm probe and 1550 nm pump wavelengths used in the modulation measurements.

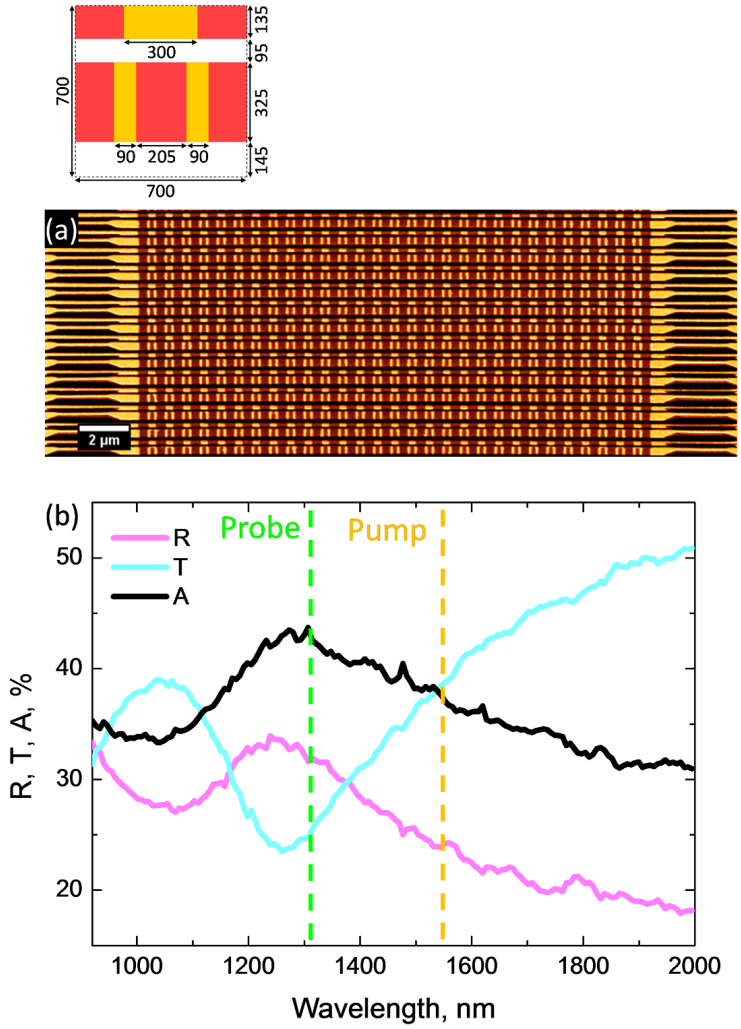

Figure 5.5: **Optically reconfigurable photonic metamaterial with asymmetric plasmonic resonators.** (a) Scanning electron microscope image of a metamaterial nanostructure consisting of asymmetrically spaced gold (yellow) resonators on silicon nitride bridges (red). The inset shows detailed dimensions of the unit cells in nanometers. (b) Transmission T, reflection R and absorption A spectra of the asymmetric metamaterial for x-polarized light. Dashed lines indicate the optical 1310 nm probe and 1550 nm pump wavelengths used in the modulation measurements.

5.3.2 Device Characterization and Results

Measurement setup: The reconfigurable metamaterial's transmission and reflection spectra were recorded using a microspectrophotometer (CRAIC Technologies), see Fig. 5.4(b) and Fig. 5.5(b).

High frequency optomechanical modulation (Figs 5.8 and 5.9) was studied by measuring the modulation of a 1310 nm probe laser beam (peak intensity 80 W/cm^2, FWHM

26 μm) transmitted through the nanostructure, while modulating the metamaterial using a 1550 nm pump laser focused to 15 μm FWHM on the sample, see Fig. 5.8(a). The modulated signal was detected by an InGaAs photodetector (New Focus 1811) and a lock-in amplifier (Stanford Research SR844). The pump laser was modulated with a fiber coupled electro-optical modulator (JDSU 2.5Gb/s Bias Free Modulator) using the reference signal from the lock-in amplifier. In all optical experiments the incident electric field was polarized parallel to the bridges.

Measurements and full 3D Maxwell simulations reveal a pronounced absorption resonance in the near infrared, located around 1470 nm and 1270 nm for the symmetric and asymmetric metamaterials, respectively, compare Figs 5.4(b), 5.5(b) and 5.6(a), 5.7(a). Maxwell stress tensor calculations [160] reveal optical forces acting on the Π-resonators around the resonance wavelength, see Fig. 5.6(b,c) and Fig. 5.7(b,c). We consider normal incidence far-field illumination of a non-diffracting, periodic metamaterial, that is placed far away from any other objects. As the normally incident photons only carry momentum along the z-direction, there cannot be any net in-plane optical forces on the unit cell, $F_{y1} + F_{y2} = 0$, and the net force along the z-direction must be given by the momentum transfer associated with absorption and reflection, $F_{z1} + F_{z2} = (A + 2R)P/c$, where A is absorption, R is reflection, P is the incident power per unit cell and c is the speed of light in vacuum. In close agreement with these relationships, our simulations show substantial relative optical forces acting on different components of the unit cell. The relative optical forces $F_2 - F_1$ between the unit cell's bridge segments reach about 0.4 P/c along y and about 3 P/c along z. The simulations predict smaller in-plane forces for the more symmetric metamaterial design than for the more asymmetric one. These in-plane forces can be understood from the charge distributions at the pump and probe wavelengths, see Figs. 5.6(a) and 5.7(a). In case of the more asymmetric structure at the probe wavelength of 1310 nm, repulsive forces between the bridges are linked to Coulomb forces between equal charges. Attractive in-plane forces in the other cases are linked to attractive Coulomb forces between opposite charges.

In order to optomechanically modulate the metamaterials' optical properties, we pumped the nanostructures with a modulated laser beam at 1550 nm just above their absorption resonances, where simulations predict significant relative forces on the bridges along z for the symmetric structure and along y for the asymmetric structure. The modulation of the metamaterial's transmission was probed at 1310 nm and detected using a lock-in amplifier, see Fig. 5.8(a) for details. Generally, both pump and probe

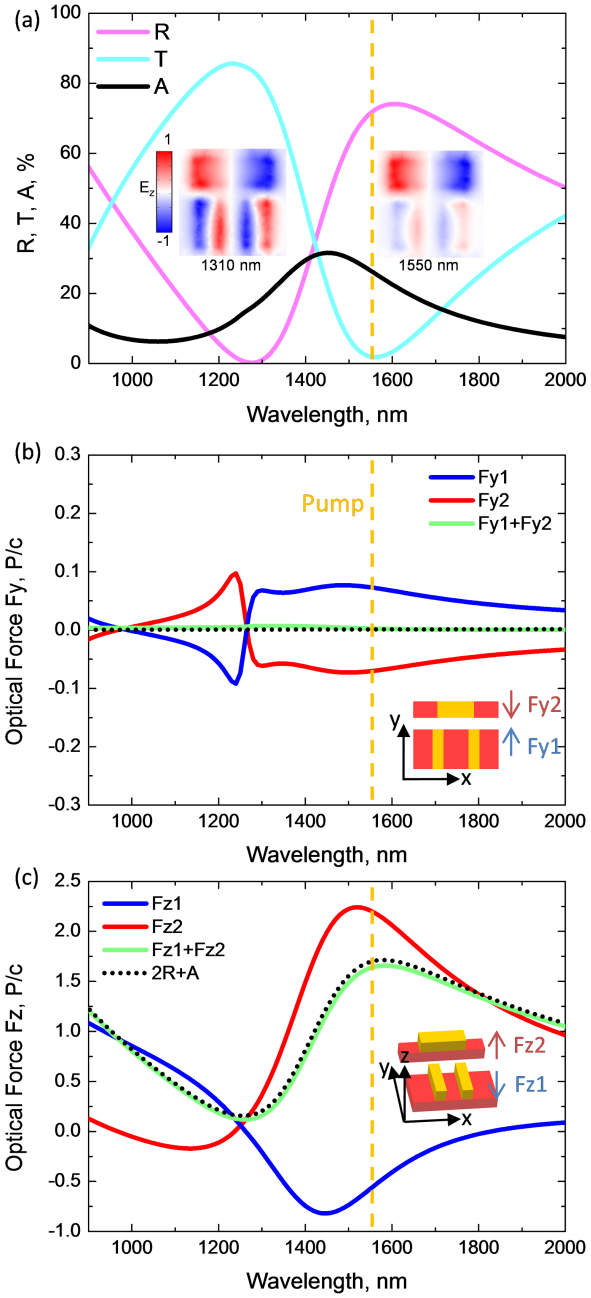

Figure 5.6: **Simulation of optical properties and optical forces for optically reconfigurable metamaterial with symmetric plasmonic resonators.** (a) Simulated transmission, reflection and absorption spectra. Insets show the charge distributions at the wavelengths of 1310nm and 1550nm in terms of E_z just above the gold surface. (b) Corresponding in-plane optical forces $F_{y1,2}$ between the bridge segments of an individual 700 nm × 700 nm unit cell. (c) Optical forces $F_{z1,2}$ on the bridge segments along the propagation direction. The total optical force on the unit cell is indicated by a green line, while the expected value based on light pressure, reflection and absorption is represented by a dotted black line in panels (b-c). All forces are shown per unit cell in units of P/c, where P is the incident power per unit cell and c is the speed of light in vacuum. Dashed lines indicate the 1550 nm optical pump wavelength used in the modulation measurements and the direction of optical forces at this wavelength is indicated by arrows. All quantities are shown for x-polarized illumination from the silicon nitride side.

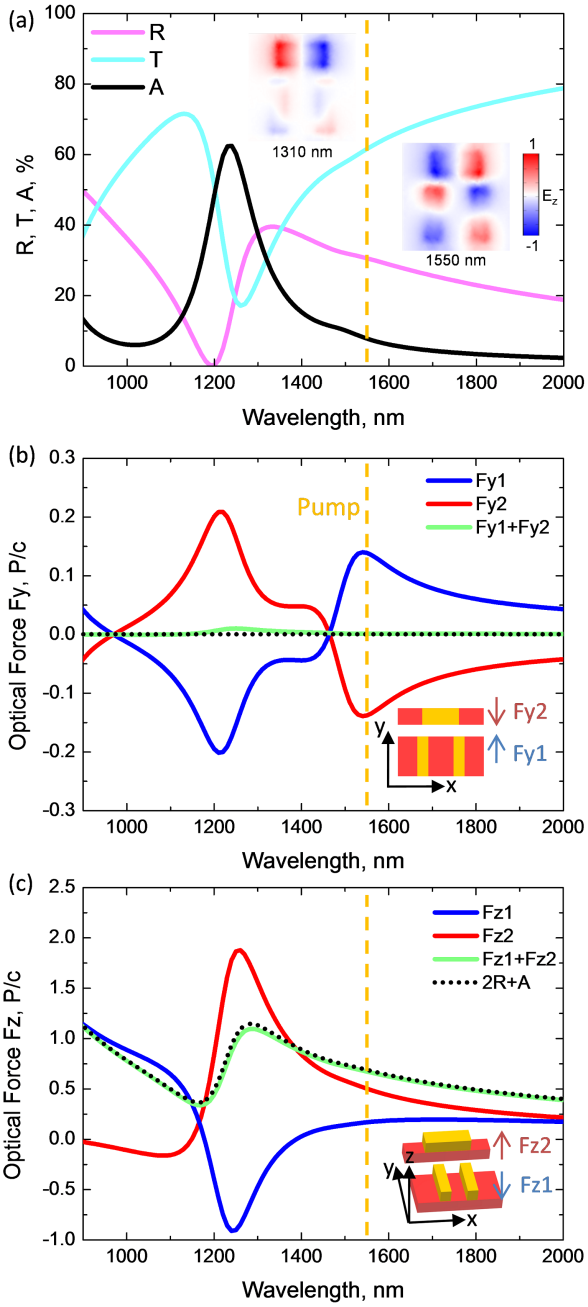

Figure 5.7: **Simulations of optical properties and optical forces for reconfigurable metamaterials with asymmetric plasmonic resonators.** (a) Simulated transmission, reflection and absorption spectra. Insets show the charge distributions at the wavelengths of 1310nm and 1550nm. (b) Corresponding in-plane optical forces $F_{y1,2}$ between the bridge segments of an individual 700 nm × 700 nm unit cell. (c) Optical forces $F_{z1,2}$ on the bridge segments along the propagation direction. The total optical force on the unit cell is indicated by a green line, while the expected value based on light pressure, reflection and absorption is represented by a dotted black line in panels (b-c). All forces are shown per unit cell in units of P/c, where P is the incident power per unit cell and c is the speed of light in vacuum. Dashed lines indicate the 1550 nm optical pump wavelength used in the modulation measurements and the direction of optical forces at this wavelength is indicated by arrows. All quantities are shown for x-polarized illumination from the silicon nitride side.

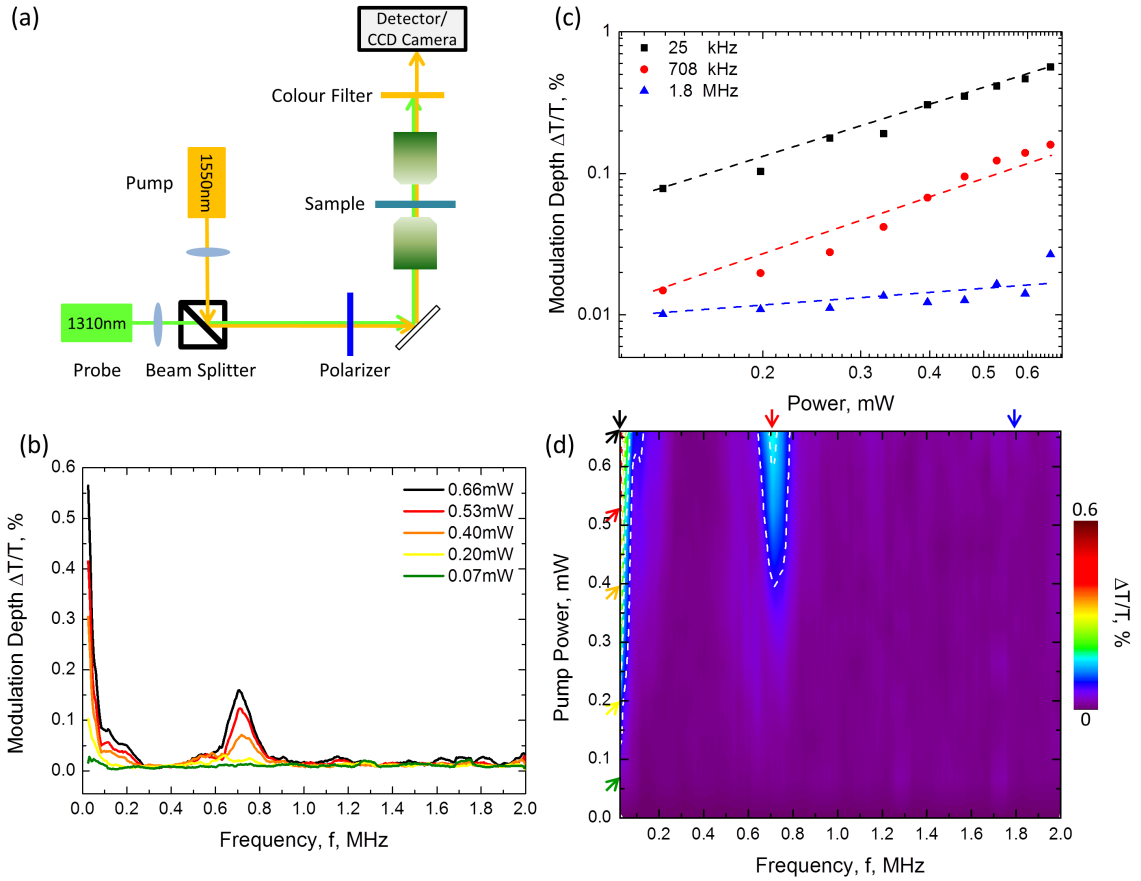

Figure 5.8: **Modulating light with light (symmetric metamaterial).** (a) Schematic of the pump-probe experimental setup. Both pump and probe beams are x-polarized and the samples are illuminated from the silicon nitride side in all cases. (b) Modulation depth as a function of modulation frequency for selected pump powers. (c) Modulation depth as a function of pump power for selected modulation frequencies. (d) Colour map showing modulation depth as a function of modulation frequency and pump power. The selected pump powers and modulation frequencies shown on the previous graphs are marked by arrows.

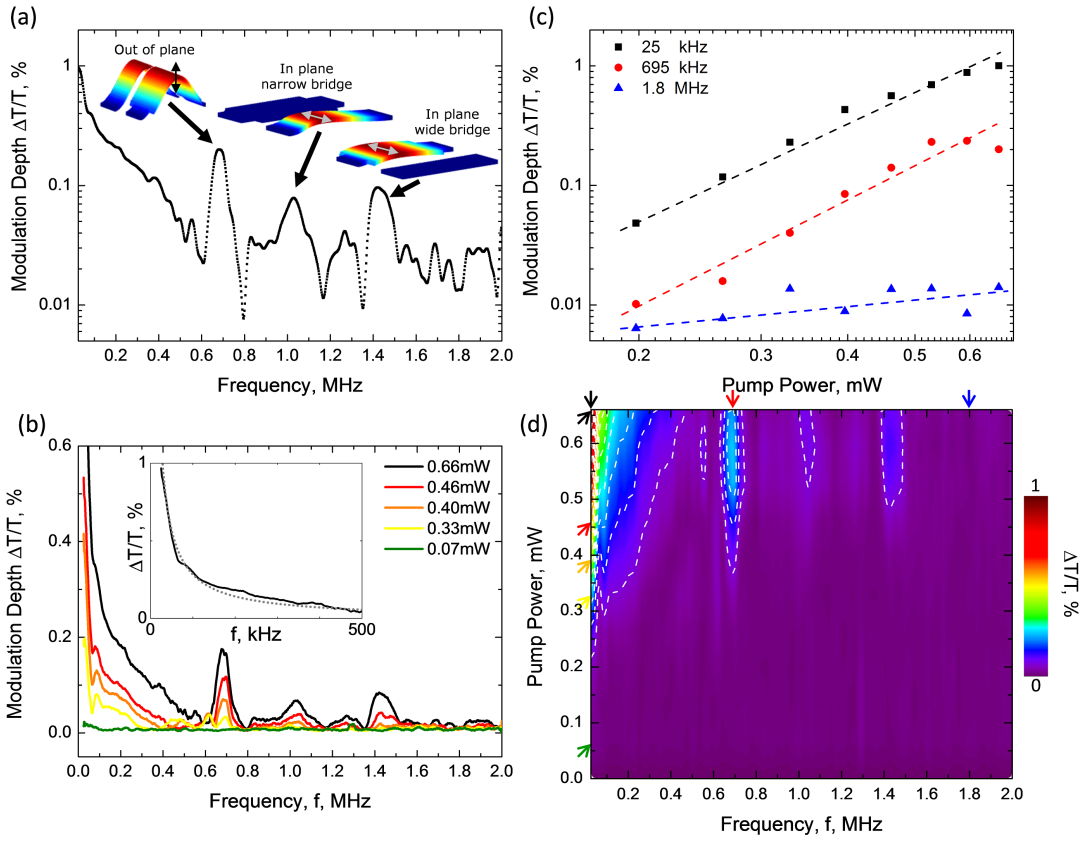

Figure 5.9: **Observation of optical forces (asymmetric metamaterial).** (a) Modulation depth as a function of modulation frequency for a pump power of 0.66 mW on a logarithmic scale, where simulations of the mechanical eigenmodes are shown as insets. (b) Modulation depth as a function of modulation frequency for selected pump powers. The inset shows a hyperbolic fit $\sim 1/f$ of the thermal modulation tail for a pump power of 0.66 mW. (c) Modulation depth as a function of pump power for selected modulation frequencies. (d) Colour map showing modulation depth as a function of modulation frequency and pump power. The selected pump powers and modulation frequencies shown on the previous graphs are marked by arrows.

beams will lead to optical forces, deformation of the nanostructure and associated optical effects. However, in the experiments optical modulation caused by the modulated pump beam will be modulated at the pump modulation frequency and detected by the lock-in amplifier, while any constant changes in optical properties associated with the continuous probe beam will not be detected. Therefore, the detected transmission modulation at the probe wavelength is caused by the pump beam alone.

At modulation frequencies of 10s of kHz, the optical pump leads to pronounced modulation of the metamaterial's transmission characteristics at the probe wavelength, see Figs 5.8(b) and 5.9(b). For a pump power of 0.66 mW (peak intensity I =250 W/cm^2) a modulation amplitude on the order of 1% is detected at 25 kHz modulation for both samples. However, the modulation amplitude drops rapidly with increasing modulation frequency, approaching the detection limit of about 0.0025% at a few 100s of kHz. The rapid decay in the modulation amplitude at kHz frequencies points towards a thermal origin of the effect. Indeed, in this frequency range, the modulation amplitude approximately halves as the modulation frequency doubles (leaving half the time for heating/cooling), leading to a hyperbolic frequency dependence which is consistent with driving a thermal process above the characteristic cooling timescale, see inset to Fig. 5.9(b). This is consistent with detailed calculations based on the law of heat conduction and literature values for the thermal properties of 50 nm thick films of gold [127] and silicon nitride [128], which predict conductive cooling timescales on the order of 20-30 μs, implying that thermal modulation processes become inefficient at 10s of kHz, see section 5.2.3. While the thermal modulation process easily dominates at low frequencies, it becomes less important above the characteristic cooling timescale, so that other modulation mechanisms may dominate at sufficiently high modulation frequencies.

Importantly, optical modulation of the metamaterial transmission is also seen at much higher frequencies. A resonant peak in the transmission modulation amplitude reaching about 0.2% around 700 kHz is seen for both nanostructures, compare Figs 5.8 and 5.9. Through mechanical eigenmode calculations (see section 5.2.2), the resonance has been identified as the fundamental mechanical resonance of the bridges, which oscillate normal to the metamaterial plane (inset to Fig. 5.9(a)). Considering that the heating and cooling cycles (0.7 μs each) are very short compared to the bridges' characteristic cooling timescale at this resonance, one may expect that the high frequency modulation is of non-thermal origin. Even more intriguing modulation peaks have been observed at 1 MHz and 1.4 MHz for the asymmetric metamaterial only (Fig. 5.9(a)). Eigenmode cal-

culations show that these correspond to the fundamental in-plane modes of the narrow and wide bridges, indicating that their excitation must be linked to in-plane forces.

The thermal origin of the low frequency modulation can be easily understood by considering how the nanostructure is heated by the pump beam. The peak temperature at the centre of the beams can be estimated by solving the heat equation for heat transport along the metamaterial bridges (radiative cooling is negligible). For 0.66 mW pump power (peak intensity 250 W/cm^2), 30% absorption at the pump wavelength and assuming 2 WK^{-1}m^{-1} [128] for the thermal conductivity of silicon nitride (which is not accurately known for nanoscale layers) the equilibrium temperature is on the order of 300 K above room temperature, see section 5.2.3. The thermal expansion coefficient of gold (14.4 $\times 10^{-6}$/K) exceeds that of silicon nitride (2.8 $\times 10^{-6}$/K) by a factor of 5 and therefore optical heating leading to a temperature change on the order of 100s of Kelvin will lead to bending of the bridges. In a reconfigurable nanostructure designed to show large changes in optical properties in response to ambient temperature changes, this deformation mechanism has led to relative transmission changes of up to 50% [46]. In contrast to the cited work, in our case, the bilayered bridge design will lead to similar out-of-plane deformation of all bridges for same temperatures, with narrow bridges being raised slightly higher due to their slightly more complete gold coverage. Therefore, the overall optothermal changes of the resonator spacing and coupling, which cause changes of the optical properties, remain relatively small.

In order to assess whether the high frequency modulation may be caused by optical forces acting between different parts of of the Π-resonators, we estimate the optomechanical deformation that can be expected from this mechanism. Based on the simulations presented in Fig. 5.6(b) and (c), the optical force at the pump wavelength near the resonance reaches 2.2 P/c (0.6 P/c) for the narrow (wide) bridges, where P is the pump power incident on a unit cell and c is the speed of light in vacuum. For a bridge pair with 29 unit cells and a pump intensity of 250 W/cm^2, this corresponds to a force of about 260 fN (70 fN) per bridge. For out-of-plane deformation of silicon nitride beams (Young's modulus E = 260 GPa [125], length L = 28 μm, thickness t = 50 nm) of width w = 175 nm (285 nm) the spring constant is $k = 32Ewt^3/L^3$ =8.3 fN/pm (13.5 fN/pm) [168] and thus we may expect a change of the gap size of about 37 pm, which explains why we do not see non-resonant high-frequency modulation. However, considering the observed resonant transmission changes on the order of 0.2% and noting that a 0.2% change of the gap size would correspond to 220 pm movement, it may be expected

that resonant enhancement of the oscillation amplitude at mechanical resonances may be sufficient for observation of the deformation resulting from optical forces. Thus, it is conceivable that the 700 kHz resonance seen in the transmission modulation of both metamaterials results from resonant enhancement of mechanical oscillations caused by optical forces or the thermal modulation tail.

On the other hand, the higher frequency mechanical resonances seen only for the asymmetric structure correspond to mechanical oscillations within the metamaterial plane (Fig. 5.9), which cannot be excited by optical heating and differential thermal expansion as the thermal mechanism can only cause movement normal to the metamaterial plane. The observation of these resonances for only the asymmetric metamaterial further links them to in plane optical forces, which are larger in the asymmetric structure, reaching 0.14 P/c (17 fN) per bridge at the pump wavelength. For in-plane deformation, the mechanical properties of the bridges strongly depend on their narrowed ends. However, the in-plane spring constants may be estimated from the out-of-plane spring constants by considering that the fundamental resonance frequencies are proportional to $\sqrt{k}$ for each bridge, giving $k \sim 14$ fN/pm (60 fN/pm) for in-plane displacement of the narrow (wide) bridges of the asymmetric structure, which corresponds to a gap change of 1.5 pm. Considering the observed 0.09% transmission modulation, we note that a 0.09% gap change would correspond to 85 pm movement or about 60× resonant enhancement of the mechanical oscillation amplitude.

We note that the all-optical modulation observed here is different from the spontaneous Brownian motion observed by [169]. While the equipartition theorem predicts a Brownian oscillation amplitude on the order of $\sqrt{k_\mathrm{B}\vartheta/k}$ or a few 100 pm in vacuum at room temperature ϑ (k_B Boltzmann constant), this phenomenon is strongly damped by air in our experiments. Furthermore, it would not be seen by lock-in detection due to not being locked to the driving signal, it would continue to be present in absence of an optical pump and it would be proportional to $\sqrt{\vartheta}$, rather than the linear power and thus temperature dependence seen in our experiments (Figs. 5.8(c) and 5.9(c)).

The intensity in a nonlinear medium is conventionally described by the expression

$$-\tfrac{dI}{dz} = \alpha I + \beta I^2 + ... \tag{5.12}$$

where z is the propagation distance and α and β are the linear and nonlinear absorption coefficients. As the observed nonlinear transmission change is proportional to the pump

power, we can quantify the nonlinearity of the reconfigurable photonic metamaterial by estimating its first nonlinear absorption coefficient β. At the pump wavelength linear absorption of the asymmetric structure is about $A_{\mathrm{lin}} = 38\%$ (see Fig. 5.5(b)) in the nanostructure of $t = 100$ nm thickness and thus $\alpha \sim A_{\mathrm{lin}}/t = 3.8 \cdot 10^{-6}$ m^{-1}. Assuming that the nonlinear transmission change results from nonlinear absorption $A_{\mathrm{nl}} \sim \Delta T$, the nonlinear absorption coefficient can be estimated as $\beta \sim \Delta T/(It)$. In the low frequency limit at the pump wavelength, $\beta_{25\mathrm{kHz}} \sim 1.5 \cdot 10^{-2}$ m/W, while at the first mechanical resonance $\beta_{700\mathrm{kHz}} \sim 3 \cdot 10^{-3}$ m/W, thus, the optical nonlinearity is 7 orders of magnitude stronger than nonlinear absorption in the classic nonlinear reference medium GaAs [170].

5.4 Conclusion

In summary, we demonstrate for the first time experimentally that photonic metamaterials can be reconfigured and modulated by light. We identify and observe evidence of two mechanisms of optomechanical deformation, (i) optical heating leading to deformation of bimaterial structures and (ii) optical forces between plasmonic resonators. The resulting optical nonlinear response is gigantic, exceeding nonlinear absorption in GaAs by 7 orders of magnitude. This work opens up new opportunities for dynamic optical control of photonic metamaterials, all-optical modulation and optomechanical media with giant nonlinear responses.

6 Conclusions

6.1 Summary

This work addresses the key challenge that the enhanced or novel metamaterial functionalities seen in lab demonstrations are often narrow-band and fixed, while many potential applications require broadband or tunable functionalities. By providing practical solutions for tuning and high-contrast modulation of metamaterial optical properties, reconfigurable photonic metamaterials make an important contribution to bridging the gap between scientific proof-of-principle demonstrations and industrial applications of metamaterials. The demonstrated approach of placing nanoscale plasmonic meta-molecules on a flexible support structure that can be reconfigured with thermal, electrical or optical control signals can be applied to all sorts of meta-molecule designs, thus providing solutions for tuning and modulation of various metamaterial functionalities.

Key achievements of this work include:

- The development of sophisticated nanofabrication techniques based on focused ion beam milling / electron beam lithography for optical metamaterials and metadevices.

- Demonstration of the first thermally reconfigurable metamaterial operating in the optical part of the spectrum.

- Realization of the first electrically reconfigurable metadevice operating in the optical spectral range.

- Demonstration of the first optically reconfigurable photonic metamaterial.

Compared to reconfigurable THz metamaterials, the metadevices demonstrated here have 3 to 4 orders of magnitude smaller characteristic features and are up to 4 orders of magnitude faster. The demonstrated electro-optical effect is up to 5 orders of magnitude larger than in typical electro-optic media, while the demonstrated optomechanical nonlinarity exceeds typical nonlinar optical media by about 7 orders of magnitude.

6.2 Outlook

The experiments reported in this thesis are mainly "proof of concept" demonstrations. Each of them though shows that there is room for further studies for each of the three types of reconfigurable photonic metamaterials investigated. Here, a very brief outlook is given on what it is still left to do for each of the three directions. In this thesis, I have developed solutions for rearranging metamaterial structures on the nanoscale in response to thermal, electrical or optical control signals, offering practical solutions for tuning, high contrast switching and modulation of optical metamaterial functionalities. This added layer of functionality – which provides metamaterial optical properties on demand – provides real added value for potential commercial applications. I expect that this concept will be developed further towards addressable reconfigurable metamaterials, which will eventually provide optical properties on demand at any point in time and space. This would allow breakthrough applications, such as programmable transformation optics devices, holographic 3D displays and filters for spatial mode multiplexing in optical fibre communications. I note that reconfigurable photonic metamaterials can be easily prototyped by focussed ion beam milling or electron beam lithography and could be mass-produced by standard semiconductor manufacturing techniques.

Temperature Controlled Reconfigurable Photonic Metamaterials

In chapter 3, we show that thermally controlled reconfigurable photonic metamaterials provide a flexible platform for the realization of tunable metamaterials for the optical part of the spectrum by ambient temperature and electrothermally control. By placing nanoscale plasmonic resonators with useful functionalities at optical frequencies on reconfigurable support structures, their interaction can be controlled, which leads to large-range tunability of the system's electromagnetic properties. Potential applications of this generic approach include optical temperature sensors, tunable spectral filters, switches, modulators and any other planar metamaterial device where tunability is re-

quired or desirable.

Furthermore, under application of external magnetic field, the electrical current can deliver not only Joule heat to reconfigurable metamaterials but also introduce the magnetic Lorentz force which leads to a magneto-electric control mechanism for reconfigurable metamaterials. This magneto-electric effect promises applications in optical magnetic field sensing.

Electrostatically Controlled Reconfigurable Photonic Metamaterials

The development of electrostatically controlled reconfigurable metamaterials in chapter 4 provides high contrast switching and electro-optical modulation at modulation frequencies up to 1 MHz. Building on this work and aiming to demonstrate the potential of reconfigurable metamaterials for fast electro-optic modulation and addressable modulators, we shrink the characteristic size of the electrostatically driven metamaterial from 35 μm down to for example, 9 μm. As the mechanical resonance frequency of the bridges is inversely proportional to the square of their length, this drives up the achievable modulation rates. Electrical modulation of this metamaterial's optical properties can be detected up to its mechanical resonances around 20 MHz. We expect that, in principle, reconfigurable elements on the size scale of the meta-molecules (1 μm or less) would allow GHz modulation rates.

Optically Controlled Reconfigurable Photonic Metamaterials

We demonstrate experimentally that photonic metamaterials can be reconfigured and modulated by light in chapter 5. The optomechanical deformation resulting from optical forces between plasmonic resonators leads to a gigantic nonlinear optical response. This work opens up new opportunities for dynamic optical control of photonic metamaterials, all-optical modulation and optomechanical media with giant nonlinear responses. In particular, optically reconfigurable metamaterials allow the realization of adaptable transformation optics devices that are controlled by the pattern of pump illumination.

A

Publications

Journal Publications

Papers on Metamaterials

1. **J. Y. Ou**, J. K. So, G. Adamo, A. Sulaev, L. Wang, and N. I. Zheludev. Ultraviolet and visible range plasmonics in the topological insulator $Bi_{1.5}Sb_{0.5}Te_{1.8}Se_{1.2}$ Nature Comms., 5, 5139 (2014)

2. X. Fang, M. L. Tseng, **J. Y. Ou**, K. F. MacDonald, D. P. Tsai, and N. I. Zheludev. Ultrafast all-optical switching via coherent modulation of metamaterial absorption. Appl. Phys. Lett., 104, 141102 (2014)

3. **J. Y. Ou**, E. Plum, J. Zhang, and N. I. Zheludev. An electromechanically reconfigurable plasmonic metamaterial operating in the near-infrared. Nat. Nanotech. 8, 252-255 (2013)

4. O. Buchnev, **J. Y. Ou**, M. Kaczmarek, N. I. Zheludev, and V. A. Fedotov. Electro-optical control in a plasmonic metamaterial hybridised with a liquid-crystal cell. Opt. Express 21(2), 1633 (2013)

5. G. Adamo, **J. Y. Ou**, J. K. So, S. D. Jenkins, F. De Angelis, K. F. MacDonald, E. Di Fabrizio, J. Ruostekoski, and N. I. Zheludev. Electron-Beam-Driven Collective-Mode Metamaterial Light Source. Phys. Rev. Lett. 109, 217401 (2012)

6. J. Zhang, **J. Y. Ou**, K. F. MacDonald and N. I. Zheludev. Optical response of plasmonic relief meta-surfaces. J. Opt. 14, 114002 (2012)

7. T. S. Kao, E. T. F. Rogers, **J. Y. Ou**, and N. I. Zheludev. "Digitally" addressable focusing of light into a subwavelength hot spot. Nano Lett. 12, 2728 (2012)

8. V. A. Fedotov, T. Uchino, and **J. Y. Ou**. Low-loss plasmonic metamaterial based on epitaxial gold monocrystal film. Opt. Express 20(9), 9545 (2012)

9. J. Zhang, **J. Y. Ou**, N. Papasimakis, Y. Chen, K. F. MacDonald, and N. I. Zheludev. Continuous metal plasmonic frequency selective surfaces. Opt. Express 19(23), 23279 (2011)

10. M. Ren, B. Jia, **J. Y. Ou**, E. Plum, J. Zhang, K. F. MacDonald, A. E. Nikolaenko, J. Xu, M. Gu, N. I. Zheludev. Nanostructured plasmonic medium for terahertz bandwidth all-optical switching. Adv. Mater. 23, 5540 (2011)

11. **J. Y. Ou**, E. Plum, L. Jiang, and N. I. Zheludev. Reconfigurable photonic metamaterials. Nano Lett. 11(5), 2142-2144 (2011)

12. K. Tanaka, E. Plum, **J. Y. Ou**, T. Uchino, and N. I. Zheludev. Multifold enhancement of quantum dot luminescence in plasmonic metamaterials. Phys. Rev. Lett. 105, 227403 (2010)

Papers on Other Topics

1. B. Gholipour, C.C.Huang, **J. Y. Ou**, & D.W. Hewak. Germanium antimony lateral nanowire phase change memory by chemical vapor deposition. Phys. Status. Solidi. B, 250(5), 994-998(2013)

2. C. C. Huang, B. Gholipour, K. Knight, **J. Y. Ou**, and D. W. Hewak. Deposition and Characterization of CVD-Grown Ge-Sb Thin Film Device for Phase-Change Memory Application. Advances in OptoElectronics 2012, 840348 (2012)

3. M. Ding, O. Fenwick, F. D. Stasio, **J. Y. Ou**, N. Sessions, Y. Jung, F. Cacialli, G. Brambilla. Efficient light confinement with nanostructured optical microfiber tips.Opt. Commun. 285, 4688-4697(2012)

4. C. C. Huang, B. Gholipour, **J. Y. Ou**, K. J. Knight, and D. W. Hewak. Electrical phase change of CVD-grown Ge-Sb-Te thin film device. Electron. Lett. 47, 288 (2011)

5. K. S. Kaur, M. Feinäugle, D. P. Banks, **J. Y. Ou**, F. Di Pietrantonio, E. Verona, C. L. Sones, and R. W. Eason. Laser-induced forward transfer of focussed ion beam pre-machined donors. Appl. Surf. Sci. 257, 6650 (2011)

Manuscripts in Preparation

- **J. Y. Ou**, E. Plum, J. Zhang, and N. I. Zheludev. Giant Optical Nonlinearity through Reconguring Photonic Metamaterials with Light. in preparation

Non-peer Reviewed Publications

- J. Zhang, **J. Y. Ou**, N. Papasimakis, Y. Chen, K. F. MacDonald, and N. I. Zheludev. "Control of metal color using surface relief metamaterial nanostructuring". SPIE Newsroom, 2012. DOI: 10.1117/2.1201201.004119

Patent Applications

- B. Jia, K. Macdonald, A. Nikolaenko, **J. Y. Ou**, E. Plum, M. Ren, J. Zhang, and N. I. Zheludev. Non-linear materials and related devices. Publication number US20120293854 A1, 16 May 2011 Granted as patent GB2490895

- N. I. Zheludev, E. Plum, and **J. Y. Ou**. Tunable metamaterials and related devices. Publication number US20120327502 A1, 24 Jun 2011

- N. I. Zheludev, K. F. MacDonald, N. Papasimakis, J. Zhang, **J. Y. Ou**, "Method And Device For Controlling The Color Of Metals". US Application 13/182,084 (13/070/2011); GB Application 1011720.8 (13/07/2010)

Conference Contributions

My name is underlined where I was the presented author.

1. Nano-Opto-Mechanical Nonlinear Plasmonic Metamaterials **J. Y. Ou**, E. Plum, N. I. Zheludev Nanometa 2015, Seefeld, Austria, 5 - 8 Jan 2015

2. (Poster) Randomly Addressable Reconfigurable Photonic Metamaterials P. Cencillo, **J. Y. Ou**, J. Valente, E. Plum, N. I. Zheludev Nanometa 2015, Seefeld, Austria, 5 - 8 Jan 2015

3. Topological Insulator BSTS as a Broadband Switchable Metamaterial **J. Y. Ou**, J. K. So, G. Adamo, Z. Wang, J. Yin, S. Vezzoli, V. Nalla, L. Wang, C. Soci, N. I. Zheludev 2014 MRS Fall Meeting, Boston, MA, USA, 30 Nov - 5 Dec 2014

4. Ultraviolet and visible plasmonic metamaterials made of topological insulator **J. Y. Ou**, J. K. So, G. Adamo, A. Sulaev, L. Wang, and N. I. Zheludev Photon14, London, 1 - 4 Sep 2014

5. (invited) Giant optical nonlinearity and magnetoelectric effect in reconfigurable plasmonic metamaterials E. Plum, J. Valente, **J. Y. Ou**, K. F. MacDonald, and N. I. Zheludev Metamaterials'2014, Copenhagen, Denmark, 25 - 30 Aug 2014

6. Metamaterial NEMS: Giant optical nonlinearity and magnetoelectric effect J. Valente, **J. Y. Ou**, E. Plum, K. F. MacDonald, and N. I. Zheludev OMN2014 - International Conference on Optical MEMS and Nanophotonics, Glasgow, Scotland, 17 - 21 Aug 2014

7. Lorentz Force Metamaterial with Giant Optical Magnetoelectric Response J. Valente, **J. Y. Ou**, E. Plum, I. Youngs, and N. I. Zheludev CLEO:2014, San Jose, CA, USA, 8 - 13 Jun 2014

8. Controlling Light with Light in a Plasmonic Nanooptomechanical Metamaterial **J. Y. Ou**, E. Plum, J. Zhang and N. I. Zheludev CLEO:2014, San Jose, CA, USA, 8 - 13 Jun 2014

9. UV & Visible Plasmonic Metamaterials Made of Topological Insulator **J. Y. Ou**, J. K. So, G. Adamo, A. Sulaev, L. Wang, and N. I. Zheludev CLEO:2014, San Jose, CA, USA, 8 - 13 Jun 2014

10. (invited) Plasmonics of topological Insulators at UV-Visible frequencies **J. Y. Ou**, J. K. So, G. Adamo, A. Sulaev, L. Wang, and N. I. Zheludev META'14, Singapore, 20 - 23 May 2014

11. (invited) Nanomechanical metamaterial light modulators E. Plum, **J. Y. Ou**, J. Valente, P. Cencillo, and N. I. Zheludev META'14, Singapore, 20 - 23 May 2014

12. Reconfigurable photonics metamaterials: Nanoscale forces and giant magnetoelectric effect J. Valente, E. Plum, **J. Y. Ou**, and N. I. Zheludev DSTL Novel Electronic Materials PhD Theme Event, London, 17 Dec 2013

13. (poster) Reconfigurable photonics metamaterial: Observation of a giant magneto-electric effect J. Valente, E. Plum, **J. Y. Ou**, and N. I. Zheludev DSTL Novel Electronic Materials PhD Theme Event, London, 17 Dec 2013

14. Electrically controlled liquid crystal plasmonic metamaterials O. Buchnev, **J. Y. Ou**, M. Kaczmarek, N. I. Zheludev, and V. A. Fedotov Optics of Liquid Crystals 2013, Honolulu, Hawaii, 29 Sep - 4 Oct 2013

15. Switching near-IR metamaterial response with electrically-controlled liquid crystals O. Buchnev, **J. Y. Ou**, M. Kaczmarek, N. I. Zheludev, and V. A. Fedotov Conference on Liquid Crystals ECLC-2013, Rhodes, Greece, 22 - 27 Sep 2013

16. (keynote) Driving reconfigurable photonic metamaterials with light and electrical signals: Exploiting forces and fields at the nanoscale N. I. Zheludev, E. Plum, K. F. MacDonald, **J. Y. Ou**, J. Zhang, J. Valente, W. M. Zhu, and A. Q. Liu Metamaterials' 2013, Bordeaux, France, 16 - 19 Sep 2013

17. Electrically tunable liquid crystal plasmonic metamaterials O. Buchnev, **J. Y. Ou**, M. Kaczmarek, N. I. Zheludev, and V. A. Fedotov Metamaterials' 2013, Bordeaux, France, 16 - 19 Sep 2013

18. (invited) Reconfigurable photonic metamaterials driven by Coulomb, Lorentz and optical forces E. Plum, **J. Y. Ou**, J. Valente, and N. I. Zheludev International Conference on Nanomaterials 2013 (ICN 2013), London, Ontario, Canada, 12 - 16 Aug 2013

19. (invited) Amplifying free-electron evanescent fields J. K. So, **J. Y. Ou**, G. Adamo, F. J. G. de Abajo, K. F. MacDonald, and N. I. Zheludev SPP6, Ottawa, Canada, 26 - 31 May 2013

20. Reconfigurable metamaterials controlled by Lorentz, Ampere and Coulomb forces: towards GHz bandwidth J. Valente, E. Plum, **J. Y. Ou**, and N. I. Zheludev CLEO/Europe - IQEC 2013, Munich, Germany, 12 - 16 May 2013

21. Tunable light emission in reconfigurable plasmonic metamaterials G. Adamo, W. T. Chen, E. Plum, **J. Y. Ou**, J. K. So, D. P. Tsai, and N. I. Zheludev CLEO/Europe - IQEC 2013, Munich, Germany, 12 - 16 May 2013

22. Electrically controlled liquid crystal plasmonic metamaterials O. Buchnev, **J. Y. Ou**, M. Kaczmarek, N.I. Zheludev, and V. A. Fedotov CLEO/Europe - IQEC 2013, Munich, Germany, 12 - 16 May 2013

23. Optical magnetism in all-dielectric metamaterials J. Zhang, **J. Y. Ou**, K. F. MacDonald, and N. I. Zheludev CLEO/Europe - IQEC 2013, Munich, Germany, 12 - 16 May 2013

24. (poster) Plasmonic amplifier of the evanescent field of free electrons J. K. So, **J. Y. Ou**, G. Adamo, F. J. Garcıa de Abajo, K.F. MacDonald, and N. I. Zheludev CLEO/Europe - IQEC 2013, Munich, Germany, 12 - 16 May 2013

25. (invited) Plasmonic amplification of free-electron evanescent fields J. K. So, **J. Y. Ou**, G. Adamo, J. G. de Abajo, K. F. MacDonald, and N. I. Zheludev IPS Meeting 2013, Singapore, 4 - 6 Mar 2013

26. (invited) Nanomechanical control of metamaterial optical properties E. Plum, **J. Y. Ou**, J. Valente, J. Zhang and N. I. Zheludev IPS Meeting 2013, Singapore, 4 - 6 Mar 2013

27. (invited) Reconfiguring photonic metamaterials with electromagnetic forces E. Plum, **J. Y. Ou**, J. Valente, J. Zhang, and N. I. Zheludev Nanometa 2013, Seefeld, Austria, 3 - 6 Jan 2013

28. Amplifying the evanescent field of free electrons J. K. So, **J. Y. Ou**, G. Adamo, F. J. G. de Abajo, K. F. MacDonald, and N. I. Zheludev Nanometa 2013, Seefeld, Austria, 3 - 6 Jan 2013

29. Optical magnetic response in all-dielectric metamaterial J. Zhang, **J. Y. Ou**, R. Chen, M. D. B. Charlton, K. F. MacDonald,and N. I. Zheludev Nanometa 2013, Seefeld, Austria, 3 - 6 Jan 2013

30. (poster) Electrically controlled liquid-crystal cell enhanced with plasmonic metamaterial O. Buchnev, **J. Y. Ou**, M. Kaczmarek, N. I. Zheludev, V. Fedotov Nanometa 2013, Seefeld, Austria, 3 - 6 Jan 2013

31. (invited) Reconfiguring photonic metamaterials E. Plum, **J. Y. Ou**, J. Valente, J. Zhang, and N. I. Zheludev Sino-UK Workshop on Nanophotonics and Metamaterials, Beijing, China, 7 - 8 Dec 2012

32. (invited) Coherent light emission from planar plasmonic metamaterials G. Adamo, **J. Y. Ou**, J. K. So, M. Ren, E. Plum, E. T. F. Rogers, K. F. MacDonald, J. Xu, N. I. Zheludev CLEO:2012, San Jose, United States, 06 - 11 May 2012

33. Amplification of the evanescent field of free electrons J. K. So, **J. Y. Ou**, G. Adamo, K. MacDonald, J. G. de Abajo, N. I. Zheludev CLEO:2012, San Jose, United States, 06 - 11 May 2012

34. (poster) MHz bandwidth electro-optical modulator based on a reconfigurable photonic metamaterial **J. Y. Ou**, E. Plum, N. I. Zheludev CLEO:2012, San Jose, United States, 06 - 11 May 2012

35. (invited) A new way of reducing plasmonic losses V. A. Fedotov, **J. Y. Ou**, N. I. Zheludev META'12, Paris, France, 19 - 22 Apr 2012

36. (poster) Coherent emission from plasmonic metamaterials G. Adamo, **J. Y. Ou**, J. K. So, S. D. Jenkins, K. F. MacDonald, F. De Angelis, E. Di Fabrizio, J. Ruostekoski, N. I. Zheludev SPIE Photonics Europe, Brussels, Belgium, 16 - 19 Apr 2012

37. (poster) Nano-electro-mechanical switchable (NEMS) photonic metamaterial **J. Y. Ou**, E. Plum, W. T. Chen, D. P. Tsai, N. I. Zheludev SPIE Photonics Europe, Brussels, Belgium, 16 - 19 Apr 2012

38. (poster) Amplification of the evanescent field of free electrons J. K. So, **J. Y. Ou**, G. Adamo, K. F. MacDonald, F. J. Garcia de Abajo, N. I. Zheludev SPIE Photonics Europe, Brussels, Belgium, 16 - 19 Apr 2012

39. Nano-electromechanical switchable photonic metamaterials **J. Y. Ou**, E. Plum, L. Jiang, and N. I. Zheludev Metamaterials 2011, Barcelona, Spain, 10 - 15 Oct 2011

40. Giant femtosecond optical nonlinearity of gold metamaterial nanostructures M. Ren, B. Jia, **J. Y. Ou**, E. Plum, K. F. MacDonald, A. E. Nikolaenko, J. J. Xu, M. Gu, and N. I. Zheludev Metamaterials 2011, Barcelona, Spain, 10 - 15 Oct 2011

41. (poster) Frequency selective reflectors, magnetic walls and perfect optical absorbers based on new classes of metal and dielectric-loaded relief metamaterials J. Zhang,

J. Y. Ou, T. Uchino, K. F. MacDonald, and N. I. Zheludev Metamaterials 2011, Barcelona, Spain, 10 - 15 Oct 2011

42. (invited) Functional photonic metamaterials M. Ren, **J. Y. Ou**, B. Jia, E. Plum, J. Zhang, L. Jiang, A. Nikolaenko, J. J. Xu, M. Gu, K. F. MacDonald, and N. I. Zheludev IEEE Photonics 2011, Arligton, VA, USA, 09 - 13 Oct 2011

43. (invited) Manipulating light with photonic metamaterials **J. Y. Ou**, T. S. Kao, J. Zhang, E. Plum, K. F. MacDonald, and N. I. Zheludev SPIE Optics & Photonics 2011, San Diego, CA, USA, 21-25 Aug 2011

44. (keynote)Reconfigurable Photonic Metamaterials **J. Y. Ou**, E. Plum, L. Jiang, and N. I. Zheludev ICMAT 2011, Suntec, Singapore, 26 Jun - 01 Jul 2011

45. Electron-beam-driven nanoscale metamaterial light G. Adamo, **J. Y. Ou**, K. F. MacDonald, F. De Angelis, E. Di Fabrizio, and N. I. Zheludev CLEO/Europe - EQEC 2011, Munich, Germany, 22-26 May 2011

46. Reconfigurable Nanostructured Photonic Metamaterials **J. Y. Ou**, E. Plum, L. Jiang, and N. I. Zheludev CLEO/Europe - EQEC 2011, Munich, Germany, 22-26 May 2011

47. Reconfigurable Photonic Metamaterials **J. Y. Ou**, E. Plum, S. Savo, L. Jiang, and N. I. Zheludev CLEO/QELS 2011, Baltimore, Maryland, US, 1-6 May 2011

48. (invited) Metamaterials: novel functionalities and meta-molecular interactions E. Plum, **J. Y. Ou**, K. Tanaka, G. Adamo, A. Nikolaenko, and N. I. Zheludev UKIERI Workshop, Aurangabad, Maharashtra, India, 14 - 16 Apr 2011

49. Intaglio and Bas-Relief Metamaterials: Controlling the Colour of Metals J. Zhang, **J. Y. Ou**, N. Papasimakis, Y. Chen, K. F. MacDonald, and N. I. Zheludev NANOMETA 2011, Seefeld, Austria, 3-6 Jan 2011

50. (poster) The Super-oscillating Superlens E. T. F. Rogers, T. Roy, T. S. Kao, **J. Y. Ou**, V. Savinov, S. Sano, J. Lindberg, M. R. Dennis, and N. I. Zheludev NANOMETA 2011, Seefeld, Austria, 3-6 Jan 2011

51. (poster) Reconfigurable Photonic Metamaterials **J. Y. Ou**, E. Plum, L. Jiang, and N. I. Zheludev NANOMETA 2011, Seefeld, Austria, 3-6 Jan 2011

52. Multi-fold quantum dot luminescence enhancement in a plasmonic metamaterial K. Tanaka, E. Plum, **J. Y. Ou**, T. Uchino, and N. I. Zheludev NANOMETA 2011, Seefeld, Austria, 3-6 Jan 2011

References

[1] J. B. Pendry, "Negative refraction makes a perfect lens," *Phys. Rev. Lett.*, vol. 85, no. 18, pp. 3966–3969, 2000.

[2] J. B. Pendry, D. Schurig, and D. R. Smith, "Controlling electromagnetic fields," *Science*, vol. 312, no. 5781, p. 1780, 2006.

[3] D. R. Smith, J. Pendry, and M. C. K. Wiltshire, "Metamaterials and negative refractive index," *Science*, vol. 305, no. 5685, p. 788, 2004.

[4] R. A. Shelby, D. R. Smith, and S. Schultz, "Experimental verification of a negative index of refraction," *Science*, vol. 292, p. 77, 2001.

[5] T. J. Yen, W. J. Padilla, N. Fang, D. C. Vier, D. R. Smith, J. B. Pendry, D. N. Basov, and X. Zhang, "Terahertz magnetic response from artificial materials," *Science*, vol. 303, no. 5663, pp. 1494–1496, 2004.

[6] N. I. Zheludev, S. L. Prosvirnin, N. Papasimakis, and V. A. Fedotov, "Lasing spaser," *Nature Photon.*, vol. 2, no. 6, pp. 351–354, 2008.

[7] K. L. Tsakmakidis, A. D. Boardman, and O. Hess, "Trapped rainbow storage of light in metamaterials," *Nature*, vol. 450, no. 7168, pp. 397–401, 2007.

[8] N. I. Zheludev, "A roadmap for metamaterials," *Optics and Photonics News*, vol. 22, no. 3, pp. 30–35, 2011.

[9] N. Kanda, K. Konishi, and M. Kuwata-Gonokami, "Light-induced terahertz optical activity," *Opt. Lett.*, vol. 34, no. 19, pp. 3000–3002, 2009.

[10] H.-T. Chen, W. J. Padilla, J. M. O. Zide, A. C. Gossard, A. J. Taylor, and R. D. Averitt, "Active terahertz metamaterial devices," *Nature*, vol. 444, p. 597, 2006.

[11] A. E. Nikolaenko, F. D. Angelis, S. A. Boden, N. Papasimakis, P. Ashburn, E. D. Fabrizio, and N. I. Zheludev, "Carbon nanotubes in a photonic metamaterial," *Phys. Rev. Lett.*, vol. 104, p. 153902, 2010.

[12] Z. L. Sámson, K. F. MacDonald, F. De Angelis, B. Gholipour, K. Knight, C. C. Huang, E. Di Fabrizio, D. W. Hewak, and N. I. Zheludev, "Metamaterial electro-optic switch of nanoscale thickness," *Appl. Phys. Lett.*, vol. 96, p. 143105, 2010.

[13] T. Driscoll, H. T. Kim, B. G. Chae, B. J. Kim, Y. W. Lee, N. M. Jokerst, S. Palit, D. R. Smith, M. D. Ventra, and D. N. Basov, "Memory metamaterials," *Science*, vol. 325, no. 5947, p. 1518, 2009.

[14] F. Wang, Y. Zhang, C. Tian, C. Girit, A. Zettl, M. Crommie, and Y. R. Shen, "Gate-variable optical transitions in graphene," *Science*, vol. 320, no. 5873, p. 206, 2008.

[15] N. I. Zheludev, "The road ahead for metamaterials," *Science*, vol. 328, p. 582, 2010.

[16] H. Tao, A. C. Strikwerda, K. Fan, W. J. Padilla, X. Zhang, and R. D. Averitt, "Reconfigurable terahertz metamaterials," *Phys. Rev. Lett.*, vol. 103, p. 147401, 2009.

[17] W. M. Zhu, A. Q. Liu, X. M. Zhang, D. P. Tsai, T. Bourouina, J. H. Teng, T. Mei, G. Q. Lo, and D. L. Kwong, "Switchable magnetic metamaterials using micromachining processes," *Adv. Mater.*, vol. 23, p. 1792, 2011.

[18] Y. H. Fu, A. Q. Liu, W. M. Zhu, X. M. Zhang, D. P. Tsai, J. B. Zhang, T. Mei, J. F. Tao, H. C. Guo, X. H. Zhang, J. H. Teng, N. I. Zheludev, G. Q. Lo, and D. L. Kwong, "A micromachined reconfigurable metamaterial via reconfiguration of asymmetric split-ring resonators," *Adv. Funct. Mater.*, vol. 21, no. 18, pp. 3589–3594, 2011.

[19] W. M. Zhu, A. Q. Liu, T. Bourouina, D. P. Tsai, J. Teng, X. H. Zhang, G. Q. Lo, D. Kwong, and N. I. Zheludev, "Microelectromechanical maltese-cross metamaterial with tunable terahertz anisotropy," *Nat. Commun.*, vol. 3, p. 1274, 2012.

[20] J. B. Pendry, A. J. Holden, D. Robbins, and W. Stewart, "Magnetism from conductors and enhanced nonlinear phenomena," *Microwave Theory and Techniques, IEEE Transactions on*, vol. 47, no. 11, pp. 2075–2084, 1999.

[21] V. G. Veselago, "The electrodynamics of substances with simultaneously negative values of ε and μ," *Physics-Uspekhi*, vol. 10, no. 4, pp. 509–514, 1968.

[22] V. A. Fedotov, P. L. Mladyonov, S. L. Prosvirnin, A. V. Rogacheva, Y. Chen, and N. I. Zheludev, "Asymmetric propagation of electromagnetic waves through a planar chiral structure," *Phys. Rev. Lett.*, vol. 97, p. 167401, 2006.

[23] H. Chen, C. T. Chan, and P. Sheng, "Transformation optics and metamaterials," *Nature Mater.*, vol. 9, no. 5, pp. 387–396, 2010.

[24] D. Schurig, J. J. Mock, B. J. Justice, S. A. Cummer, J. B. Pendry, A. F. Starr, and D. R. Smith, "Metamaterial electromagnetic cloak at microwave frequencies," *Science*, vol. 314, p. 977, 2006.

[25] E. Plum, V. A. Fedotov, A. S. Schwanecke, N. I. Zheludev, and Y. Chen, "Giant optical gyrotropy due to electromagnetic coupling," *Appl. Phys. Lett.*, vol. 90, p. 223113, 2007.

[26] M. Ren, E. Plum, J. Xu, and N. I. Zheludev, "Giant nonlinear optical activity in a plasmonic metamaterial," *Nat. Commun.*, vol. 3, p. 833, 2012.

[27] G. A. Wurtz, R. Pollard, W. Hendren, G. P. Wiederrecht, D. J. Gosztola, V. A. Podolskiy, and A. V. Zayats, "Designed ultrafast optical nonlinearity in a plasmonic nanorod metamaterial enhanced by nonlocality," *Nature Nanotechnol.*, vol. 6, pp. 107–111, 2011.

[28] M. Ren, B. Jia, J. Y. Ou, E. Plum, J. Zhang, K. F. MacDonald, A. E. Nikolaenko, J. Xu, M. Gu, and N. I. Zheludev, "Nanostructured plasmonic medium for terahertz bandwidth all-optical switching," *Adv. Mater.*, vol. 23, p. 5540, 2011.

[29] M. L. Povinelli, S. G. Johnson, J. Joannopoulos, and J. Pendry, "Toward photonic-crystal metamaterials: Creating magnetic emitters in photonic crystals," *Appl. Phys. Lett.*, vol. 82, no. 7, pp. 1069–1071, 2003.

[30] J. Li, M. Hossain, B. Jia, D. Buso, and M. Gu, "Three-dimensional hybrid photonic crystals merged with localized plasmon resonances," *Opt. Express*, vol. 18, no. 5, pp. 4491–4498, 2010.

[31] P. Parimi, W. Lu, P. Vodo, J. Sokoloff, J. Derov, and S. Sridhar, "Negative refraction and left-handed electromagnetism in microwave photonic crystals," *Phys. Rev. Lett.*, vol. 92, no. 12, p. 127401, 2004.

[32] J. D. Joannopoulos, S. G. Johnson, J. N. Winn, and R. D. Meade, *Photonic crystals: molding the flow of light.* Princeton University Press, 2011.

[33] N. I. Zheludev and Y. S. Kivshar, "From metamaterials to metadevices," *Nature Mater.*, vol. 11, no. 11, pp. 917–924, 2012.

[34] I. Gil, J. Bonache, J. Garcia-Garcia, and F. Martin, "Tunable metamaterial transmission lines based on varactor-loaded split-ring resonators," *IEEE T. Microw. Theory*, vol. 54, no. 6, p. 2665, 2006.

[35] Q. Zhao, L. Kang, B. Du, B. Li, J. Zhou, H. Tang, X. Liang, and B. Zhang, "Electrically tunable negative permeability metamaterials based on nematic liquid crystals," *Appl. Phys. Lett.*, vol. 90, p. 011112, 2007.

[36] D. H. Werner, D.-H. Kwon, I.-C. Khoo, A. V. Kildishev, and V. M. Shalaev, "Liquid crystal clad near-infrared metamaterials with tunable negative-zero-positive refractive indices," *Opt. Express*, vol. 15, no. 6, pp. 3342–3347, 2007.

[37] N. Papasimakis, Z. Luo, Z. X. Shen, F. D. Angelis, E. D. Fabrizio, A. E. Nikolaenko, and N. I. Zheludev, "Graphene in a photonic metamaterial," *Opt. Express*, vol. 18, p. 8353, 2010.

[38] L. Ju, B. Geng, J. Horng, C. Girit, M. Martin, Z. Hao, H. A. Bechtel, X. Liang, A. Zettl, Y. R. Shen, and F. Wang, "Graphene plasmonics for tunable terahertz metamaterials," *Nature Nanotechnol.*, vol. 6, pp. 630–634, 2011.

[39] V. Savinov, V. A. Fedotov, S. M. Anlage, P. A. J. de Groot, and N. I. Zheludev, "Modulating sub-THz radiation with current in superconducting metamaterial," *Phys. Rev. Lett.*, vol. 109, no. 24, p. 243904, 2012.

[40] W. J. Padilla, A. J. Taylor, C. Highstrete, M. Lee, and R. D. Averitt, "Dynamical electric and magnetic metamaterial response at terahertz frequencies," *Phys. Rev. Lett.*, vol. 96, p. 107401, 2006.

[41] D. Chicherin, S. Dudorov, D. Lioubtchenko, V. Ovchinnikov, S. Tretyakov, and A. V. Räisänen, "Mems-based high-impedance surfaces for millimeter and submillimeter wave applications," *Microw. Opt. Techn. Let.*, vol. 48, no. 12, p. 2570, 2006.

[42] K. Aydin and E. Ozbay, "Capacitor-loaded split ring resonators as tunable metamaterial components," *J. of Appl. Phys.*, vol. 101, p. 024911, 2007.

[43] M. Ricci, N. Orloff, and S. Anlage, "Superconducting metamaterials," *Appl. Phys. Lett.*, vol. 87, p. 034102, 2005.

[44] M. Lapine, D. Powell, M. Gorkunov, I. Shadrivov, R. Marqués, and Y. Kivshar, "Structural tunability in metamaterials," *Appl. Phys. Lett.*, vol. 95, no. 8, p. 084105, 2009.

[45] M. Lapine, I. V. Shadrivov, D. A. Powell, and Y. S. Kivshar, "Magnetoelastic metamaterials," *Nature Mater.*, vol. 11, pp. 30–33, 2012.

[46] J. Y. Ou, E. Plum, L. Jiang, and N. I. Zheludev, "Reconfigurable photonic metamaterials," *Nano Lett.*, vol. 11, no. 5, pp. 2142–2144, 2011.

[47] A. Tsiatmas, A. R. Buckingham, V. A. Fedotov, S. Wang, Y. Chen, P. A. J. de Groot, and N. I. Zheludev, "Superconducting plasmonics and extraordinary transmission," *Appl. Phys. Lett.*, vol. 97, p. 111106, 2010.

[48] V. A. Fedotov, A. Tsiatmas, J. H. Shi, R. Buckingham, P. de Groot, Y. Chen, S. Wang, and N. I. Zheludev, "Temperature control of fano resonances and transmission in superconducting metamaterials," *Opt. Express*, vol. 18, p. 9015, 2010.

[49] K. Dani, Z. Ku, P. C. Upadhya, R. P. Prasankumar, S. R. J. Brueck, and A. J. Taylor, "Subpicosecond optical switching with a negative index metamaterial," *Nano Lett.*, vol. 9, no. 10, pp. 3565–3569, 2009.

[50] T. Driscoll, S. Palit, M. Qazilbash, M. Brehm, F. Keilmann, B. Chae, S. Yun, H. Kim, S. Cho, and N. Jokerst, "Dynamic tuning of an infrared hybrid-

metamaterial resonance using vanadium dioxide," *Appl. Phys. Lett.*, vol. 93, p. 024101, 2008.

[51] M. Gorkunov, M. Lapine, E. Shamonina, and K. H. Ringhofer, "Effective magnetic properties of a composite material with circular conductive elements," *Eur. Phys. J. B.*, vol. 28, no. 3, pp. 263–269, 2002.

[52] A. D. Boardman, V. V. Grimalsky, Y. S. Kivshar, S. V. Koshevaya, M. Lapine, N. M. Litchinitser, V. N. Malnev, M. Noginov, Y. G. Rapoport, and V. M. Shalaev, "Active and tunable metamaterials," *Laser Photon. Rev.*, vol. 5, no. 2, pp. 287–307, 2011.

[53] I. M. Pryce, K. Aydin, Y. A. Kelaita, R. M. Briggs, and H. A. Atwater, "Highly strained compliant optical metamaterials with large frequency tunability," *Nano Lett.*, vol. 10, p. 4222, 2010.

[54] V. Kaajakari, *Practical MEMS: design of microsystems, accelerometers, gyroscopes, RF MEMS, optical MEMS, and microfluidic systems.* Las Vegas, NV: Small Gear Publishing, 2009.

[55] A. Q. Liu and X. M. Zhang, "A review of mems external-cavity tunable lasers," *J. Micromech. Microeng.*, vol. 17, no. 1, p. R1, 2007.

[56] X. Xu, B. Peng, D. Li, J. Zhang, L. M. Wong, Q. Zhang, S. Wang, and Q. Xiong, "Flexible visible-infrared metamaterials and their applications in highly sensitive chemical and biological sensing," *Nano Lett.*, vol. 11, p. 3232, 2011.

[57] F. Huang and J. J. Baumberg, "Actively tuned plasmons on elastomerically driven gold nanoparticle dimers," *Nano Lett.*, vol. 10, p. 1787, 2010.

[58] T. V. Roszhart, H. Jerman, J. Drake, and C. de Cotiis, "An inertial-grade, micromachined vibrating beam accelerometer," in *The 8th International Conference on Solid-State Sensors and Actuators, 1995 and Eurosensors IX. Transducers' 95*, 1995, pp. 656–658.

[59] M. Engesser, A. R. Franke, M. Maute, D. C. Meisel, and J. G. Korvink, "Miniaturization limits of piezoresistive mems accelerometers," *Microsyst. Technol.*, vol. 15, no. 12, pp. 1835–1844, 2009.

[60] J. Zhou, S. Dasgupta, H. Kobayashi, J. M. Wolff, H. E. Jackson, and J. T. Boyd, "Optically interrogated MEMS pressure sensors for propulsion applications," *Opt. Eng.*, vol. 40, p. 598, 2001.

[61] M. A. Haque and M. T. A. Saif, "Microscale materials testing using mems actuators," *J. Microelectromech. S.*, vol. 10, no. 1, pp. 146–152, 2001.

[62] T. W. Yeow, K. L. E. Law, and A. Goldenberg, "Mems optical switches," *IEEE Commun. Mag.*, vol. 39, no. 11, pp. 158–163, 2001.

[63] K. L. Ekinci, "Electromechanical transducers at the nanoscale: actuation and sensing of motion in nanoelectromechanical systems," *Small*, vol. 1, no. 8-9, pp. 786–797, 2005.

[64] K. L. Ekinci and M. L. Roukes, "Nanoelectromechanical systems," *Rev. Sci. Instrum.*, vol. 76, no. 6, p. 061101, 2005.

[65] O. Y. Loh and H. D. Espinosa, "Nanoelectromechanical contact switches," *Nature Nanotechnol.*, vol. 7, no. 5, pp. 283–295, 2012.

[66] M. D. LaHaye, O. Buu, B. Camarota, and K. C. Schwab, "Approaching the quantum limit of a nanomechanical resonator," *Science*, vol. 304, no. 5667, pp. 74–77, 2004.

[67] T. Kouh, D. Karabacak, D. Kim, and K. Ekinci, "Diffraction effects in optical interferometric displacement detection in nanoelectromechanical systems," *Appl. Phys. Lett.*, vol. 86, no. 1, p. 013106, 2004.

[68] T. Rocheleau, T. Ndukum, C. Macklin, J. B. Hertzberg, A. A. Clerk, and K. C. Schwab, "Preparation and detection of a mechanical resonator near the ground state of motion," *Nature*, vol. 463, no. 7277, pp. 72–75, 2009.

[69] A. Boltasseva and V. M. Shalaev, "Fabrication of optical negative-index metamaterials: Recent advances and outlook," *Metamaterials*, vol. 2, no. 1, pp. 1–17, 2008.

[70] C. M. Soukoulis and M. Wegener, "Past achievements and future challenges in the development of three-dimensional photonic metamaterials," *Nature Photon.*, vol. 5, no. 9, pp. 523–530, 2011.

[71] N. C. Lindquist, P. Nagpal, K. M. McPeak, D. J. Norris, and S.-H. Oh, "Engineering metallic nanostructures for plasmonics and nanophotonics," *Rep. Prog. Phys.*, vol. 75, no. 3, p. 036501, 2012.

[72] P. B. Cui, Ed., *Recent advances in nanofabrication techniques and applications.* Intech, 2011.

[73] M. Deubel, G. Von Freymann, M. Wegener, S. Pereira, K. Busch, and C. M. Soukoulis, "Direct laser writing of three-dimensional photonic-crystal templates for telecommunications," *Nature Mater.*, vol. 3, no. 7, pp. 444–447, 2004.

[74] S. Kawata, H.-B. Sun, T. Tanaka, and K. Takada, "Finer features for functional microdevices," *Nature*, vol. 412, no. 6848, pp. 697–698, 2001.

[75] J. Fischer, G. von Freymann, and M. Wegener, "The materials challenge in diffraction-unlimited direct-laser-writing optical lithography," *Adv. Mater.*, vol. 22, no. 32, pp. 3578–3582, 2010.

[76] P. Rai-Choudury, Ed., *Handbook of microlithography, micromachining and microfabrication: handbook of microlithography.* SPIE, 1997, vol. PM39.

[77] R. F. Pease and S. Y. Chou, "Lithography and other patterning techniques for future electronics," *Proc. of the IEEE*, vol. 96, no. 2, pp. 248–270, 2008.

[78] http://www.elionix.co.jp/english/products/ELS/ELS7500EX.html.

[79] T. H. P. Chang, M. Mankos, K. Y. Lee, and L. P. Muray, "Multiple electron-beam lithography," *Microelectron. Eng.*, vol. 57, pp. 117–135, 2001.

[80] P. Petric, C. Bevis, A. Carroll, H. Percy, M. Zywno, K. Standiford, A. Brodie, N. Bareket, and L. Grella, "REBL: A novel approach to high speed maskless electron beam direct write lithography," *J. Vac. Sci.Tech. B*, vol. 27, no. 1, pp. 161–166, 2009.

[81] J. Orloff, *Handbook of charged particle optics.* CRC press, 2008.

[82] C. Enkrich, F. Pérez-Willard, D. Gerthsen, J. F. Zhou, T. Koschny, C. M. Soukoulis, M. Wegener, and S. Linden, "Focused-ion-beam nanofabrication of near-infrared magnetic metamaterials," *Adv. Mater.*, vol. 17, no. 21, pp. 2547–2549, 2005.

[83] C. A. Volkert and A. M. Minor, "Focused ion beam microscopy and micromachining," *MRS bulletin*, vol. 32, no. 5, pp. 389–399, 2007.

[84] P. Sigmund, "Theory of sputtering. I. Sputtering yield of amorphous and polycrystalline targets," *Phys. Rev.*, vol. 184, no. 2, p. 383, 1969.

[85] P. a. Sigmund, "A mechanism of surface micro-roughening by ion bombardment," *J. Mater. Sci.*, vol. 8, no. 11, pp. 1545–1553, 1973.

[86] S. Reyntjens and R. Puers, "A review of focused ion beam applications in microsystem technology," *J. Micromech. Microeng.*, vol. 11, no. 4, p. 287, 2001.

[87] M. Rösler and W. Brauer, "Theory of electron emission from solids by proton and electron bombardment," *Phys. Status Solidi B*, vol. 148, no. 1, pp. 213–226, 1988.

[88] D. Hasselkamp, "Kinetic electron emission from solid surfaces under ion bombardment," in *Particle Induced Electron Emission II*. Springer, 1992, pp. 1–95.

[89] A. Yasaka, "Feasibility study of spatial-phase-locked focused-ion-beam lithography," Ph.D. dissertation, Massachusetts Institute of Technology, 1995.

[90] I. Utke, P. Hoffmann, and J. Melngailis, "Gas-assisted focused electron beam and ion beam processing and fabrication," *J. Vac. Sci.Tech. B*, vol. 26, no. 4, pp. 1197–1276, 2008.

[91] B. Gholipour, C.-C. Huang, J. Y. Ou, and D. W. Hewak, "Germanium antimony lateral nanowire phase change memory by chemical vapor deposition," *Phys. Status Solidi B*, vol. 250, no. 5, pp. 994–998, 2013.

[92] T. E. Everhart and R. F. M. Thornley, "Wide-band detector for micro-microampere low-energy electron currents," *J. Sci. Instrum.*, vol. 37, no. 7, p. 246, 1960.

[93] C. N. Burrous, A. J. Lieber, and V. T. Zaviantseff, "Detection efficiency of a continuous channel electron multiplier for positive ions," *Rev. Sci. Instrum.*, vol. 38, no. 10, pp. 1477–1481, 1967.

[94] J. D. Schiffbauer and S. Xiao, "Novel application of focused ion beam electron microscopy (FIB-EM) in preparation and analysis of microfossil ultrastructures: A new view of complexity in early Eukaryotic organisms," *Palaios*, vol. 24, no. 9, pp. 616–626, 2009.

[95] http://www.fei.com/products/dualbeam/helios-nanolab/.

[96] K. Tanaka, E. Plum, J. Y. Ou, T. Uchino, and N. I. Zheludev, "Multifold enhancement of quantum dot luminescence in plasmonic metamaterials," *Phys. Rev. Lett.*, vol. 105, no. 22, p. 227403, 2010.

[97] R. F. Oulton, V. J. Sorger, D. Genov, D. Pile, and X. Zhang, "A hybrid plasmonic waveguide for subwavelength confinement and long-range propagation," *Nature Photonics*, vol. 2, no. 8, pp. 496–500, 2008.

[98] M. Noginov, V. Podolskiy, G. Zhu, M. Mayy, M. Bahoura, J. Adegoke, B. Ritzo, and K. Reynolds, "Compensation of loss in propagating surface plasmon polariton by gain in adjacent dielectric medium," *Opt. Express*, vol. 16, no. 2, pp. 1385–1392, 2008.

[99] E. Plum, V. A. Fedotov, P. Kuo, D. P. Tsai, and N. Zheludev, "Towards the lasing spaser: controlling metamaterial optical response with semiconductor quantum dots," *Opt. Express*, vol. 17, no. 10, pp. 8548–8550, 2009.

[100] S. Xiao, V. P. Drachev, A. V. Kildishev, X. Ni, U. K. Chettiar, H.-K. Yuan, and V. M. Shalaev, "Loss-free and active optical negative-index metamaterials," *Nature*, vol. 466, no. 7307, pp. 735–738, 2010.

[101] M. Wegener, J. L. GarcÝa-Pomar, C. M. Soukoulis, N. Meinzer, M. Ruther, and S. Linden, "Toy model for plasmonic metamaterial resonances coupled to two-level system gain," *Opt. Express*, vol. 16, no. 24, pp. 19 785–19 798, 2008.

[102] O. Wilhelmi, S. Reyntjens, C. Mitterbauer, L. Roussel, D. J. Stokes, and D. H. Hubert, "Rapid prototyping of nanostructured materials with a focused ion beam," *Jan. J. Appl. Phys.*, vol. 47, no. 6S, p. 5010, 2008.

[103] T. S. Kao, E. T. F. Rogers, J. Y. Ou, and N. I. Zheludev, "'Digitally' addressable focusing of light into a subwavelength hot spot," *Nano Lett.*, vol. 12, no. 6, pp. 2728–2731, 2012.

[104] V. A. Fedotov, T. Uchino, and J. Y. Ou, "Low-loss plasmonic metamaterial based on epitaxial gold monocrystal film," *Opt. Express*, vol. 20, no. 9, pp. 9545–9550, 2012.

[105] D. Bobb, G. Zhu, M. Mayy, A. Gavrilenko, P. Mead, V. Gavrilenko, and M. Noginov, "Engineering of low-loss metal for nanoplasmonic and metamaterials applications," *Appl. Phys. Lett.*, vol. 95, no. 15, p. 151102, 2009.

[106] A. Boltasseva and H. A. Atwater, "Low-loss plasmonic metamaterials," *Science*, 2011.

[107] M. G. Blaber, M. D. Arnold, and M. J. Ford, "Optical properties of intermetallic compounds from first principles calculations: a search for the ideal plasmonic material," *J. Phys.: Condens. Matter*, vol. 21, no. 14, p. 144211, 2009.

[108] M. Kuttge, E. Vesseur, J. Verhoeven, H. Lezec, H. Atwater, and A. Polman, "Loss mechanisms of surface plasmon polaritons on gold probed by cathodoluminescence imaging spectroscopy." *Appl. Phys. Lett.*, vol. 93, no. 11, p. 113110, 2008.

[109] D. Bobb, G. Zhu, M. Mayy, A. Gavrilenko, P. Mead, V. Gavrilenko, and M. Noginov, "Engineering of low-loss metal for nanoplasmonic and metamaterials applications," *Appl. Phys. Lett.*, vol. 95, no. 15, p. 151102, 2009.

[110] A. Green, E. Bauer, R. L. Peck, and J. Dancy, "Stages of epitaxial film formation," *Kristall und Technik*, vol. 5, no. 3, pp. 345–366, 1970.

[111] B. Lewis, "Physical processes in epitaxial growth," *Thin Solid Films*, vol. 7, no. 3, pp. 179–217, 1971.

[112] K. M. Kunz, A. K. Green, and E. Bauer, "On the formation of single crystal films of FCC metals on alkali halide cleavage planes in ultrahigh vacuum," *Phys. Status Solidi B*, vol. 18, no. 1, pp. 441–457, 1966.

[113] D. Stirland, "Electron-bombardment-induced changes in the growth and epitaxy of evaporated gold films," *Appl. Phys. Lett.*, vol. 8, no. 12, pp. 326–328, 1966.

[114] W. A. Jesser and J. W. Matthews, "Growth of copper, silver, and gold on twelve alkali halides cleaved in vacuum," *J. Cryst. Growth*, vol. 5, no. 2, pp. 83–89, 1969.

[115] V. A. Fedotov, M. Rose, S. Prosvirnin, N. Papasimakis, and N. I. Zheludev, "Sharp trapped-mode resonances in planar metamaterials with a broken structural symmetry," *Phys. Rev. Lett.*, vol. 99, no. 14, p. 147401, 2007.

[116] http://www.norcada.com/.

[117] N. Papasimakis, V. A. Fedotov, N. I. Zheludev, and S. L. Prosvirnin, "Metamaterial analog of electromagnetically induced transparency," *Phys. Rev. Lett.*, vol. 101, p. 253903, Dec 2008.

[118] S. Zhang, D. A. Genov, Y. Wang, M. Liu, and X. Zhang, "Plasmon-induced transparency in metamaterials," *Phys. Rev. Lett.*, vol. 101, no. 4, p. 47401, 2008.

[119] B. Gholipour, C.-C. Huang, J. Y. Ou, and D. W. Hewak, "Germanium antimony lateral nanowire phase change memory by chemical vapor deposition," *Phys. Status Solidi B*, vol. 250, no. 5, pp. 994–998, 2013.

[120] M. H. R. Lankhorst, B. W. S. M. M. Ketelaars, and R. A. M. Wolters, "Low-cost and nanoscale non-volatile memory concept for future silicon chips," *Nature Mater.*, vol. 4, no. 4, pp. 347–352, 2005.

[121] D. J. Bell, T. J. Lu, N. A. Fleck, and S. M. Spearing, "Mems actuators and sensors: observations on their performance and selection for purpose," *J. Micromech. Microeng.*, vol. 15, p. S153, 2005.

[122] M. Y. Al Aioubi, V. Djakov, S. E. Huq, and P. D. Prewett, "Deflection and load characterisation of bimorph actuators for bioMEMS and other applications," *Microelectron. Eng.*, vol. 73, pp. 898–903, 2004.

[123] D. Bullen, X. Wang, J. Zou, S.-W. Chung, C. A. Mirkin, and C. Liu, "Design, fabrication, and characterization of thermally actuated probe arrays for dip pen nanolithography," *J. Microelectromech. S.*, vol. 13, no. 4, pp. 594–602, 2004.

[124] E. Prodan, C. Radloff, N. J. Halas, and P. Nordlander, "A hybridization model for the plasmon response of complex nanostructures," *Science*, vol. 302, no. 5644, p. 419, 2003.

[125] S. Prasanna and S. M. Spearing, "Materials selection and design of microelectrothermal bimaterial actuators," *J. Microelectromech. S.*, vol. 16, no. 2, pp. 248 –259, 2007.

[126] J. Y. Ou, E. Plum, Z. J., and N. I. Zheludev, "An electromechanically reconfigurable plasmonic metamaterial operating in the near infrared," *Nature Nanotechnol.*, vol. 8, pp. 252–255, 2013.

[127] G. Chen and P. Hui, "Thermal conductivities of evaporated gold films on silicon and glass," *Appl. Phys. Lett.*, vol. 74, p. 2942, 1999.

[128] D. R. Queen and F. Hellman, "Thin film nanocalorimeter for heat capacity measurements of 30 nm films," *Rev. Sci. Instrum.*, vol. 80, p. 063901, 2009.

[129] H. L. Anderson, Ed., *AIP 50th anniversary physics vade mecum.* American Institute of Physics, 1981.

[130] J. D. Jackson, *Classical electrodynamics*, 1998, vol. 1.

[131] V. A. Fedotov, P. L. Mladyonov, S. L. Prosvirnin, and N. I. Zheludev, "Planar electromagnetic metamaterial with a fish scale structure," *Phys. Rev. E*, vol. 72, no. 5, p. 056613, 2005.

[132] A. S. Schwanecke, V. A. Fedotov, V. V. Khardikov, S. L. Prosvirnin, Y. Chen, and N. I. Zheludev, "Optical magnetic mirrors," *J. Opt. A: Pure Appl. Opt.*, vol. 9, no. 1, pp. L1–L2, 2007.

[133] T. S. Kao, F. M. Huang, Y. Chen, E. T. F. Rogers, and N. I. Zheludev, "Metamaterial as a controllable template for nanoscale field localization," *Appl. Phys. Lett.*, vol. 96, p. 041103, 2010.

[134] N. Tas, T. Sonnenberg, H. Jansen, R. Legtenberg, and M. Elwenspoek, "Stiction in surface micromachining," *J. Micromech. Microeng.*, vol. 6, no. 4, p. 385, 1996.

[135] X. Y. Meng, Z. Z. Wang, Y. Zhu, and C. T. Chen, "Mechanism of the electro-optic effect in the perovskite-type ferroelectric knbo3 and linbo3," *J. of Appl. Phys.*, vol. 101, no. 10, p. 103506, 2007.

[136] E. H. Turner, "High-frequency electro-optic coefficients of lithium niobate," *Appl. Phys. Lett.*, vol. 8, p. 303, 1966.

[137] B. Luk'yanchuk, N. I. Zheludev, S. A. Maier, N. J. Halas, P. Nordlander, H. Giessen, and C. T. Chong, "The Fano resonance in plasmonic nanostructures and metamaterials," *Nature Mater.*, vol. 9, p. 707, 2010.

[138] D. G. Grier, "A revolution in optical manipulation," *Nature*, vol. 424, pp. 810–816, 2003.

[139] K. Dholakia and T. Čižmár, "Shaping the future of manipulation," *Nature Photon.*, vol. 5, pp. 335–342, 2011.

[140] M. L. Juan, M. Righini, and R. Quidant, "Plasmon nano-optical tweezers," *Nature Photon.*, vol. 5, pp. 349–356, 2011.

[141] J. Chen, J. Ng, Z. Lin, and C. T. Chan, "Optical pulling force," *Nature Photon.*, vol. 5, pp. 531–534, 2011.

[142] K. Dholakia and P. Zemánek, "Colloquium: gripped by light: optical binding," *Rev. Mod. Phys.*, vol. 82, pp. 1767–1791, 2010.

[143] T. J. Kippenberg and K. J. Vahala, "Cavity optomechanics: back-action at the mesoscale," *Science*, vol. 321, pp. 1172–1176, 2008.

[144] I. Favero and K. Karrai, "Optomechanics of deformable optical cavities," *Nature Photon.*, vol. 3, pp. 201–205, 2009.

[145] M. Eichenfield, J. Chan, R. M. Camacho, K. J. Vahala, and O. Painter, "Optomechanical crystals," *Nature*, vol. 462, pp. 78–82, 2009.

[146] G. Anetsberger, O. Arcizet, Q. P. Unterreithmeier, R. Rivière, A. Schliesser, E. M. Weig, J. P. Kotthaus, and T. J. Kippenberg, "Near-field cavity optomechanics with nanomechanical oscillators," *Nature Phys.*, vol. 5, pp. 909–914, 2009.

[147] K. Usami, A. Naesby, T. Bagci, B. M. Nielsen, J. Liu, S. Stobbe, P. Lodahl, and E. S. Polzik, "Optical cavity cooling of mechanical modes of a semiconductor nanomembrane," *Nature Phys.*, vol. 8, pp. 168–172, 2012.

[148] L. Ding, C. Baker, P. Senellart, A. Lemaitre, S. Ducci, G. Leo, and I. Favero, "High frequency GaAs nano-optomechanical disk resonator," *Phys. Rev. Lett.*, vol. 105, p. 263903, 2010.

[149] Y.-G. Roh, T. Tanabe, A. Shinya, H. Taniyama, E. Kuramochi, S. Matsuo, T. Sato, and M. Notomi, "Strong optomechanical interaction in a bilayer photonic crystal," *Phys. Rev. B*, vol. 81, p. 121101(R), 2010.

[150] M. Eichenfield, C. P. Michael, R. Perahia, and O. Painter, "Actuation of micro-optomechanical systems via cavity-enhanced optical dipole forces," *Nature Photon.*, vol. 1, pp. 416–422, 2007.

[151] P. T. Rakich, M. A. Popovi, M. Soljai, and E. P. Ippen, "Trapping, corralling and spectral bonding of optical resonances through optically induced potentials," *Nature Photon.*, vol. 1, pp. 658–665, 2007.

[152] M. Li, W. H. P. Pernice, C. Xiong, T. Baehr-Jones, M. Hochberg, and H. X. Tang, "Harnessing optical forces in integrated photonic circuits," *Nature*, vol. 456, pp. 480–484, 2008.

[153] G. S. Wiederhecker, L. Chen, A. Gondarenko, and M. Lipson, "Controlling photonic structures using optical forces," *Nature*, vol. 462, pp. 633–636, 2009.

[154] D. V. Thourhout and J. Roels, "Optomechanical device actuation through the optical gradient force," *Nature Photon.*, vol. 4, pp. 211–217, 2010.

[155] M. Bagheri, M. Poot, M. Li, W. P. H. Pernice, and H. X. Tang, "Dynamic manipulation of nanomechanical resonators in the high-amplitude regime and non-volatile mechanical memory operation," *Nature Nanotechnol.*, vol. 6, pp. 726–732, 2011.

[156] P. B. Deotare, I. Bulu, I. W. Frank, Q. Quan, Y. Zhang, R. Ilic, and M. Loncar, "All optical reconfiguration of optomechanical filters," *Nature Commun.*, vol. 3, p. 846, 2012.

[157] A. H. Safavi-Naeini, T. P. M. Alegre, J. Chan, M. Eichenfield, M. Winger, Q. Lin, J. T. Hill, D. E. Chang, and O. Painter, "Electromagnetically induced transparency and slow light with optomechanics," *Nature*, vol. 472, pp. 69–73, 2011.

[158] C. Tang, Q. Wang, F. Liu, Z. Chen, and Z. Wang, "Optical forces in twisted split-ring-resonator dimer stereometamaterials," *Opt. Express*, vol. 21, pp. 11 783–11 793, 2013.

[159] R. Zhao, P. Tassin, T. Koschny, and C. M. Soukoulis, "Optical forces in nanowire pairs and metamaterials," *Opt. Express*, vol. 18, pp. 25 665–25 676, 2010.

[160] J. Zhang, K. F. MacDonald, and N. I. Zheludev, "Nonlinear dielectric optomechanical metamaterials," *Light Sci. Appl.*, p. in press, 2013.

[161] J. Zhang, K. F. MacDonald, and N. I. Zheludev, "Optical gecko toe: optically controlled attractive near-field forces between plasmonic metamaterials and dielectric or metal surfaces," *Phys. Rev. B*, vol. 85, p. 205123, 2012.

[162] N. I. Zheludev, "The road ahead for metamaterials," *Science*, vol. 328, pp. 582–583, 2010.

[163] T. S. Kao, S. D. Jenkins, J. Ruostekoski, and N. I. Zheludev, "Coherent control of nanoscale light localization in metamaterial: Creating and positioning isolated subwavelength energy hot spots," *Phys. Rev. Lett*, vol. 106, no. 8, p. 085501, 2011.

[164] D. Van Thourhout and J. Roels, "Optomechanical device actuation through the optical gradient force," *Nature Photon.*, vol. 4, no. 4, pp. 211–217, 2010.

[165] S. K. Lamoreaux, "The Casimir force: background, experiments, and applications," *Rep. Prog. Phys.*, vol. 68, no. 1, p. 201, 2005.

[166] N. Papasimakis and N. I. Zheludev, "Metamaterial-induced transparency," *Optics & Photonics News*, vol. 20, no. 10, p. 22, 2009.

[167] J. B. J. Fourier and A. Freeman, *The analytical theory of heat.* The University Press, 1878.

[168] http://en.wikipedia.org/wiki/Euler-Bernoulli_beam_theory.

[169] R. Thijssen, E. Verhagen, T. J. Kippenberg, and A. Polman, "Plasmon nanomechanical coupling for nanoscale transduction," *Nano Lett.*, vol. 13, pp. 3293–3297, 2013.

[170] A. Said, M. Sheik-Bahae, D. J. Hagan, T. Wei, J. Wang, J. Young, and E. W. Van Stryland, "Determination of bound-electronic and free-carrier nonlinearities in ZnSe, GaAs, CdTe, and ZnTe," *J. Opt. Soc. Am. B*, vol. 9, no. 3, pp. 405–414, 1992.